This is to certify that the
dissertation entitled

Rapid Numerical Evaluation of Ultrasound Pressure Integrals
and Potential Integrals

presented by

Duo Chen

has been accepted towards fulfillment
of the requirements for the

Ph.D. degree in Electrical Engineering

Robert J. McGough
Major Professor's Signature

Dec. 18, 2009
Date

RAPID NUMERICAL EVALUATION OF ULTRASOUND PRESSURE INTEGRALS AND POTENTIAL INTEGRALS

By

Duo Chen

A DISSERTATION

Submitted to
Michigan State University
in partial fulfillment of the requirements
for the degree of

DOCTOR OF PHILOSOPHY

Electrical Engineering

2009

ABSTRACT

RAPID NUMERICAL EVALUATION OF ULTRASOUND PRESSURE INTEGRALS AND POTENTIAL INTEGRALS

By

Duo Chen

Analytical expressions are derived for fast calculations of time-harmonic and transient near field pressures generated by triangular pistons. These fast expressions remove singularities from the impulse response, thereby reducing the computation time and the peak numerical error with a general formula that describes the nearfield pressure produced by any triangular piston geometry. The time-domain expressions are further accelerated by a time-space decomposition approach that analytically separates the spatial and temporal components of the numerically computed transient pressure. Analytical 2D integral expressions are derived for fast calculations of time-harmonic and transient nearfield pressures generated by apodized rectangular pistons. The 2D expressions eliminate the numerical singularities that are otherwise present in numerical models of pressure fields generated by apodized rectangular pistons. A simplified time space decomposition method is also described, and this method further reduces the computation time for transient pressure fields. The results, compared with the Rayleigh-Sommerfeld integral, the Field II program and the impulse response method, indicate that the FNM achieves smallest errors for the same computation time among those methods. A 1D FNM for calculating the pressure generated by a polynomial apodized rectangular piston is also obtained. The fast method is based on the instantaneous impulse response. A trigonometric transform of the integrand is performed and the order of integration is exchanged to obtain the 1D integral for the apodized FNM for both apodization functions. The time and error comparisons are performed among the 1D polynomial apodized FNM, the 2D apodized FNM and the

Rayleigh-Sommerfeld integral. The results show that the 1D polynomial apodized FNM has the fastest convergence. Analytical expressions are derived for fast calculations of potential integrals. These potential integrals inculde uniformly excited volume potential integrals, polynomial apodized surface integrals and polynomial apodized volume potential integrals. The derivation starts with the fast near-field method (FNM), which originates from ultrasound pressure calculations generated by polygonal pistons. For potential integrals evaluated over a volume source, the volume source is first subdivided into subdomains about the observation points. The total potential is the summation of the potential over each submain which can be reduced to 1D integrals. Those calculation methods remove the singularities from the Rayleigh-Sommerfeld integral by subtracting sigularities in the integrand and thus can achieve rapid convergence. Simulations results are compared with the Rayleigh-Sommerfeld integral and the singularity cancellation method evaluated on a 3D grid. The results indicate that the 1D FNM expressions reduces the computation time or the number of sample point needed significantly than the Rayleigh-Sommerfeld integral and the singularity cancellation method for a given number signifcant digits.

Dedicated to my wife, Jie Sun, and my son, Eric Yaoting Chen.

ACKNOWLEDGMENTS

Firstly, I would like to thank my Ph.D. advisor Dr. Robert J. McGough for his great support during the past five and a half years. I have learned a lot from his guidance, his encouragement and his insightful discussions. Secondly, I would like to thank my Ph.D. Committee members for providing helpful guidance and discussions: Dr. Shanker Balasubramaniam, Dr. Edward Rothwell, Dr. Mei Zhuang, and Dr. Neil Wright. Thirdly, I would like to thank my colleagues at the Biomedical Ultrasonics and Eletromagnetics Lab (BUEL) at MSU for their friendship and help during my stay at MSU: Ruihua Ding, Liyong Wu, Xiaozheng Zeng, Khawar Khurshid, Don Chorman, Jason Biel, James F. Kelly, Josh Wong, Don VanderLaan, Matthew Richard Jennings, and Christopher Johnson. Finally, I would like to express my deepest gratitude and love to my dear wife, Jie Sun for her unconditional love and support to me. Without her I would have never completed this achievement.

TABLE OF CONTENTS

LIST OF TABLES

LIST OF FIGURES

CHAPTER 1

Introduction

1.1 Ultrasound pressure calculations

As increasingly complex transducer geometries are adopted for emerging applications of ultrasound imaging and therapy, new methods are needed for rapid calculations of pressure fields produced by these transducers. Fast numerical simulations are especially important for simulations of phased array structures containing hundreds or thousands of tranducers that generate pressure in large computational domains. Simulation methods that either directly evaluate the impulse response [1, 2, 3, 4] or subdivide each transducer into smaller elements and then superpose the pressure [5, 6] provide a convenient model for these calculations, but in the nearfield region, the convergence of these methods is relatively slow [7]. Furthermore, numerical implementations of the impulse response for flat unfocused transducers encounter some difficulties throughout the paraxial region [7, 8, 9].

Pressure fields from uniform planar sources can be calculated using several numerical methods including the impulse response method [1, 2, 3], the Field II program [10, 11], the Rayleigh-Sommerfeld integral [6], and the fast nearfield method (FNM) [7, 8]. Among these methods, the FNM achieves the smallest error in the least time

[7, 8, 12]. The FNM for uniformly excited rectangular pistons [8] and circular pistons [7] eliminates the $1/R$ singularity and therefore avoids problems with large errors in the nearfield region. The FNM also converges rapidly in the nearfield, which has been demonstrated for both time-harmonic and transient excitations [7, 8, 36]. For uniform excitations, the FNM is ideal for nearfield pressure calculations and for reference calculations that evaluate the numerical errors associated with other methods [13, 14].

Modeling the nearfield pressure generated by a spatially varying particle velocity on the face of a rectangular piston is of practical importance for many acoustics applications [15, 16], where accurate and fast computer simulations are required. Fast ultrasound simulations are especially important for calculating pressure fields in large computational domains, specifically steady-state HIFU simulations for ultrasound therapy [17, 18] and transient calculations for ultrasound imaging [19, 20]. Individual array elements are typically modeled as single baffled rectangular sources with uniform surface particle velocities, but the particle velocity on the transducer face is in general nonuniform. For example, Lin et. al. [21] shows that the surface particle velocity of a fluid-loaded piezoelectric element on a phased array is nonuniform, and Borges et. al [22] demonstrates that the surface velocity of a single array element is apodized and delayed when matching layers are used.

1.2 Potential integrals

Numerical calculation of potential integrals involved in integral equations are of great importance in scattering problems. The polynomial function is a very popular function to approximate the electric and magnetic currents. For example, three-dimensional polynomials are adopted to approximate the entire-domain normalized current density by Moraros and Popovic [23] as applied to the optimization of volume

potential integrals involved in the moment-method analysis of 3D dielectric scatters. The commonly used Rao-Wilton-Glisson basis that is also a linear basis function which is used to approximate both the magnetic and electric currents [24]. Potential integrals are often singular and direct evaluation of potential integrals may encounter numerical difficulties. To improve the accuracy of the potential integrals, singularity subtraction methods [23, 25, 26, 27, 28] or singularity cancellation methods [30, 31, 32, 33] are often used to acheive better performance. Typically, those methods manipulate the integrands to eliminate singularties and thus the number of dimensions over which the integration is performed remains the same for both methods. This approach is reasonable for general potential integrals; however, more efficient expressions can be acheived when polynomial apodized potential integrals are considered.

Potentials generated by uniformly excited plannar source and uniformly excited plannar source are computed with both the Rayleigh-Sommerfeld integral [6] and the fast nearfield method (FNM) [7, 8, 12]. The existing FNM achieves much better accuracy by eliminating the $1/R$ singularity in the Rayleigh-Sommerfeld integral and by simplifying the multiple integral into a single integral. Since the numerical evaluation of potential integrals with polynomial apodization are routinely evaluated, a similar fast nearfield method is needed for those integrals to improve the performance.

1.3 Thesis Content

This dissertation investigates fast pressure calculation methods for planar pistons and fast potential evaluation methods for potential integrals. Chapter 2 introduces fast calculations for the time-harmonic and transient pressures generated by trangular pistons. The transient calculations are further accelerated by the time-space decomposition method. Analytically 2D integral expressions for fast calculations of

time-harmonic and transient nearfield pressures generated by apodized rectangular pistons are derived in Chapter 3. As a special case of Chapter 3, fast caculations of pressure generated by a polynomial apodized rectangular pistion are obtained based on the instantaneous impulse response in Chapter 4. Chaper 5 introduces 1D fast expressions for calculations of uniformly excited volume potential integrals that are otherwise represented by a triple integral. Fast 1D calculation expressions for pressures generated by surface integrals and volume integrals with polynomial apodization are introduced in Chapters 6 and 7. Chapter 8 concludes the thesis.

CHAPTER 2

A Fast Nearfield Method for Calculations of Time-harmonic and Transient Pressures Produced by Triangular Pistons

The substantial reduction in computation time demonstrated by the FNM for calculations of nearfield pressures generated by circular and rectangular pistons motivates the derivation of similar integral expressions for triangular sources. After the impulse response is obtained for right, acute, and obtuse triangular sources, general FNM expressions for time-harmonic and transient inputs are then demonstrated for a triangular source, and the time-space decomposition of the FNM integral is presented for a transient excitation. Based on these expressions for the nearfield pressure generated by a triangular source, computation times are evaluated for the same peak numerical errors. For time-harmonic inputs applied to a triangular source, results show that FNM calculations are several times faster than both exact and approximate impulse response calculations, and for pulsed excitations, results demonstrate that FNM cal-

culations performed with time-space decomposition are also much faster than exact and approximate impulse response calculations for triangular piston geometries.

2.1 Time-harmonic and Transient Nearfield Pressure Calculations for Triangular Sources

2.1.1 Impulse response calculations for a triangular source

The geometry for a right triangular source with a *right angle* $\angle BCA$ at vertex C is depicted in Figure 2.1a. For this right triangle and the triangles in Figures 2.1b and 2.1c, the impulse response is evaluated at a point directly over the vertex A (indicated in bold in Figure 2.1), where the the orthogonal projection of the observation point onto the source plane is exactly coincident with the vertex A, and the distance from the observation point to the source plane along this orthogonal projection is represented by the variable z. In Figure 2.1a, the acute angle $\angle CAB = \tan^{-1}(s/l)$ defines the angular extent of sector EAB with radius $\sqrt{l^2+s^2}$, which has an impulse response of $c/(2\pi)\tan^{-1}(s/l)$ for $(z/c) \le t \le \sqrt{z^2+l^2+s^2}/c$. The impulse response for the right triangle $\triangle ABC$ contained within the sector EAB is obtained by subtracting the impulse response of the region ECB between the curved outer edge of the sector and the near edge of the right triangle so that only the contribution from the right triangle $\triangle ABC$ remains. The impulse response of the region ECB is $c/(2\pi)\cos^{-1}\left(l/\sqrt{c^2t^2-z^2}\right)$ for $\sqrt{z^2+l^2}/c \le t \le \sqrt{z^2+l^2+s^2}/c$, and therefore the impulse response at an orthogonal distance z above the vertex A is

$$h_{right}(z;t) = \begin{cases} c/(2\pi)\tan^{-1}(s/l) & \text{for } t_1 \le t \le t_2 \\ c/(2\pi)\left\{\tan^{-1}(s/l) - \cos^{-1}\dfrac{l}{\sqrt{c^2t^2-z^2}}\right\} & \text{for } t_2 \le t \le t_3 \\ 0 & \text{otherwise} \end{cases}, \tag{2.1}$$

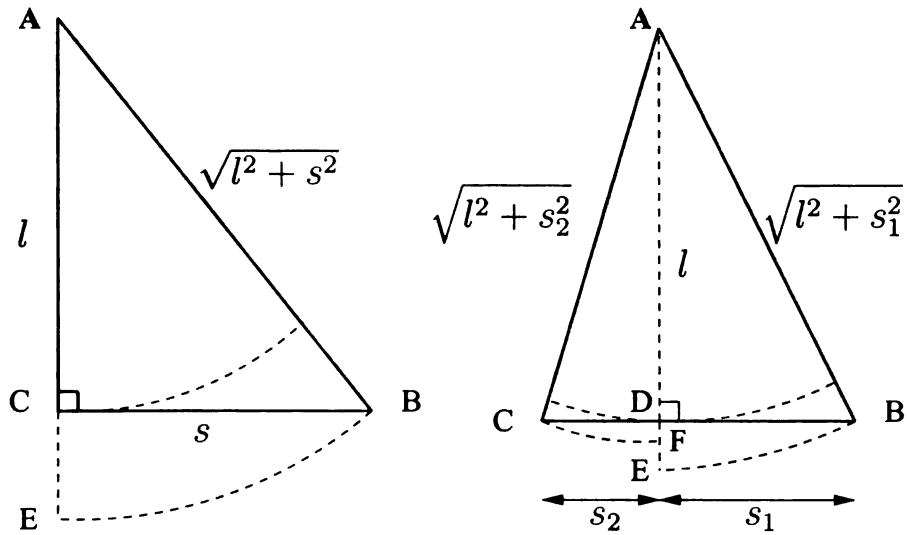

(a) Triangular source with right $\angle BCA$. (b) Triangular source with acute $\angle BCA$

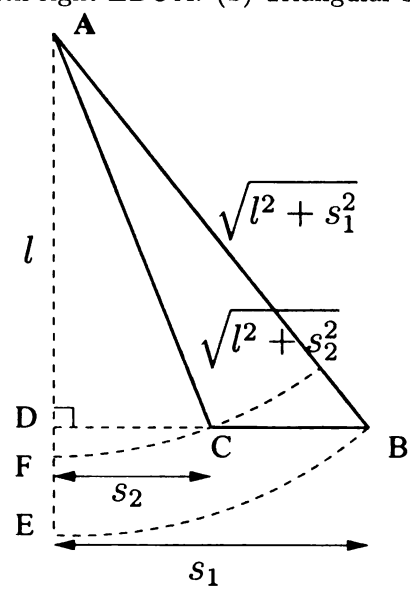

(c) Triangular source with obtuse $\angle BCA$

Figure 2.1. Triangular source geometries defined for nearfield pressure calculations. The nearfield pressure is evaluated above the vertex A (indicated in bold), and the shape of the triangle (right, acute, or obtuse) is defined by the angle $\angle BCA$. The height of each triangle is indicated by l, and the bases of the individual right triangles are indicated by s, s_1, and s_2. The acute triangle in b) is represented by the sum of two right triangles, and the obtuse triangle in c) is defined as the difference between two right triangles.

where the values of t_1, t_2, and t_3 are z/c, $\sqrt{z^2+l^2}/c$, and $\sqrt{z^2+l^2+s^2}/c$, respectively.

For other triangular sources, the impulse response is readily constructed from the sum or difference between two right triangles. Figure 2.1b contains an example of a triangular source with an *acute angle* $\angle BCA$ at vertex C. The expression for the impulse response evaluated at a point directly over the vertex A is obtained by evaluating the *sum* of the contributions from the right triangles $\angle CDA$ and $\angle BDA$, each with a right angle at vertex D. The resulting impulse response above the vertex A in Figure 2.1b is represented by

$$h_{sum}(z;t) =$$

$$\begin{cases} c/(2\pi)\left\{\tan^{-1}(s_1/l)+\tan^{-1}(s_2/l)\right\} & \text{for } t_1 \le t \le t_2 \\ \frac{c}{2\pi}\left\{\tan^{-1}(s_1/l)+\tan^{-1}(s_2/l)-2\cos^{-1}\left(l/\sqrt{c^2t^2-z^2}\right)\right\} & \text{for } t_2 \le t \le t_3 \\ c/(2\pi)\left\{\tan^{-1}(s_1/l)-\cos^{-1}\left(l/\sqrt{c^2t^2-z^2}\right)\right\} & \text{for } t_3 \le t \le t_4 \\ 0 & \text{otherwise} \end{cases}, \tag{2.2}$$

where the values of s_1 and s_2 are selected such that $s_1 \ge s_2$ and the values of t_1, t_2, t_3 and t_4 are z/c, $\sqrt{z^2+l^2}/c$, $\sqrt{z^2+l^2+s_2^2}/c$, and $\sqrt{z^2+l^2+s_1^2}/c$, respectively.

Similarly, Figure 2.1c contains an example of a triangular source with an *obtuse angle* $\angle BCA$ at vertex C, where the impulse response is again evaluated at a point directly over the vertex A, but the impulse response is instead evaluated for the *difference* between two right triangles. The impulse response for the triangle in Figure

2.1c is

$$h_{diff}(z;t) = \begin{cases} c/(2\pi)\left\{\tan^{-1}(s_1/l) - \tan^{-1}(s_2/l)\right\} & \text{for } t_1 \le t \le t_2 \\ c/(2\pi)\left\{\tan^{-1}(s_1/l) - \cos^{-1}\left(l/\sqrt{c^2t^2 - z^2}\right)\right\} & \text{for } t_2 \le t \le t_3 \\ 0 & \text{otherwise} \end{cases}, \tag{2.3}$$

where the values of s_1 and s_2 are selected such that $s_1 > s_2$ and the values of t_1, t_2, and t_3 are z/c, $\sqrt{z^2 + l^2 + s_2^2}/c$, and $\sqrt{z^2 + l^2 + s_1^2}/c$, respectively.

Time-harmonic impulse response calculations

The time-harmonic pressure generated by these triangular source geometries is proportional to the Fourier transform of the impulse response. Therefore, the formula for the time-harmonic pressure generated by the right triangle in Figure 2.1a is

$$P_{right}(z;k) = \frac{\omega\rho_0 v e^{j\omega t}}{2\pi}\left\{\frac{j}{k}\tan^{-1}\frac{s}{l}e^{-jkz} - \frac{j}{k}\tan^{-1}\frac{s}{l}e^{-jk\sqrt{z^2+l^2+s^2}} + \int_{\sqrt{z^2+l^2}}^{\sqrt{z^2+l^2+s^2}} e^{-jk\beta}\cos^{-1}\frac{l}{\sqrt{\beta^2 - z^2}}d\beta\right\}. \tag{2.4}$$

The time-harmonic pressures produced the remaining triangles depicted in Figures 2.1b and 2.1c are obtained by adding and subtracting the contributions of two right triangles, as for calculations of the impulse response in Eqs. 2.2 and 2.3, respectively.

Transient impulse response calculations

Transient nearfield pressures are computed with the impulse response through the convolution

$$p(z;t) = \rho_0 \dot{v}(t) \otimes h(z;t), \tag{2.5}$$

where the time derivative of the particle velocity $\dot{v}(t)$ is evaluated analytically from the excitation pulse $v(t)$, and the convolution $\otimes$ is evaluated with the fast Fourier

transform (FFT). In particular, the discrete Fourier transforms of $\dot{v}(t)$ and $h(z,t)$ are computed with the FFT, the results are multiplied, and the inverse FFT is applied to the product. The forward and inverse FFT routines are computed with the Fastest Fourier Transform in the West (FFTW) library [34].

Field II

Field II is a software package [10] that computes the impulse response either by superposing far field contributions from small rectangles or by evaluating expressions similar to Eqs. 2.1, 2.2, and 2.3. With both approaches, Field II modifies the impulse response according to the area under the impulse response curve [11]. This modification allows Field II to reduce the temporal sampling for impulse response calculations, which are directly applicable to transient and steady-state nearfield pressure computations.

Smoothed impulse response

The Fourier transform of Eq. 2.5 is

$$P(z;\omega) = i\omega\rho_0 V(\omega) H(z,\omega). \tag{2.6}$$

Normally, the excitation $V(\omega)$ is bandlimited, so the high-frequency components in the Fourier transform $H(z;\omega)$ of the impulse response are negligible. To exploit the bandlimited characteristics of the excitation $v(t)$, the formula for a smoothed impulse response is given by [35]

$$h_{smooth}(z;t) = \frac{O(c(t+\Delta t/2)) - O(c(t-\Delta t/2))}{2\pi t c \Delta t}, \tag{2.7}$$

where $O(ct)$ is the area that formed by the intersection of the transducer and the sphere with radius ct centered at the observation point, and Δt is the length of the

rectangular pulse that smooths the analytical impulse response. The constraint

$$f_{Emax} < \frac{1}{\Delta t} \tag{2.8}$$

insures proper smoothing, where f_{Emax} is the highest-frequency component of the excitation pulse, and $\Delta t = 0.02\mu s$ in the simulations that follow. The result obtained from Eq. 2.7 is then directly applied to calculations of the nearfield pressure for time-harmonic and transient inputs.

2.1.2 The fast nearfield method for a triangular source

Integral expressions that describe the fast nearfield method (FNM) for a triangular source excited by a time-harmonic input are obtained by replacing the inverse cosine term with the integral form of the inverse tangent and then exchanging the order of integration in the impulse response expressions for right, acute, and obtuse triangles. The procedure is illustrated by:

$$\begin{aligned}
&\int_{\sqrt{z^2+l^2}}^{\sqrt{z^2+l^2+s^2}} e^{-jk\beta} \cos^{-1} \frac{l}{\sqrt{\beta^2 - z^2}} d\beta \\
&= \int_{\sqrt{z^2+l^2}}^{\sqrt{z^2+l^2+s^2}} e^{-jk\beta} \tan^{-1} \frac{\sqrt{\beta^2 - z^2 - l^2}}{l} d\beta \\
&= \int_{\sqrt{z^2+l^2}}^{\sqrt{z^2+l^2+s^2}} \int_0^{\sqrt{\beta^2-z^2-l^2}} e^{-jk\beta} \frac{l}{\sigma^2 + l^2} d\sigma d\beta \\
&= \int_0^s \left[\int_{\sqrt{\sigma^2+z^2+l^2}}^{\sqrt{z^2+l^2+s^2}} e^{-jk\beta} d\beta \right] \frac{l}{\sigma^2 + l^2} d\sigma d\beta.
\end{aligned} \tag{2.9}$$

After defining a new variable of integration and subtracting the singularity at $z = 0$ from each integrand, the resulting FNM expression for a *right* triangle (Figure 2.1a), the *sum* of two right triangles (Figure 2.1b) that share a common side of length l, and

the *difference* between two right triangles (Figure 2.1c) that share a common side of length l is

$$P(z;k) = \frac{-\rho c v e^{j\omega t}}{2\pi} \int_{x_C}^{x_B} \frac{l}{\sigma^2 + l^2} \left(e^{-jk\sqrt{\sigma^2+z^2+l^2}} - e^{-jkz} \right) d\sigma, \qquad (2.10)$$

where l represents the height of the triangle, and x_B and x_C represent the x-coordinates of B and C, respectively. In Figures 2.1a, 2.1b, and 2.1c, the values of (x_B, x_C) are $(s, 0)$, $(s_1, -s_2)$, and (s_1, s_2), respectively. Thus, a single FNM expression represents all three triangle geometries in Figure 2.1, whereas the impulse response requires a separate expression for each triangle in Figure 2.1.

Transient FNM calculations

The inverse Fourier transform of Eq. 2.10 generates the FNM expression for the transient response. The transient pressure generated by a triangular source above the vertex A is represented by

$$p(z;t) = -\frac{\rho c}{2\pi} \int_{x_C}^{x_B} \frac{l}{l^2 + \sigma^2} \left[v\left(t - \frac{1}{c}\sqrt{z^2 + \sigma^2 + l^2} \right) - v(t - z/c) \right] d\sigma, \qquad (2.11)$$

where the transient excitation is represented by $v(t)$. By retaining the $v(t - z/c)$ term within the integral and subtracting the singularity, Eq. 2.11 maintains the rapid rate of convergence achieved for time-harmonic calculations with Eq. 2.10.

Time-Space Decomposition

Transient FNM computations are accelerated by decoupling the temporal and spatial dependence of Eq. 2.11. The time-space decomposition approach, demonstrated previously for a circular source [36], expands the delayed input pulse $v(t - \tau)$ in terms of temporal weighting functions $g_n(t)$ and spatially-dependent terms $f_n(\tau)$ that depend

Table 2.1. Basis functions for time-space decomposition with a Hanning-weighted pulse.

temporal basis functions $g_n(t)$	spatial basis functions $f_n(\tau)$
$g_1(t) = \frac{1}{2}\sin(2\pi f_0 t)$	$f_1(\tau) = \cos(2\pi f_0 \tau)$
$g_2(t) = -\frac{1}{2}\cos(2\pi f_0 t)$	$f_2(\tau) = \sin(2\pi f_0 \tau)$
$g_3(t) = -\frac{1}{2}\cos\left(\frac{2\pi t}{W}\right)\sin(2\pi f_0 t)$	$f_3(\tau) = \cos\left(\frac{2\pi \tau}{W}\right)\cos(2\pi f_0 \tau)$
$g_4(t) = \frac{1}{2}\cos\left(\frac{2\pi t}{W}\right)\cos(2\pi f_0 t)$	$f_4(\tau) = \cos\left(\frac{2\pi \tau}{W}\right)\sin(2\pi f_0 \tau)$
$g_5(t) = \frac{1}{2}\sin\left(\frac{2\pi t}{W}\right)\sin(2\pi f_0 t)$	$f_5(\tau) = \sin\left(\frac{2\pi \tau}{W}\right)\cos(2\pi f_0 \tau)$
$g_6(t) = \frac{1}{2}\sin\left(\frac{2\pi t}{W}\right)\cos(2\pi f_0 t)$	$f_6(\tau) = \sin\left(\frac{2\pi \tau}{W}\right)\sin(2\pi f_0 \tau)$

only on the coordinates of the observation point and the variable of integration σ through $\tau = \frac{1}{c}\sqrt{z^2 + \sigma^2 + l^2}$. The decoupled input pulse is thus represented by

$$v(t-\tau) = rect\left(\frac{t-\tau}{W}\right)\sum_{n=1}^{N} f_n(\tau) g_n(t), \tag{2.12}$$

where the time duration of the pulse is indicated by the parameter W. The decomposed pulse in Eq. 2.12 is then inserted into Eq. 2.11, and then time-dependent terms are factored out of the integral. The result consists of N edge wave terms specified by

$$E_n = -\frac{\rho c}{2\pi} l \int_{x_C}^{x_B} \frac{f_n(\tau)}{\sigma^2 + l^2} rect\left(\frac{t-\tau}{W}\right) d\sigma \tag{2.13}$$

and a direct wave term given by

$$D = -\frac{\rho c}{2\pi} v(t - z/c) l \int_{x_C}^{x_B} \frac{1}{\sigma^2 + l^2} d\sigma. \tag{2.14}$$

The temporal dependence of the edge wave integrand in Eq. 2.13 is eliminated when the effect of the *rect* function is instead shifted to the limits of integration. This operation, which restricts the edge wave contributions by only considering those that have reached the observation point without completely passing the observation point, completely removes all temporal variables from the integrand. As a result, calculations of transient pressure fields are converted into the numerical evaluation and subsequent superposition of N spatial integrals that are weighted by analytical time-dependent

terms. Further reduction in the computation time is achieved by storing redundant edge wave calculations from Eq. 2.13 in the matrix

$$K_n(i,j) = \sum_{m=i}^{j} w_m \frac{f_n(\tau[\sigma_m])}{\sigma_m^2 + l^2}. \tag{2.15}$$

In Eq. 2.15, w_m represents the weights and σ_m represents the abscissas computed for Gauss quadrature, the value of $\tau[\sigma_m]$ is obtained from the relation $\tau[\sigma_m] = \frac{1}{c}\sqrt{z^2 + \sigma_m^2 + l^2}$, and the indices i and j indicate the shortest and longest times that correspond to the limits of integration. The values in $K_n(i,j)$ are initialized within the computation procedure only for the points that are needed, and then the time-space decomposition calculations superpose the numerically computed results of the spatial integrals with analytical time-dependent weighting factors to achieve a significant reduction in computation time for transient pressure calculations in the nearfield region.

2.1.3 Superposition calculations with impulse response and FNM expressions

At observation points away from the normal that passes through a vertex of the triangular source, impulse response and FNM calculations project the observation point onto the source plane and then superpose the contributions from two or three triangles as in Figure 2.2. The contributions from three triangles are either added, as shown in Figure 2.2a for an observation point within the lateral extent of the source triangle $\triangle ABC$, or added and subtracted as demonstrated in Figure 2.2b for an observation point outside of the lateral extent of the source triangle. Whether a contribution is added or subtracted depends on the location of the projected observation point in the source plane relative to each side of the triangular source.

The FNM admits some additional simplifications for nearfield calculations of pressures generated by the triangle $\triangle ABC$ in Figure 2.2. If the three lines that are co-

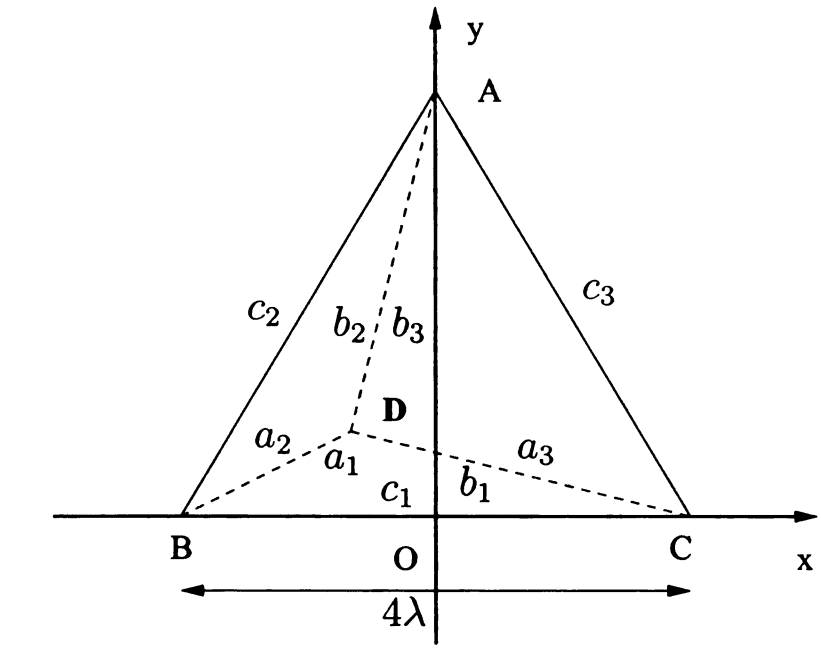

(a)

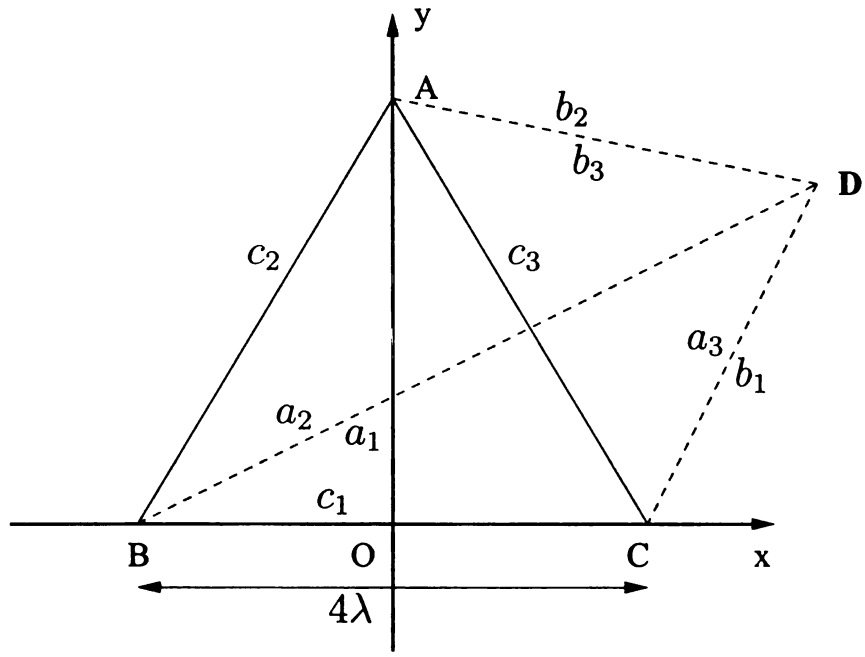

(b)

Figure 2.2. Superposition operations that calculate nearfield pressures generated by an equilateral triangular source, where each side is four wavelengths long. The vertex D (indicated in bold) is the projection of the observation point onto the source plane, which partitions the radiating source into three triangles with sides (a_i, b_i, c_i). (a) The field point is located inside of the equilateral triangular source. (b) The field point is located outside of the equilateral triangular source.

incident with the three sides of the source triangle $\triangle ABC$ are defined in the general form $E_i x + F_i y + G_i = 0$, then the distances from the projected observation point to each of the three sides are represented by $l_i = |E_i x + F_i y + G_i| / \sqrt{E_i^2 + F_i^2}$. Likewise, the sign of each contribution is defined as $S_i = (E_i x + F_i y + G_i)/|E_i x + F_i y + G_i|$ for coefficients E_i, F_i, and G_i chosen such that S_i is positive within the lateral extent of the source $\triangle ABC$. Furthermore, the lower and upper limits of integration are defined as $(a_i^2 - b_i^2 - c_i^2)/(2c_i)$ and $(a_i^2 + c_i^2 - b_i^2)/(2c_i)$, respectively. The resulting nearfield pressure generated by $\triangle ABC$ in Figure 2.2 is therefore represented by

$$P(x, y, z;\ k) = \frac{-\rho c v e^{j\omega t}}{2\pi} \sum_{i=1}^{3} \left(\frac{E_i x + F_i y + G_i}{\sqrt{E_i^2 + F_i^2}} \times \int_{\frac{a_i^2 - b_i^2 - c_i^2}{2c_i}}^{\frac{a_i^2 + c_i^2 - b_i^2}{2c_i}} \frac{e^{-jk\sqrt{\sigma^2 + z^2 + l_i^2}} - e^{-jkz}}{\sigma^2 + l_i^2} d\sigma \right) \tag{2.16}$$

Calculations with Eq. 5.4 compute the values of c_i, E_i, F_i, and G_i only once for each edge of $\triangle ABC$, whereas the values of a_i and b_i are calculated once for each (x, y) pair. Unlike the expressions for the impulse response that change depending on the spatial coordinate, Eq. 5.4 is a general formula that computes the nearfield pressure with a single expression that is valid at all points in space.

2.1.4 Transient input waveform

Evaluations of the impulse response and the FNM with time-space decomposition are performed for the Hanning-weighted pulse specified by

$$v(t) = \frac{1}{2} [1 - \cos(2\pi t/W)] \sin(2\pi f_0 t) rect(t/W), \tag{2.17}$$

where $rect(t) = 1$ if $t \in [0, 1]$ and $rect(t) = 0$ otherwise. In the simulations that follow, the input is a Hanning-weighted pulse with a center frequency $f_0 = 2$MHz and a pulse duration $W = 1.5\mu s$. Time-space decomposition performed on this pulse

with $N = 6$ yields the entries in Table 2.1, where the spatial edge wave integral in Eq. 2.13 is evaluated once for each row entry applied to each edge of the source triangle $\triangle ABC$ in Figure 2.2, and then the results are weighted by the temporal basis functions in Table 2.1.

2.1.5 Error calculations

For time-harmonic nearfield pressure calculations, the numerical error $\eta(x,\ y,\ z)$ is defined as the normalized difference between the reference field and the computed field according to

$$\eta(x,y,z) = \frac{|P(x,y,z) - P_{ref}(x,y,z)|}{max|P_{ref}(x,y,z)|}, \tag{2.18}$$

where $P_{ref}(x,y,z)$ is the reference time-harmonic nearfield pressure. For transient nearfield pressure calculations, the numerical error $\eta(x,\ y,\ z)$ between the computed transient field and the reference transient field is defined by

$$\eta(x,\ y,\ z) = \frac{||p(x,\ y,\ z;\ t) - p_{ref}(x,\ y,\ z;\ t)||}{\max_{x,y,z} ||p_{ref}(x,\ y,\ z;\ t)||}, \tag{2.19}$$

where $||\cdot||$ denotes the energy norm used with respect to time, and $p_{ref}(x,\ y,\ z;\ t)$ is the reference transient pressure field as a function of time. The maximum error is defined as $\eta_{max} = \max_{x,y,z} \eta(x,\ y,\ z)$, and this value is computed for both time-harmonic and transient excitations.

2.2 Results

All simulation programs are written in C, then compiled and executed within a Matlab-C language MEX interface. The simulations are performed on an eMachines T3958 personal computer with a 2.93MHz Celeron D processor. The operating sys-

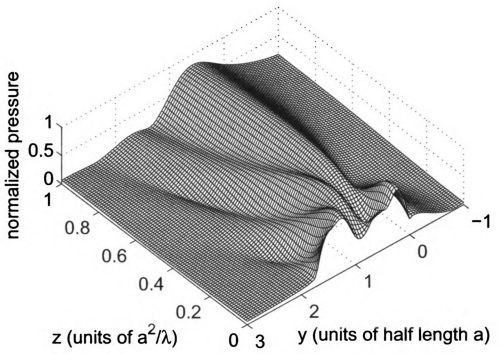

Figure 2.3. Simulated time-harmonic pressure field in the $x = 0$ plane for an equilateral triangular source with sides equal to 4 wavelengths. The reference field is generated by the impulse response method computed with 100,000-point Gauss quadrature.

tem on this computer is Fedora Core 3 Linux. All simulations are run sequentially under similar operating conditions.

2.2.1 Time-harmonic nearfield pressure calculations

Reference pressure distribution

The reference pressure field is computed in Figure 2.3 for an equilateral triangular source with sides equal to 4 wavelengths. In Figure 2.3, the acoustic field is evaluated in the $x = 0$ plane defined in Figure 2.2. The reference nearfield pressure distributions in Figure 2.3 are obtained when the impulse response is calculated for all triangles

with 100,000-point Gauss quadrature. This pressure distribution is selected as the reference because nearfield pressures computed with 100,000 abscissas produce normalized errors that converge to 15 significant digits throughout the nearfield region, which represents the smallest error achievable with double precision arithmetic.

FNM and impulse response calculations

The numerical errors and computation times for the fast nearfield method and the impulse response method are shown in Figure 2.4. For the FNM, the exact impulse response, and Field II with 'use_triangles,' nearfield pressures are evaluated in an 81 by 101 point grid in the $x = 0$ plane as shown in Figure 2.3. Field II with 'use_rectangles' and the smoothed impulse response require an offset due to a singularity on the piston face and are therefore evaluated on a smaller 81 by 86 point grid. The FNM and the exact impulse response are evaluated with Gauss quadrature, and all three integrals corresponding to the three sides of the source triangles are evaluated with the same number of abscissas. The remaining methods that approximate the uniformly sampled impulse response (i.e., Field II and the smoothed impulse response) are evaluated with the midpoint rule as described in the user's guide on the Field II web site (http://www.es.oersted.dtu.dk/staff/jaj/field/). Figure 2.4 shows that the error for a given computation time is consistently smaller with the FNM, where smaller errors are located nearer to the horizontal axis on the bottom of this log-log plot. Likewise, the time required to achieve a given error is consistently smaller with the FNM, since the FNM plot is consistently located to the left of the impulse response plot.

Comparisons between the impulse response and the FNM evaluated for the same peak error are summarized in Table 2.2. For a 10% peak error, the FNM is 4.39 times faster than the impulse response, and for a 1% peak error, the FNM is 3.44 times faster than the impulse response for this grid and piston geometry. Even greater improvements are observed for smaller peak error values due to the rapid convergence

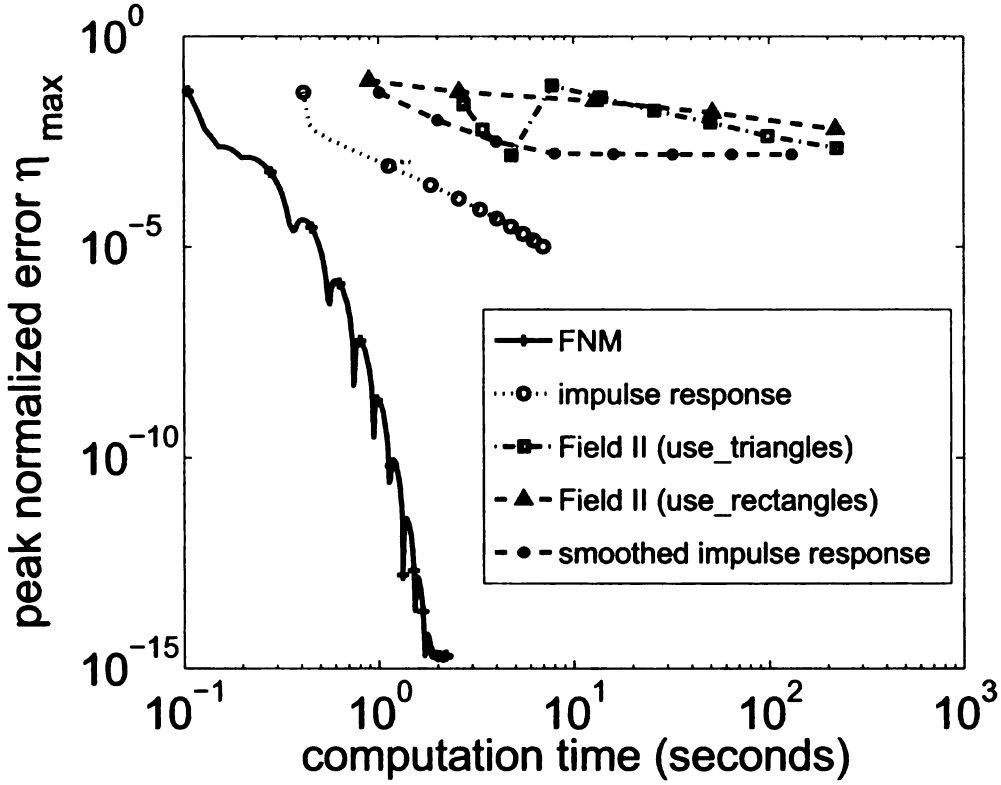

Figure 2.4. Peak normalized error for calculations of nearfield pressures generated by the triangular source in Figure 2.2 plotted as a function of the computation time. The results show that the FNM consistently achieves smaller errors in less time than exact and approximate impulse response calculations for time-harmonic excitations.

of the FNM. Although these values change somewhat for different source and grid geometries, the FNM is consistently faster than the exact and the approximate impulse response for nearfield calculations of time-harmonic pressures.

Field II calculations

The Field II simulation program [10] includes the 'use_triangles' option for calculations that model rectangular and triangular pistons as the superposition of triangular sources. For calculations of time-harmonic pressures with the 'use_triangles' option applied to the source geometry in Figure 2.2, Field II requires a temporal sampling

frequency of f_S = 16MHz to achieve a peak error of 10%. The computation time for Field II with 'use_triangles' is 29.02 times slower than the FNM evaluated on the same grid. For time-harmonic calculations, Field II with the 'use_triangles' option requires a temporal sampling frequency of f_S = 32MHz to achieve a peak error of 1%. This results in a computation time that is 26.43 times longer than that required for the FNM evaluated on the same grid.

Field II also provides a 'use_rectangles' option that introduces a numerical singularity on the piston surface, so the pressure is evaluated on a smaller 81 by 86 point spatial grid that is offset from the piston face. Field II with 'use_rectangles' evaluated on this reduced grid produces a 10% peak error in 0.8908 seconds, which is 9.5 times slower than the FNM on the full 81 by 101 point grid. For a 1% peak error, Field II with 'use_rectangles' computes the result on the restricted grid in 218.2492 seconds, which is 1697 times slower than the FNM on the full grid.

Smoothed impulse response calculations

Time-harmonic calculations with the smoothed impulse response [35] evaluate the pressure on a smaller 81 by 86 point spatial grid that is offset from the piston face. The offset is required for smoothed impulse response calculations so that the singularity in Eq. 2.7 at the piston face is avoided. For calculations of the time-harmonic pressure generated by the triangular source depicted in Figure 2.2 and evaluated within an 81 by 86 point subset of the grid shown in Figure 2.3, the smoothed impulse calculation converges to a peak error of 10% with a temporal sampling rate of f_S = 32MHz. This computation is completed in 1.0105 seconds, which is 10.74 times longer than the time required for the corresponding FNM calculation evaluated on a larger 81 by 101 point spatial grid. Time-harmonic calculations with the smoothed impulse response achieve a peak error of 1% for a temporal sampling rate of f_S = 128MHz. This computation is completed in 3.9983 seconds, which is 31.26 times longer than

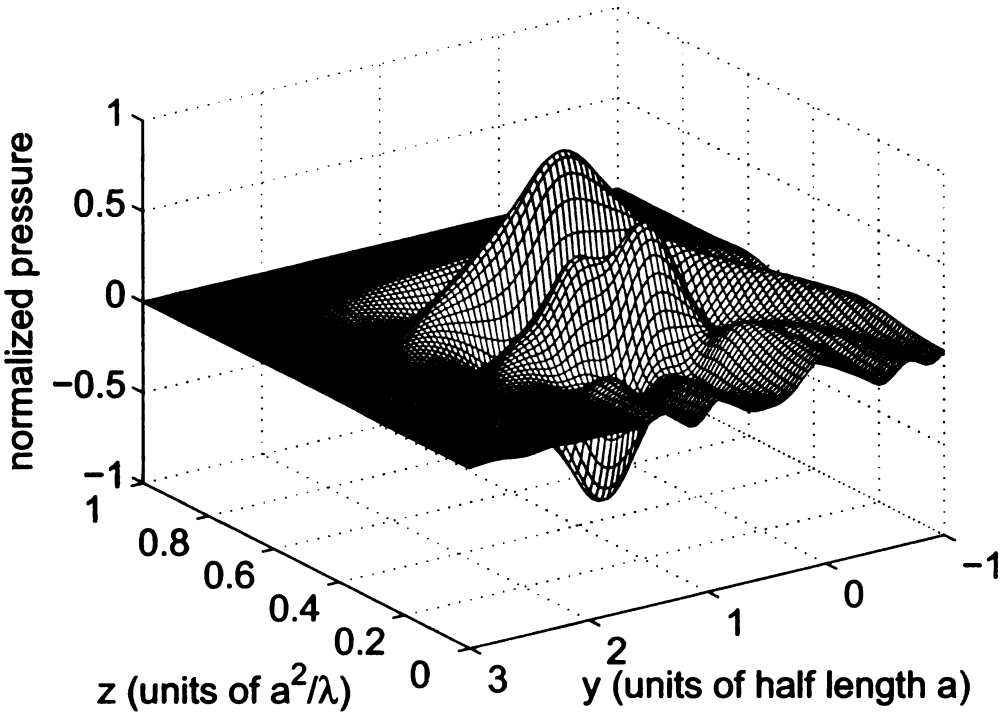

Figure 2.5. Simulated transient pressure field in the $x = 0$ plane for an equilateral triangular source with sides equal to 4 wavelengths. For this calculation, the excitation is the Hanning-weighted pulse in Eq. 2.17, and the transient pressure is evaluated at 85 time points in an 81 by 101 point grid. The result is plotted at 1.8125μs after the initiation of the input pulse.

time required to obtain the FNM result with 1% peak error in Table 2.2.

2.2.2 Transient nearfield pressure calculations

Reference pressure distribution

The reference nearfield pressure distribution for transient excitations is calculated with impulse response waveforms that are sampled at $f_S = 524.288$GHz, zero padded, and convolved with FFTs. The resulting temporal variations in the nearfield pressure, which are evaluated for an equilateral triangular piston with 4 wavelengths on

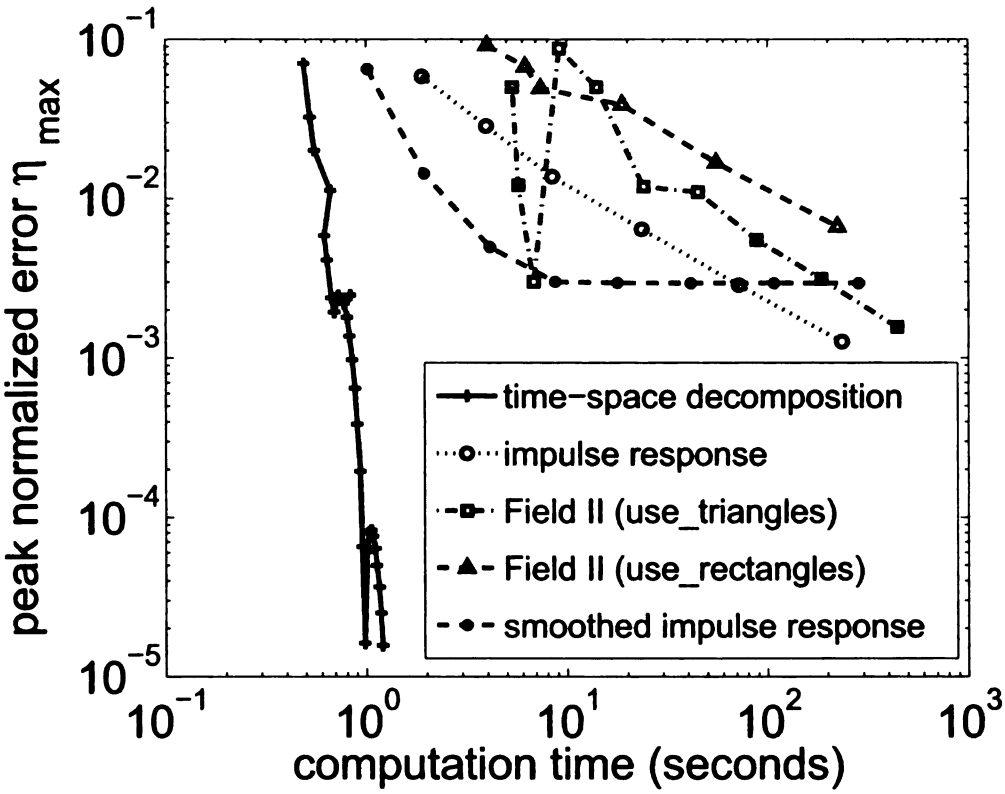

Figure 2.6. The peak normalized error plotted as a function of the computation time for the FNM/time-space decomposition method, the impulse response method, and methods that approximate the impulse response. These errors and times are evaluated for transient nearfield calculations of an equilateral triangular source with sides equal to 4 wavelengths. The excitation for these calculations is a Hanning-weighted pulse with a center frequency of 2MHz.

each side, are then downsampled and stored at $f_S = 16\text{MHz}$. The reference field is calculated for a sound speed of $c = 1.5mm/\mu s$ on an 81 by 101 point spatial grid evaluated at 85 time points, and the result at time $t = 1.8125\mu s$ is shown in Figure 2.5. This error reference is accurate to 5 significant digits for calculations in the $x = 0$ plane.

FNM and impulse response calculations

Figure 2.6 shows the numerical error plotted as a function of the computation time for the FNM with time-space decomposition and calculations based on the impulse response method. All methods, except for Field II with 'use_rectangles' and the smoothed impulse response, are evaluated relative to an 81 by 101 spatial point by 85 time point reference transient pressure distribution. Field II with 'use_rectangles' and the smoothed impulse response are singular at the piston face, so a smaller 81 by 86 point spatial grid that incorporates an offset from the piston face is again required for transient field computations. The input for the reference is generated by a Hanning-weighted pulse with a center frequency of $f_0 = 2$MHz. The transient nearfield pressures are compared for $f_S = 16$MHz, which is the original sampling rate for the FNM calculations and the resulting rate after downsampling for impulse response calculations. Figure 2.6 shows that the FNM with time-space decomposition is consistently faster than the impulse response and the methods that approximate the impulse response. Similarly, Figure 2.6 indicates that the FNM with time-space decomposition achieves much smaller numerical errors than the impulse response and approximations to the impulse response.

Table 2.3 shows that the FNM with time-space decomposition achieves a 10% peak error with 5 Gauss abscissas in 0.4867 seconds. To achieve a 1% peak error, the FNM with time-space decomposition needs 9 Gauss abscissas and the computation time is 0.6160 seconds. In contrast, the impulse response method achieves a peak error of 10% with a sampling frequency of $f_S = 128$MHz in 1.8911 seconds. To achieve a peak error of 1%, the impulse response method requires a sampling frequency of $f_S = 1$GHz and a computation time of 23.5241 seconds. Thus, the reduction in the computation time with time-space decomposition applied to the FNM relative to the impulse response is a factor of 3.89 for a peak error of 10% and a factor of 38.19 for a peak error of 1%.

Field II calculations

The Field II result obtained with the 'use_triangles' option for the transient excitation in Eq. 2.17 requires a sampling frequency of $f_S = 16$MHz to achieve a peak error of 10%, and the computation time for this combination of parameters is 5.3317 seconds. For a peak error of 1%, Field II with the 'use_triangles' option requires a sampling frequency of $f_S = 64$MHz, and the computation time is 6.8078 seconds. Therefore, the FNM with time-space decomposition is 10.95 times faster than Field II with 'use_triangles' for a peak error of 10% and 11.05 times faster for a peak error of 1%.

Transient Field II calculations that subdivide the aperture into small rectangular sources with 'use_rectangles' reach a peak error of 10% with a temporal sampling frequency of $f_S = 32$MHz in 3.9926 seconds. Field II with 'use_rectangles' achieves a peak error of 1% with a temporal sampling frequency of $f_S = 48$MHz in 221.6569 seconds. Therefore, the FNM with time-space decomposition is 8.2 times faster than Field II evaluated with subdivided rectangular sources for a 10% peak error and 359.81 times faster than Field II evaluated with subdivided rectangular sources for a 1% peak error.

Smoothed impulse response calculations

Transient calculations with the smoothed impulse response in Eq. 2.7 evaluate the pressure at 85 time points on a smaller 81 by 86 point spatial grid that is offset from the piston face. The offset is required in order to avoid the singularity in Eq. 2.7 on the piston face. For calculations of the time-harmonic pressure generated by the triangular source depicted in Figure 2.2 and evaluated within an 81 by 86 point subset of the grid shown in Figure 2.3, the smooth impulse calculation converges to a peak error of 10% with a temporal sampling rate of $f_S = 32$MHz. This computation is completed in 1.0122 seconds, which is 2.08 times longer than the time required for the corresponding FNM calculation evaluated on a larger 81 by 101 point spatial grid.

Time-harmonic calculations with the smoothed impulse response achieve a peak error of 1% for a temporal sampling rate of $f_S = 128$MHz. This computation is completed in 4.1261 seconds, which is 6.7 times longer than time required to obtain the FNM result with 1% peak error in Table 2.2.

2.3 Discussion

2.3.1 Time and error calculations

While computer processor speed and memory has increased substantially in recent decades, the size and complexity of ultrasound therapy and imaging simulations has grown accordingly. Simulations of large ultrasound therapy arrays are now applied to thousands of transducer elements and computational volumes spanning hundreds of wavelengths in three dimensions, and simulations of diagnostic imaging arrays have demonstrated a corresponding increase in the number of active elements and the number of scatterers. As a result, large simulations of ultrasound phased arrays can require 24 hours or longer on modern computers.

For these large simulations, the evaluation of computational time and numerical error is essential. The computation time remains the primary bottleneck in these time-consuming calculations, but fair comparisons of computation time also require calculations of the numerical error. In recent years, evaluations of the numerical error have been neglected due to the slow convergence of the impulse response and methods that approximate the impulse response. Figures 2.4 and 2.6 demonstrate this slow convergence, which is further emphasized by the time-harmonic reference field that requires 100,000 Gauss abscissas for convergence to 15 significant digits and by the transient reference field that requires a sampling frequency of f_S =524.288GHz for convergence to 5 significant digits.

The rapid convergence of the FNM demonstrated in Figures 2.4 and 2.6 suggests

that the FNM is ideal for calculating nearfield pressure reference fields. In Figure 2.4, time-harmonic FNM calculations converge within 15 significant digits in less than one-third of the time that the impulse response requires for convergence within 5 significant digits. Likewise, in Figure 2.6, transient FNM calculations with time-space decomposition converges within 5 significant digits in less than one-fifth of the time that the impulse response requires for convergence within 2 significant digits. In these simulations of a triangular piston source excited by a pulse with a center frequency of 2MHz, impulse response calculations require a sampling rate of 1GHz to achieve only 2 significant digits of accuracy, whereas the FNM with time-space decomposition requires only 9 Gauss abscissas applied to each integral and a sampling rate of 16MHz to achieve 2 significant digits of accuracy throughout the nearfield region.

2.3.2 Advantages of the FNM for time-harmonic and transient calculations

The computational advantages of the FNM are obtained from several sources. First, the FNM replaces time-consuming calculations of inverse trigonometric functions with a ratio of polynomials in the integrand. This reduces the computation time without increasing the numerical error. Second, the FNM reduces the numerical error by subtracting a singularity in the integrand. This step, which reduces the numerical error without significantly increasing the computation time, is particularly effective in eliminating numerical problems that occur along the edge of the source and throughout the paraxial region. Third, the FNM defines a single analytical expression that describes the pressure throughout the nearfield region, whereas the impulse response requires multiple expressions to define the field generated by a single source. Thus, relative to calculations that employ exact or approximate calculations of the impulse response, convergence is faster with the FNM, and the FNM expressions are easier to evaluate.

The advantage of the FNM with time-space decomposition is that an integral expression with temporal and spatial dependencies is replaced with an equivalent expression that instead evaluates N spatial integrals for each edge of the triangular source and weights the result of each integral with an analytical temporal term. This results in greatly reduced overhead for transient nearfield calculations, considering that the impulse response requires sampling rates of $f_S = 128\text{MHz}$ for a peak error of 10% and $f_S = 1\text{GHz}$ for a peak error of 1% for the source geometry in Figure 2.2. The FNM eliminates these high sampling rates, which therefore facilitates much more efficient utilization of computer memory.

2.3.3 Field II

The Field II calculations with 'use_triangles' are evaluated within the same 81 by 101 spatial grid defined previously for these nearfield calculations, whereas the same calculations with subdivided rectangular subapertures (i.e., 'use_rectangles') are evaluated in an 81 by 86 spatial grid that includes an offset from the piston face. The offset is required for these nearfield calculations, otherwise the error grows excessively large on the piston face, which translates into much longer computation times for 10% and 1% peak errors. This occurs because subdividing the aperture introduces a numerical singularity on the piston face. Although Field II reduces the sampling frequency relative to other impulse response calculations, the exact impulse response consistently outperforms Field II for these time-harmonic nearfield calculations, and the FNM evaluated with Gauss quadrature outperforms both of these by a wide margin. Furthermore, the FNM with time-space decomposition is also considerably faster than Field II for transient nearfield calculations, and the FNM with time-space decomposition, unlike Field II with 'use_rectangles,' allows the computational grid to extend up to the piston face.

2.3.4 Smoothed impulse response

Unlike the FNM and the exact impulse response, the smoothed impulse response requires an offset from the piston face for nearfield calculations. This offset is required because the denominator in Eq. 2.7 produces a numerical singularity on the piston face. Despite evaluating the nearfield pressure on a smaller 81 by 86 point spatial grid, the smoothed impulse response is slower than the FNM and the exact impulse response for time-harmonic calculations, as demonstrated in Figure 2.4 and Table 2.2. The exact impulse response is faster than the smoothed impulse response for these time-harmonic calculations because the exact impulse response is evaluated with Gauss quadrature, and Gauss quadrature generally converges much faster than other numerical integration methods that uniformly sample the integrand. For transient calculations with both exact and approximate impulse response expressions, uniform sampling is required for convolutions with the FFT. In these transient calculations, the smoothed impulse response gains some advantage over the exact impulse response by evaluating the pressure at a smaller number of spatial grid points and by reducing the problems with aliasing at higher frequencies. Nevertheless, as demonstrated in Figures 2.4 and 4.3, the smoothed impulse response converges more slowly than the FNM for time-harmonic and transient nearfield calculations.

2.4 Conclusion

A fast nearfield method is presented for numerical calculations of the pressure generated by a triangular source. For time-harmonic nearfield computations, the FNM expression in Eq. 2.10 achieves smaller peak errors in less time than the exact impulse response, the smoothed impulse response, and the Field II program. The results show that the FNM is 4.39 times faster than the exact impulse response for a 10% peak error, and the FNM is 3.44 times faster than the exact impulse response for

a 1% peak error. The FNM is at least an order of magnitude faster than Field II and the smoothed impulse response for time-harmonic calculations compared at 10% and 1% peak error values. In transient nearfield computations, the FNM in Eq. 2.11 combined with time-space decomposition achieves a substantial reduction in the computation time relative to exact and approximate impulse response calculations for a given peak error value. Transient nearfield pressures are evaluated with a Hanning-weighted broadband pulse, and the resulting transient calculation is transformed into the superposition of six spatial integrals. The results demonstrate that the FNM with time-space decomposition is 3.89 and 38.19 times faster than the impulse response for peak errors of 10% and 1%, respectively, evaluated on an 81 by 101 spatial grid at 85 time points. Comparisons between smoothed impulse response results evaluated on the smaller 81 by 86 point offset spatial grid and the FNM with time-space decomposition evaluated on the larger 81 by 101 point spatial grid indicate that the FNM with time-space decomposition is 2.08 times faster than the smoothed impulse response for a 10% peak error and the FNM with time-space decomposition is 6.7 times faster for a 1% peak error. Compared to the Field II program, the FNM is at least an order of magnitude faster for 10% and 1% peak error values. The results also suggest that the FNM, which eliminates the numerical problems that are encountered in exact and approximate impulse response calculations, provides a superior reference for nearfield pressure calculations evaluated with time-harmonic and transient inputs.

Table 2.2. Number of Gauss abscissas, computation times, and computation times relative to the FNM that describe the reduction in the computation time achieved with the fast nearfield method relative to the impulse response and methods that approximate the impulse response for peak errors of 10% and 1%. The FNM and exact impulse response results are evaluated for time-harmonic calculations on a 81 by 101 point grid located in the $x = 0$ plane, and the Field II and smoothed impulse response results are evaluated on an 81 by 86 point grid in the $x = 0$ plane that is slightly offset from the transducer face. (a) For a 10% peak error and (b) for a 1% peak error.

(a)

	Time-Harmonic Nearfield Computations				
	10% peak error				
	FNM	impulse response	Field II 'use_triangles'	smooth imp. resp.	Field II 'use_rectangles'
Parameters	N=8	N=11	f_S = 16MHz	f_S = 32 MHz	f_S = 32MHz N=16×16
Time	0.0938s	0.4112s	2.7212s	1.0051s	0.8908
Computation time relative to the FNM	1×	4.39×	29.02×	10.72×	9.5×

(b)

	Time-Harmonic Nearfield Computations				
	1% peak error				
	FNM	impulse response	Field II 'use_triangles'	smooth imp. resp.	Field II 'use_rectangles'
Parameters	N=11	N=12	f_S = 32MHz	f_S = 128 MHz	f_S = 48MHz N=256×256
Time	0.1286s	0.4419s	3.3993s	4.0130s	218.2492s
Computation time relative to the FNM	1×	3.44×	26.43×	31.21×	1697.00×

Table 2.3. Comparisons of computation times, input parameters, and computation times relative to the FNM that describe the reduction in the computation time achieved with the FNM and time-space decomposition relative to the exact and approximate impulse response for specified maximum errors of 10% and 1%. For FNM, impulse response, Field II calculations with 'use_triangles', and Field II calculations with 'use_rectangles', these transient results are evaluated in an 81 by 101 spatial point by 85 time point grid, and for the smoothed impulse response, the results are valued at the same temporal points in a restricted 81 by 86 point spatial grid. (a) For a 10% peak error and (b) for a 1% peak error.

(a)

	Transient Nearfield Computations				
	10% peak error				
	FNM	impulse response	Field II 'use_triangles'	smoothed imp. resp.	Field II 'use_rectangles'
Parameters	N=5	$f_S = 128$ MHz	$f_S = 16$MHz	$f_S = 32$ MHz	$f_S = 32$MHz N=16×16
Time	0.4867s	1.8911s	5.3317s	1.0122s	3.9926s
Computation time relative to the FNM	1×	3.89×	10.95×	2.08×	8.2×

(b)

	Transient Nearfield Computations				
	1% peak error				
	FNM	impulse response	Field II 'use_triangles'	smoothed imp. resp.	Field II 'use_rectangles'
Parameters	N=9	$f_S = 1$ GHz	$f_S = 64$MHz	$f_S = 128$ MHz	$f_S = 48$MHz N=256×256
Time	0.6160s	23.5241s	6.8078s	4.1261s	221.6569s
Computation time relative to the FNM	1×	38.19×	11.05×	6.70×	359.81×

CHAPTER 3

A 2D Fast Nearfield Method for Apodized Rectangular Pistons

Although several methods, including the Rayleigh-Sommerfeld integral [6] and the Field II program [10, 11], calculate the pressures generated by apodized rectangular pistons, the numerical performance of these methods suffers in the nearfield region. The numerical evaluation of the Rayleigh-Sommerfeld integral converges slowly in the nearfield region because of the singularity introduced by the $1/R$ term, which approaches infinity when R approaches zero. The Field II program subdivides a rectangular piston into smaller rectangles and computes the pressure using the far field approximation for the impulse response of the velocity potential, which also contains a $1/R$ term. Thus, the Field II program generates relatively large errors and converges slowly in the nearfield region, especially near the piston face. To address this problem for circular pistons, the FNM has been recently extended to include axisymmetric particle velocity distributions, and the resulting 2D integral also demonstrates rapid convergence [37]. However, this apodized FNM expression is specific to pistons with circular or cylindrical symmetry, and methods for modeling apodized rectangular pistons are still needed.

To improve the performance of nearfield calculations for apodized rectangular pistons, an apodized FNM expression is derived from the FNM expression for uniformly excited rectangular pistons. The derivation of the apodized FNM for rectangular pistons begins by subdividing the piston into small uniformly excited subelements. The total pressure is obtained by superposing by the pressure produced by all of the subelements. After performing a summation variable exchange and integrating by parts, the apodized FNM expression for rectangular pistons is obtained. Next, the apodized FNM for transient pressure calculations is obtained by inverse Fourier transforming the time-harmonic apodized FNM expression. The apodized FNM expression, the Rayleigh-Sommerfeld integral, and the Field II program are then evaluated in the nearfield of a square piston that extends 4 wavelengths in both directions. The results of time-harmonic and transient computations indicate that, when compared to calculations performed with the Rayleigh-Sommerfeld integral and the Field II program, 1) the apodized FNM achieves the smallest errors for a given amount of time, and 2) the apodized FNM requires the least time to achieve a given error.

3.1 Existing calculation methods

3.1.1 The Rayleigh-Sommerfeld integral

The time-harmonic pressure generated by an apodized rectangular source is also computed with the Rayleigh-Sommerfeld integral [6] via

$$p_{Rayleigh}(x,y,z;k) = \frac{j\omega\rho v_0 e^{j\omega t}}{2\pi} \int_0^a \int_0^b f(\mu,\nu) \frac{e^{-jkR}}{R} d\mu d\nu, \tag{3.1}$$

where ω is the excitation frequency in radians per second, ρ is the density of the medium, c is the speed of sound, v_0 is the constant normal particle velocity evaluated on the surface of the rectangular source, k is the wavenumber, and

$R = \sqrt{(x-\mu)^2 + (y-\nu)^2 + z^2}$ is the distance between the source point $(\mu, \nu,\ 0)$ and the observation point $(x,\ y,\ z)$. The transient pressure generated by an apodized rectangular source with a temporal excitation component $v(t)$ is given by the inverse Fourier transform of Eq. (3.1), which yields

$$p_{Rayleigh}(x, y, z; t) = \frac{\rho}{2\pi} \int_0^a \int_0^b f(\mu, \nu) \frac{\dot{v}(t - R/c)}{R} d\mu d\nu, \tag{3.2}$$

where $\dot{v}(t)$ is the time derivative of the input excitation pulse $v(t)$.

3.1.2 The Field II program

The Field II program [10] is a software package that computes transient and steady-state pressures generated by phased arrays and individual ultrasound transducers. The Field II program with the *use_rectangles* option divides each piston source into small rectangular elements and applies the far field approximation of the spatial impulse response to each small rectangular element [11], where Field II specifies the apodization at the center point of each small rectangular element. The accuracy of the Field II program is dependent on two factors, namely the sampling frequency and the number of small rectangular elements. With an increase in the sampling frequency or the number of small rectangular elements, Field II achieves smaller errors, but the computation time increases accordingly.

3.2 Fast nearfield method for apodized rectangular pistons

In the derivation that follows, each observation point is denoted by (x, y, z), and each source point is denoted by $(\mu, \nu, 0)$. Figure 3.1 shows the coordinate system used in the derivation and subsequent evaluations. The rectangular source is located in the

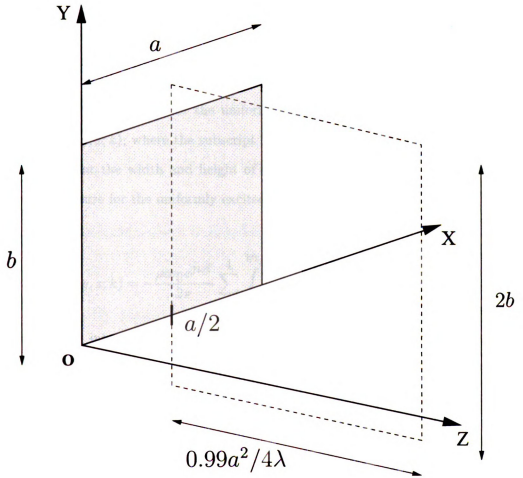

Figure 3.1. Orientation of the computational grid relative to the rectangular source. The rectangular source, which has width a and height b, lies in the $z = 0$ plane. The dashed lines define the extent of the computational grid in the $x = a/2$ plane. The extent of the computational grid is $2b$ by $0.99a^2/4\lambda$ in the y and z directions, respectively.

$z = 0$ plane, and the origin of the coordinate system O coincides with the lower left corner of the rectangular source. The apodization function of the source is given by $f(\mu, \nu)$, which is zero outside of the rectangular source. The width of the rectangular source is a and the height is b.

The FNM expression for a rectangular piston that is excited uniformly is given by McGough [8]. A more general unapodized FNM expression for a rectangular piston is obtained from the expression in Chen and McGough [12] for a triangular piston. Here, the FNM expression for the uniformly excited rectangular piston is denoted by $p_0[\mu, \nu](x, y, z; k)$, where the subscript $'0'$ indicates the uniform excitation and μ and ν represent the width and height of the rectangular source, respectively. The nearfield pressure for the uniformly excited piston is given by

$$p_0[\mu, \nu](x, y, z; k) = -\frac{\rho c v_0 e^{j\omega t}}{2\pi} \sum_{i=1}^{4} \int_{n_i}^{m_i} h_i \frac{e^{-jk\sqrt{\sigma^2+z^2+h_i^2}} - e^{-jkz}}{\sigma^2 + h_i^2} d\sigma, \quad (3.3)$$

where σ is an integration variable as defined in [8, 12]. The values of m_i and n_i, which are functions of μ and ν, represent the upper limits and lower limits of the integral, respectively. In Eq. (3.3), the values of (m_i, n_i) are $(m_1, n_1) = (m_2, n_2) = (\mu - x,\ -x)$ and $(m_3, n_3) = (m_4, n_4) = (\nu - y,\ -y)$, and the values of h_i are $h_1 = y$, $h_2 = \nu - y$, $h_3 = x$, and $h_4 = \mu - x$ for $i = 1, 2, 3,$ and 4, respectively. According to Eq. (3.3), there are two special cases, namely

$$p_0[0, \nu](x, y, z; k) = 0 \text{ and } p_0[\mu, 0](x, y, z; k) = 0, \quad (3.4)$$

where the subelement has zero width or height, respectively. These special cases are utilized in the following derivation of the apodized FNM expression for a rectangular source.

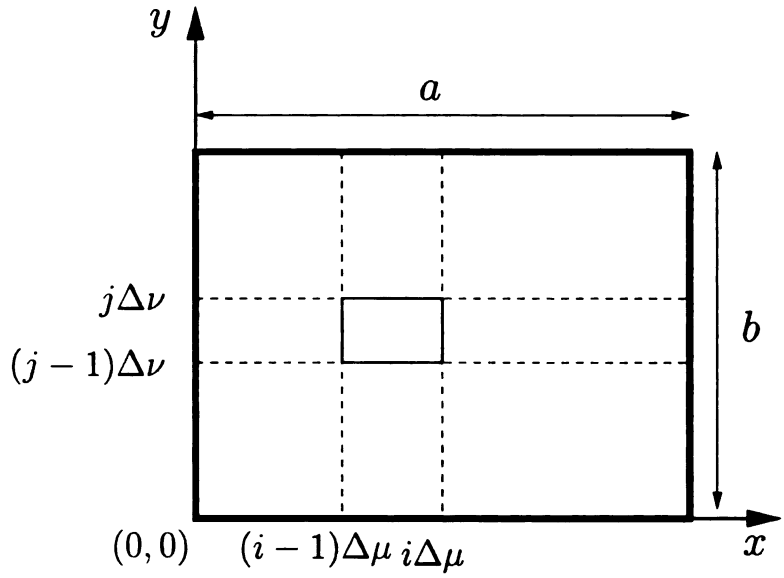

Figure 3.2. The decomposition of an apodized rectangular source into smaller rectangles, where each small rectangle is $\Delta\mu$ wide and $\Delta\nu$ high. The apodization function $f(\mu, \nu)$ is defined as constant over each small rectangle.

3.2.1 Steady-state Apodized FNM Expression

The pressure field $p_{apod}(x, y, z; k)$ is obtained by subdividing the rectangular source into $N \times N$ small rectangles, where the subscript *apod* indicates that the pressure is computed with the apodization function $f(\mu, \nu)$. One of these small rectangles is depicted inside of the rectangular source in Figure 3.2. The values $\Delta\mu = a/N$ and $\Delta\nu = b/N$ denote the width and the height of each small rectangle in the x and y directions, respectively, and $S[i, j]$ represents the rectangle at the ith column and jth row of the subdivision. The four coordinates of the vertices of $S[i, j]$ are given by $((i-1)\Delta\mu,\ (j-1)\Delta\mu)$, $(i\Delta\mu,\ (j-1)\Delta\mu)$, $(i\Delta\mu,\ j\Delta\mu)$, and $((i-1)\Delta\mu,\ j\Delta\mu)$ for the lower left, lower right, upper right, and upper left coordinates, respectively. The expression $p[i, j] = p[i\Delta\mu, j\Delta\nu](x, y, z)$ represents the pressure produced by the uniformly excited rectangular source having width $i\Delta\mu$ and height $j\Delta\nu$, where the lower left corner is located at $(0, 0)$, and the aperture function over the rectangle

$S[i,j]$ is defined by $q[i,j] = f(i\Delta\mu,\ j\Delta\nu)$. The total pressure $p_{apod}(x,y,z;k)$ is approximated by

$$p_{apod}(x,y,z;k) \simeq \sum_{i=1}^{N}\sum_{j=1}^{N} q[i,j](p[i,j]+p[i-1,j-1]-p[i,j-1]-p[i-1,j]). \quad (3.5)$$

According to Eq. (3.4), $p[l,0] = 0$, and $p[0,l] = 0$, $l = 1, \cdots, N$. By utilizing these restrictions and rearranging Eq. (3.5),

$$p_{apod}(x,y,z;k) \simeq$$

$$\sum_{i=1}^{N-1}\sum_{j=1}^{N-1} p[i,j]\left(\frac{(q[i+1,j+1]-q[i+1,j])-(q[i,j+1]-q[i,j])}{\Delta\nu\Delta\mu}\Delta\nu\Delta\mu\right)$$

$$+\sum_{i=1}^{N-1} p[i,N]\left(-\frac{q[i+1,N]-q[i,N]}{\Delta\mu}\right)\Delta\mu$$

$$+\sum_{j=1}^{N-1} p[N,j]\left(-\frac{q[N,j+1]-q[N,j]}{\Delta\nu}\right)\Delta\nu + p[N,N]q[N,N] \quad (3.6)$$

is obtained. Letting $N \to \infty$ such that $\Delta\mu \to 0$ and $\Delta\nu \to 0$, Eq. (3.6) becomes

$$p_{apod}(x,y,z;k) = p_{apod1}(x,y,z;k) + p_{apod2}(x,y,z;k)$$

$$+p_{apod3}(x,y,z;k) + p_{apod4}(x,y,z;k), \quad (3.7)$$

where $p_{apod1}(x,y,z;k) = \int_0^a \int_0^b \frac{\partial^2 f(\mu,\nu)}{\partial\mu\partial\nu} p_0[\mu,\nu](x,y,z;k)d\mu d\nu$,
$p_{apod2}(x,y,z;k) = -\int_0^a \frac{\partial f(\mu,b)}{\partial\mu} p_0[\mu,b](x,y,z;k)d\mu$,
$p_{apod3}(x,y,z;k) = -\int_0^b \frac{\partial f(a,\nu)}{\partial\nu} p_0[a,\nu](x,y,z;k)d\nu$,
and $p_{apod4}(x,y,z;k) = f(a,b)p_0[a,b](x,y,z;k)$. Within these expressions,

$p_0[\mu,\nu](x,y,z;k)$ is the single integral from Eq. (3.3), so $p_{apod1}(x,y,z;k)$ is actually a triple integral, $p_{apod2}(x,y,z;k)$ and $p_{apod3}(x,y,z;k)$ are double integrals that admit further simplification, and $p_{apod4}(x,y,z;k)$ is already simplified.

After substituting the uniformly excited fast nearfield method expression $p_0[\mu,\nu](x,y,z;k)$ from Eq. (3.3), $p_{apod1}(x,y,z;k)$ in Eq. (3.7) becomes

$$p_{apod1}(x,y,z;k) = -\frac{\rho c v_0 e^{j\omega t}}{2\pi} \sum_{i=1}^{4} \int_{n_i}^{m_i} \int_0^a \int_0^b \frac{\partial^2 f(\mu,\nu)}{\partial\mu\partial\nu} \times h_i \frac{e^{-jk\sqrt{\sigma^2+z^2+h_i^2}} - e^{-jkz}}{\sigma^2+h_i^2} d\sigma d\mu d\nu. \tag{3.8}$$

The derivation of the first two triple integrals

$$p_{apod1,i=1,2}(x,y,z;k) = -\frac{\rho c v_0 e^{j\omega t}}{2\pi} \int_{-x}^{\mu-x} \int_0^a \int_0^b \frac{\partial^2 f(\mu,\nu)}{\partial\mu\partial\nu} \times h_i \frac{e^{-jk\sqrt{\sigma^2+z^2+h_i^2}} - e^{-jkz}}{\sigma^2+h_i^2} d\sigma d\mu d\nu \tag{3.9}$$

is outlined here, where $p_{apod1}(x,y,z;k) = p_{apod1,i=1}(x,y,z;k) + p_{apod1,i=2}(x,y,z;k) + p_{apod1,i=3}(x,y,z;k) + p_{apod1,i=4}(x,y,z;k)$. Let $g_{i=1,2}(\mu)$ denote the integral

$$g_{i=1,2}(\mu) = \int_{-x}^{\mu-x} h_i \frac{e^{-jk\sqrt{\sigma^2+z^2+h_i^2}} - e^{-jkz}}{\sigma^2+h_i^2} d\sigma, \tag{3.10}$$

where $h_1 = y$ and $h_2 = \nu - y$ as indicated above. The function $g_{i=1,2}(\mu)$ is defined in terms of a variable in the upper limit of the integral, so the derivative of $g_{i=1,2}(\mu)$ with respect to μ is

$$g'_{i=1,2}(\mu) = h_i \frac{e^{-jk\sqrt{(\mu-x)^2+z^2+h_i^2}} - e^{-jkz}}{(\mu-x)^2+h_i^2}. \tag{3.11}$$

After integrating by parts with respect to the variable μ, $p_{apod1,i=1,2}(x,y,z;k)$ is rewritten as

$$p_{apod1,i=1,2}(x,y,z;k) = -\frac{\rho c v_0 e^{j\omega t}}{2\pi} \int_0^b \left[\frac{\partial f(\mu,\nu)}{\partial \nu} g_{i=1,2}(\mu)|_0^a \right.$$

$$\left. - \int_0^a \frac{\partial f(\mu,\nu)}{\partial \nu} g'_{i=1,2}(\mu) d\mu \right] d\nu. \tag{3.12}$$

According to Eq. (3.10), $g_{i=1,2}(0) = 0$. Substituting the expression for $g'_{i=1,2}(\mu)$ into Eq. (3.12) and performing an exchange of variables yields the following analytically equivalent expression for the first triple integral,

$$p_{apod1,i=1,2}(x,y,z;k) = -\frac{\rho c v_0 e^{j\omega t}}{2\pi} \int_0^a \int_0^b \left(\frac{\partial f(a,\nu)}{\partial \nu} - \frac{\partial f(\mu,\nu)}{\partial \nu} \right)$$

$$\times h_i \frac{e^{-jk\sqrt{(\mu-x)^2+z^2+h_i^2}} - e^{-jkz}}{(\mu-x)^2 + h_i^2} d\mu d\nu. \tag{3.13}$$

The simplification of the third and forth triple integrals

$$p_{apod1,i=3,4}(x,y,z;k) = -\frac{\rho c v_0 e^{j\omega t}}{2\pi} \int_{-y}^{\mu-y} \int_0^a \int_0^b \frac{\partial^2 f(\mu,\nu)}{\partial \mu \partial \nu}$$

$$\times h_i \frac{e^{-jk\sqrt{\sigma^2+z^2+h_i^2}} - e^{-jkz}}{\sigma^2 + h_i^2} d\sigma d\mu d\nu \tag{3.14}$$

in Eq. (3.8) is outlined in the following. Let $g_{i=3,4}(\nu)$ denote the integral

$$g_{i=3,4}(\nu) = \int_{-y}^{\nu-y} h_i \frac{e^{-jk\sqrt{\sigma^2+z^2+h_i^2}} - e^{-jkz}}{\sigma^2 + h_i^2} d\sigma, \tag{3.15}$$

where $h_3 = x$ and $h_4 = \mu - x$ as indicated above. The function $g_{i=3,4}(\nu)$ is defined in terms of a variable in the upper limit of the integral, so the derivative of $g_{i=3,4}(\nu)$ with respect to ν is

$$g'_{i=3,4}(\nu) = h_i \frac{e^{-jk\sqrt{(\nu-y)^2+z^2+h_i^2}} - e^{-jkz}}{(\nu-y)^2 + h_i^2}. \tag{3.16}$$

After integrating by parts with respect to the variable ν, $p_{apod1,i=3,4}(x,y,z;k)$ is rewritten as

$$p_{apod1,i=3,4}(x,y,z;k) = -\frac{\rho c v_0 e^{j\omega t}}{2\pi} \int_0^a \left[\frac{\partial f(\mu,\nu)}{\partial \mu} g_{i=3,4}(\nu)\Big|_0^b - \int_0^b \frac{\partial f(\mu,\nu)}{\partial \mu} g'_{i=1,2}(\nu) d\nu \right] d\mu. \tag{3.17}$$

According to Eq. (3.10), $g_{i=3,4}(0) = 0$. Substituting the expression for $g'_{i=3,4}(\nu)$ into Eq. (3.12) and performing an exchange of variables yields the following analytically equivalent expression for the first triple integral,

$$p_{apod1,i=3,4}(x,y,z;k) = -\frac{\rho c v_0 e^{j\omega t}}{2\pi} \int_0^a \int_0^b \left(\frac{\partial f(\mu,b)}{\partial \mu} - \frac{\partial f(\mu,\nu)}{\partial \mu} \right) \times h_i \frac{e^{-jk\sqrt{(\nu-y)^2+z^2+h_i^2}} - e^{-jkz}}{(\nu-y)^2 + h_i^2} d\mu d\nu. \tag{3.18}$$

By substituting $p_0[\mu,b](x,y,z;k)$ and $p_0[a,\nu](x,y,z;k)$ from Eq. (3.3) into $p_{apod2}(x,y,z;k)$ and $p_{apod3}(x,y,z;k)$ and by using integration by parts, $p_{apod2}(x,y,z;k)$ and $p_{apod3}(x,y,z;k)$ are converted into the sum of two single integrals and two double integrals, while $p_{apod4}(x,y,z;k)$ is already a single integral. After the four terms in Eq. (3.7) are added and common terms are canceled, the complete FNM expression for an apodized rectangular piston is:

$$p_{apod}(x,y,z;\ k) = -\frac{\rho c v_0 e^{j\omega t}}{2\pi}\sum_{i=1}^{4}\int_0^a\int_0^b T_{1i}h_{1i}\frac{e^{-jk\sqrt{\alpha_{1i}^2+z^2+h_{1i}^2}}-e^{-jkz}}{\alpha_{1i}^2+h_{1i}^2}d\mu d\nu$$

$$-\frac{\rho c v_0 e^{j\omega t}}{2\pi}\sum_{i=1}^{4}\int_{n_i}^{m_i} T_{2i}h_{2i}\frac{e^{-jk\sqrt{\alpha_{2i}^2+z^2+h_{2i}^2}}-e^{-jkz}}{\alpha_{2i}^2+h_{2i}^2}d\sigma \qquad (3.19)$$

where the values of T_{1i} are $T_{11} = T_{12} = -\frac{\partial f(\mu,\nu)}{\partial \nu}$ and $T_{13} = T_{14} = -\frac{\partial f(\mu,\nu)}{\partial \mu}$, the values of α_{1i} are $\alpha_{11} = \alpha_{12} = \mu - x$ and $\alpha_{13} = \alpha_{14} = \nu - y$, and the values of h_{1i} are $h_{11} = y$, $h_{12} = \nu - y$, $h_{13} = x$, and $h_{14} = \mu - x$. The values of T_{2i} are $T_{21} = T_{22} = f(\sigma, b)$ and $T_{23} = T_{24} = f(a, \sigma)$, the values of α_{2i} are $\alpha_{21} = \alpha_{22} = \sigma - x$ and $\alpha_{23} = \alpha_{24} = \sigma - y$, the values of h_{2i} are $h_{21} = y$, $h_{22} = b - y$, $h_{23} = x$, and $h_{24} = a - x$, and the values of (m_i, n_i) are $(m_1, n_1) = (m_2, n_2) = (a,\ 0)$ and $(m_3, n_3) = (m_4, n_4) = (b,\ 0)$ for $i = 1, 2, 3, 4$.

The apodized FNM expression in Eq. (3.19), which contains the summation of four double integrals and four single integrals, describes the pressure generated by an apodized piston for any boundary condition. The apodized FNM expression in Eq. (3.19) admits further simplification if the apodization function is equal to zero on the piston edge, where

$$f(0,\nu) = 0,\ f(a,\nu) = 0,\ f(\mu,0) = 0,\ \text{and}\ f(\mu,b) = 0. \qquad (3.20)$$

The boundary conditions given by Eq. (3.20) are equivalent to setting all of the terms T_{2i} equal to 0, so the single integrals with respect to σ in Eq. (3.19) disappear. The resulting apodized FNM expression is the summation of the four double integrals with respect to μ and ν, so only the first line of Eq. (3.19) is needed when the boundary values are all zero.

The FNM expression for the uniformly excited rectangular piston is also a special case of the apodized FNM expression in Eq. (3.19). For the uniform case, the

apodization function is $f(\mu,\nu) = \text{rect}(\mu/a)\text{rect}(\nu/b)$ where $\text{rect}(t) = 1$ if $t \in (0,\ 1)$ and $\text{rect}(t) = 0$ otherwise. The weak derivative of $f(\mu,\nu)$ is given by $\partial f(\mu,\nu)/\partial\mu = \delta(\mu) - \delta(\mu - a)$ and $\partial f(\mu,\nu)/\partial\nu = \delta(\nu) - \delta(\nu - b)$. When this apodization function is substituted into Eq. (3.19), all terms T_{2i} are equal to 0, and the double integrals reduce to a single integral, which is the same as $p_0[a,b](x,y,z;k)$ in Eq. (3.3).

3.2.2 Transient Apodized FNM Expression

The transient response for an apodized rectangular piston is obtained from the inverse Fourier transform [37] of Eq. (3.19). Defining $v(t)$ as the temporal component of the transient normal particle velocity $v(t)f(\mu,\nu)$, the transient pressure generated by an apodized rectangular piston is represented by

$$p_{apod}(x,y,z;\ t) = -\frac{\rho c}{2\pi}\sum_{i=1}^{4}\int_0^a\int_0^b T_{1i}h_{1i}\frac{v(t-\sqrt{\alpha_{1i}^2+z^2+h_{1i}^2}/c) - v(t-z/c)}{\alpha_{1i}^2+h_{1i}^2}d\mu d\nu$$

$$-\frac{\rho c}{2\pi}\sum_{i=1}^{4}\int_{n_i}^{m_i} T_{2i}h_{2i}\frac{v(t-\sqrt{\alpha_{2i}^2+z^2+h_{2i}^2}/c) - v(t-z/c)}{\alpha_{2i}^2+h_{2i}^2}d\sigma \qquad (3.21)$$

where the values of T_{1i}, α_{1i}, h_{1i}, T_{2i}, α_{2i}, and h_{2i} are listed immediately after Eq. (3.19) in the previous section. The expressions for the Rayleigh-Sommerfeld integral in Eqs. (3.1) and (3.2) are analytically equivalent to the apodized FNM expressions in Eqs. (3.19) and (3.21), but the numerical properties of the two methods differ as demonstrated in the results shown below.

3.2.3 Apodization function

The apodization function selected for comparisons between the apodized FNM, the Rayleigh-Sommerfeld integral, and the Field II program is the product of sinusoidal functions given by

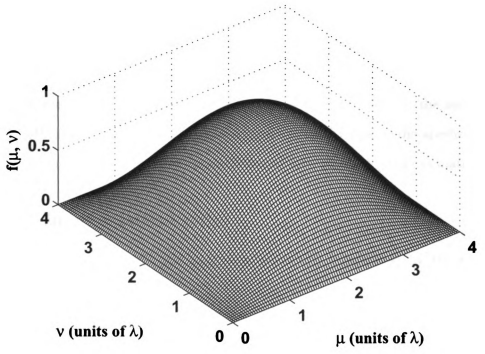

Figure 3.3. The apodization function $f(\mu, \nu) = \sin(\mu\pi/a)\sin(\nu\pi/b)$ evaluated on the face of a 4λ by 4λ square piston. The maximum value of the apodization function is achieved when $\mu = 2\lambda$ and $\nu = 2\lambda$.

$$f(\mu, \nu) = \sin(\mu\pi/a)\sin(\nu\pi/b). \tag{3.22}$$

This function corresponds to the lowest order vibration mode of a rectangular membrane with fixed edges [14, 38]. Eq. (3.22) is plotted for an apodized rectangular source with each side equal to 4 wavelengths in Figure 3.3.

The apodized FNM equations of Eq. (3.19) and Eq. (3.21) admit additional simplification when applied to the apodization function in Eq. (3.22). The apodization function is the product of two sinusoidal functions, so the apodization function is separable with respect to the variables μ and ν. After the derivative of the apodization function with respect to μ and ν is substituted into Eqs (3.19) and (3.21), the

first and third double integrals contain $\int_0^b \cos(\nu\pi/b)d\nu$ and $\int_0^a \cos(\mu\pi/a)d\mu$ terms, respectively. These two integrals are exactly equal to 0, so the first and third double integrals in Eq. (3.19) and Eq. (3.21) are equal to 0 for the apodization function in Eq. (3.22) at any observation point. Thus, only the second and fourth double integrals are needed. Furthermore, in Eq. (3.19) and Eq. (3.21), the second and the fourth double integrals share several terms. Shared terms in the apodized FNM equations are always computed once and stored for use in repeated calculations.

3.2.4 Input transient pulse

For transient calculations, the excitation pulse $v(t)$ is specified by the Hanning-weighted pulse

$$v(t) = \frac{1}{2}[1 - \cos(2\pi t/W)]\sin(2\pi f t)\text{rect}(t/W), \tag{3.23}$$

where $\text{rect}(t) = 1$ if $t \in (0,\ 1)$ and $\text{rect}(t) = 0$ otherwise. In the transient simulations that follow, the center frequency f_0 and the pulse duration W are $f_0 = 1.5$MHz and $W = 2.0\mu$s, respectively, for the Hanning-weighted pulse.

3.2.5 Time space decomposition

For transient calculations, most of the computation time is expended while evaluating $v(t-\tau)$ in Eq. (3.21) and $\dot{v}(t-\tau)$ in Eq. (3.2). These terms are calculated at each time t. The variable τ is a function of the observation coordinates only, so τ represents the contribution from the spatial variable. The function $v(t-\tau)$ can be separated according to the time space decomposition approach in Kelly and McGough [37]. This expression is decoupled as

$$v(t-\tau) = \text{rect}\left(\frac{t-\tau}{W}\right)\sum_{m=1}^{M} f_m(\tau)g_m(t), \tag{3.24}$$

where M=6 for transient FNM calculations with the Hanning-weighted pulse in Eq. (3.23), W is the length of the pulse, and the $f_m(\tau)$ and $g_m(t)$ terms are given in Table 3.1. The transient input to Eq. (3.2) is decoupled in the same manner, and the corresponding $f_m(\tau)$ and $g_m(t)$ terms for $\dot{v}(t-\tau)$ are given in Table 3.2 where $M = 10$ for transient Rayleigh-Sommerfeld calculations with the Hanning-weighted pulse. A simplified version of the time space decomposition algorithm is outlined below.

1. Pre-compute and store $g_m(t)$ in advance for all values of t.
2. Evaluate τ once for each spatial coordinate.
3. Compute the values of each $f_m(\tau)$ term immediately after τ is calculated.
4. Calculate the value of $v(t-\tau)$ according to Eq. (3.24).

By exploiting repeated calculations, this approach dramatically reduces the computation time without increasing the numerical error.

Table 3.1. Terms that define the time-space decomposition of the Hanning-weighted pulse $v(t-\tau)$ for transient apodized FNM calculations.

temporal basis functions $g_m(t)$	spatial basis functions $f_m(\tau)$
$g_1(t) = \frac{1}{2}\sin(2\pi f_0 t)$	$f_1(\tau) = \cos(2\pi f_0 \tau)$
$g_2(t) = -\frac{1}{2}\cos(2\pi f_0 t)$	$f_2(\tau) = \sin(2\pi f_0 \tau)$
$g_3(t) = -\frac{1}{2}\cos\left(\frac{2\pi t}{W}\right)\sin(2\pi f_0 t)$	$f_3(\tau) = \cos\left(\frac{2\pi \tau}{W}\right)\cos(2\pi f_0 \tau)$
$g_4(t) = \frac{1}{2}\cos\left(\frac{2\pi t}{W}\right)\cos(2\pi f_0 t)$	$f_4(\tau) = \cos\left(\frac{2\pi \tau}{W}\right)\sin(2\pi f_0 \tau)$
$g_5(t) = -\frac{1}{2}\sin\left(\frac{2\pi t}{W}\right)\sin(2\pi f_0 t)$	$f_5(\tau) = \sin\left(\frac{2\pi \tau}{W}\right)\cos(2\pi f_0 \tau)$
$g_6(t) = \frac{1}{2}\sin\left(\frac{2\pi t}{W}\right)\cos(2\pi f_0 t)$	$f_6(\tau) = \sin\left(\frac{2\pi \tau}{W}\right)\sin(2\pi f_0 \tau)$

3.2.6 Error Calculations

Two error metrics are used in this paper. One is the normalized error distribution $\eta(x, y, z; k)$, which describes the absolute value of the pressure difference at each spatial point for time-harmonic calculations. The other is the normalized root mean

Table 3.2. Terms that define the time-space decomposition of the derivative of a Hanning-weighted pulse $\dot{v}(t-\tau)$ for transient calculations with the apodized Rayleigh-Sommerfeld integral.

temporal basis functions $g_m(t)$	spatial basis functions $f_m(\tau)$
$g_1(t) = \pi f_0 \cos(2\pi f_0 t)$	$f_1(\tau) = \cos(2\pi f_0 \tau)$
$g_2(t) = \pi f_0 \sin(2\pi f_0 t)$	$f_2(\tau) = \sin(2\pi f_0 \tau)$
$g_3(t) = -\pi f_0 \cos\left(\frac{2\pi t}{W}\right) \cos(2\pi f_0 t)$	$f_3(\tau) = \cos\left(\frac{2\pi \tau}{W}\right) \cos(2\pi f_0 \tau)$
$g_4(t) = -\pi f_0 \cos\left(\frac{2\pi t}{W}\right) \sin(2\pi f_0 t)$	$f_4(\tau) = \cos\left(\frac{2\pi \tau}{W}\right) \sin(2\pi f_0 \tau)$
$g_5(t) = -\pi f_0 \sin\left(\frac{2\pi t}{W}\right) \cos(2\pi f_0 t)$	$f_5(\tau) = \sin\left(\frac{2\pi \tau}{W}\right) \cos(2\pi f_0 \tau)$
$g_6(t) = -\pi f_0 \sin\left(\frac{2\pi t}{W}\right) \sin(2\pi f_0 t)$	$f_6(\tau) = \sin\left(\frac{2\pi \tau}{W}\right) \sin(2\pi f_0 \tau)$
$g_7(t) = \frac{\pi}{W} \sin\left(\frac{2\pi t}{W}\right) \sin(2\pi f_0 t)$	$f_7(\tau) = \cos\left(\frac{2\pi \tau}{W}\right) \cos(2\pi f_0 \tau)$
$g_8(t) = -\frac{\pi}{W} \sin\left(\frac{2\pi t}{W}\right) \cos(2\pi f_0 t)$	$f_8(\tau) = \cos\left(\frac{2\pi \tau}{W}\right) \sin(2\pi f_0 \tau)$
$g_9(t) = -\frac{\pi}{W} \cos\left(\frac{2\pi t}{W}\right) \sin(2\pi f_0 t)$	$f_9(\tau) = \sin\left(\frac{2\pi \tau}{W}\right) \cos(2\pi f_0 \tau)$
$g_{10}(t) = \frac{\pi}{W} \cos\left(\frac{2\pi t}{W}\right) \cos(2\pi f_0 t)$	$f_{10}(\tau) = \sin\left(\frac{2\pi \tau}{W}\right) \sin(2\pi f_0 \tau)$

square error (NRMSE), which describes the overall error performance with a single value. For computed pressure field $p(x, y, z; k)$ and the reference pressure field $p_{ref}(x, y, z; k)$, the normalized error distribution $\eta(x, y, z; k)$ for each spatial point in time-harmonic calculations is given by

$$\eta(x, y, z; k) = |p(x, y, z; k) - p_{ref}(x, y, z; k)| / |p_{ref}(x, y, z; k)|_{\max(x,y,z)}. \quad (3.25)$$

The value of $\eta(x, y, z; k)$ is shown in each depiction of the error mesh. The normalized root mean square error (NRMSE) across all spatial points for time-harmonic calculations is

$$NRMSE = \sqrt{\sum_{x,y,z} |p(x, y, z; k) - p_{ref}(x, y, z; k)|^2} / \sqrt{\sum_{x,y,z} |p_{ref}(x, y, z; k)|^2}, \quad (3.26)$$

where $\sum_{x,y,z}$ denotes summation over all of the spatial grid points. The NRMSE for transient calculations is

$$NRMSE = \sqrt{\sum_{x,y,z,t} |p(x,y,z;\ t) - p_{ref}(x,y,z;\ t)|^2} / \sqrt{\sum_{x,y,z,t} |p_{ref}(x,y,z;\ t)|^2}, \tag{3.27}$$

where $\sum_{x,y,z,t}$ denotes summation over all spatial and temporal grid points. The values of the NRMSE are tabulated for each method evaluated in the results section 3.3. The reference fields $p_{ref}(x,y,z;k)$ and $p_{ref}(x,y,z;\ t)$ for time-harmonic calculations and transient calculations, respectively, are calculated using the Rayleigh-Sommerfeld integral.

For nearfield pressure calculations with the apodized FNM expressions and the Rayleigh-Sommerfeld integral, the number of abscissas in the μ and ν directions are the same for a square source. The NRMSE values for both methods are computed as the number of abscissas ranges from 2 to 100. The number of abscissas for a given NRMSE is determined by the smallest number of abscissas that has an NRMSE smaller than the desired NRMSE value. For nearfield pressure calculations with the Field II program, the sampling frequency f_S and the number of small rectangular elements are the two factors that determine the value of the NRMSE. In these calculations, the sampling frequency is varied from 16MHz to 160MHz with a step size of 16MHz, and the number of small rectangular elements in each direction ranges from 10 to 60 with a step size of 5. The NRMSE for each combination of the sampling frequency and the number of small rectangular elements is then computed. The sampling frequency and the number of small rectangular elements for a given NRMSE are determined by the combination that has the smallest computation time.

3.3 Results

3.3.1 Time-harmonic pressure calculations

Reference pressure field

The reference pressure field in Figure 3.4 is computed for the apodization function shown in Figure 3.3. In Figure 3.4, the acoustic field is evaluated in the $x = 2.0\lambda$ plane, where the grid in the $x = 2.0\lambda$ plane extends from -2λ to 6λ in the y direction, and the grid spacing in the y-direction is 0.1λ. The grid extends from $0.01a^2/4\lambda$ to $1.0a^2/4\lambda$ in the z direction with a spacing of $0.01a^2/4\lambda$. The computational grid in the z direction is shifted by $0.01a^2/4\lambda$ relative to the source in the $z = 0$ plane for all three methods in order to avoid the most severe singularities in this location. Although the apodized FNM eliminates the worst singularities in the $z = 0$ plane, the grid is nevertheless shifted slightly to reduce the problems that the Rayleigh integral and the Field II program encounter on the piston face. The reference pressure field shown in Figure 3.4 is obtained using the Rayleigh-Sommerfeld integral evaluated with 100,000 Gauss abscissas in each direction, and the results are computed on an 81×100 spatial grid.

Error distributions

Figures 3.5 and 3.6 shows the normalized error distribution $\eta(x, y, z; k)$ between the reference pressure field in Figure 3.4 and the simulated pressure field computed using the apodized FNM expression, the apodized Rayleigh-Sommerfeld integral, and the Field II program with the apodization function specified by Eq. 3.22. The region near the piston face contains the largest errors for all three methods. The NRMSE for the apodized FNM evaluated with $N = 16$ Gauss abscissas in each direction is 0.0005. The apodized Rayleigh-Sommerfeld integral evaluated with $N = 16$ Gauss abscissas in each direction has an NRMSE of 0.0450. The Field II program computed

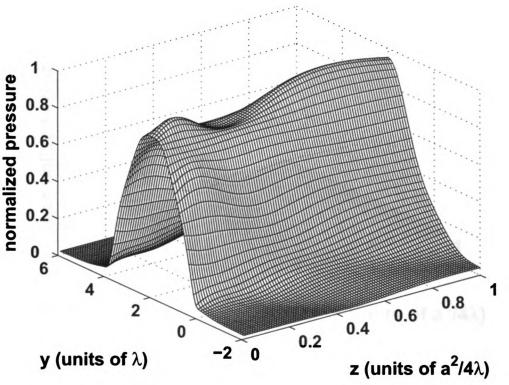

Figure 3.4. Simulated reference pressure field generated by an apodized rectangular source with each side equal to 4 wavelengths. The results are evaluated in the $x = 2.0\lambda$ plane for a time-harmonic excitation.

with a 48MHz sampling frequency and 30 subdivisions in each direction achieves an NRMSE of 0.0808.

Time vs. error comparisons for a time-harmonic input

Figure 3.7 shows the computation times and the error values for nearfield pressure calculations with a time-harmonic input applied to the apodized FNM, the Rayleigh-Sommerfeld integral, and the Field II program. In Figure 3.7, the apodized FNM achieves the smallest errors for a given computation time, and the apodized FNM uses the least amount of time for a given error value. Comparisons between the apodized

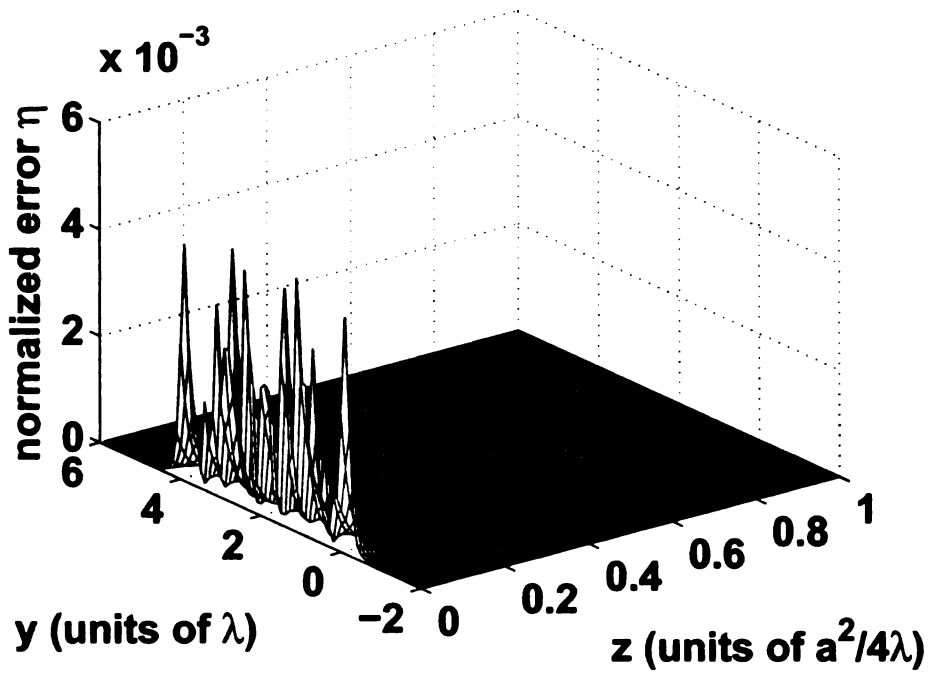

a) Apodized FNM.

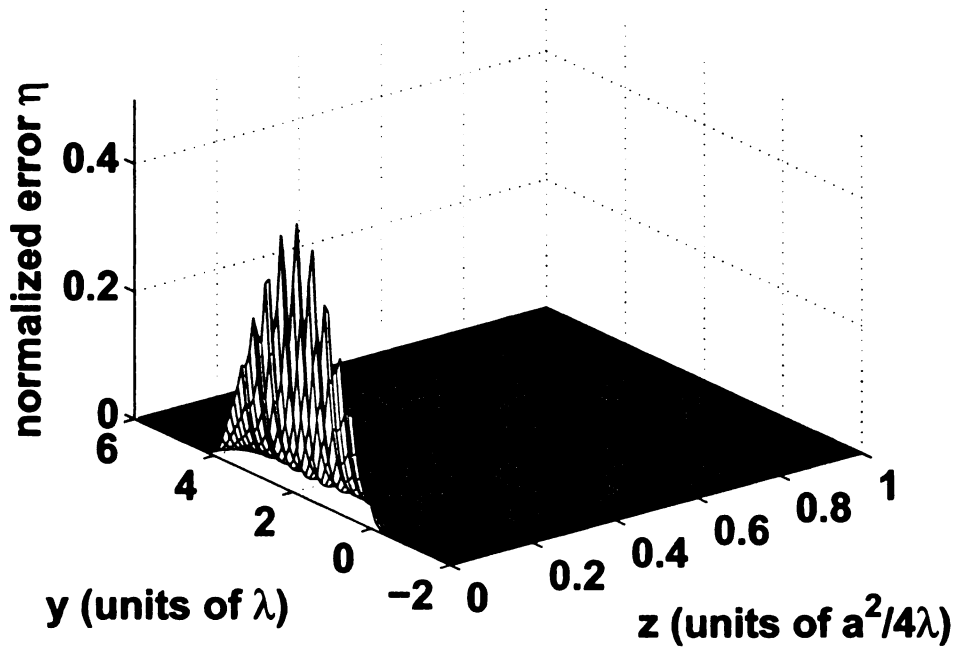

b) Rayleigh integral.

Figure 3.5. The normalized error distribution $\eta(x, y, z; k)$ describes the difference between the reference pressure field and the computed pressure field for an apodized 4λ by 4λ source. The error distribution η is plotted for a) the apodized FNM evaluated with 16-point Gauss quadrature in each direction, b) the apodized Rayleigh integral evaluated with 16-point Gauss quadrature in each direction.

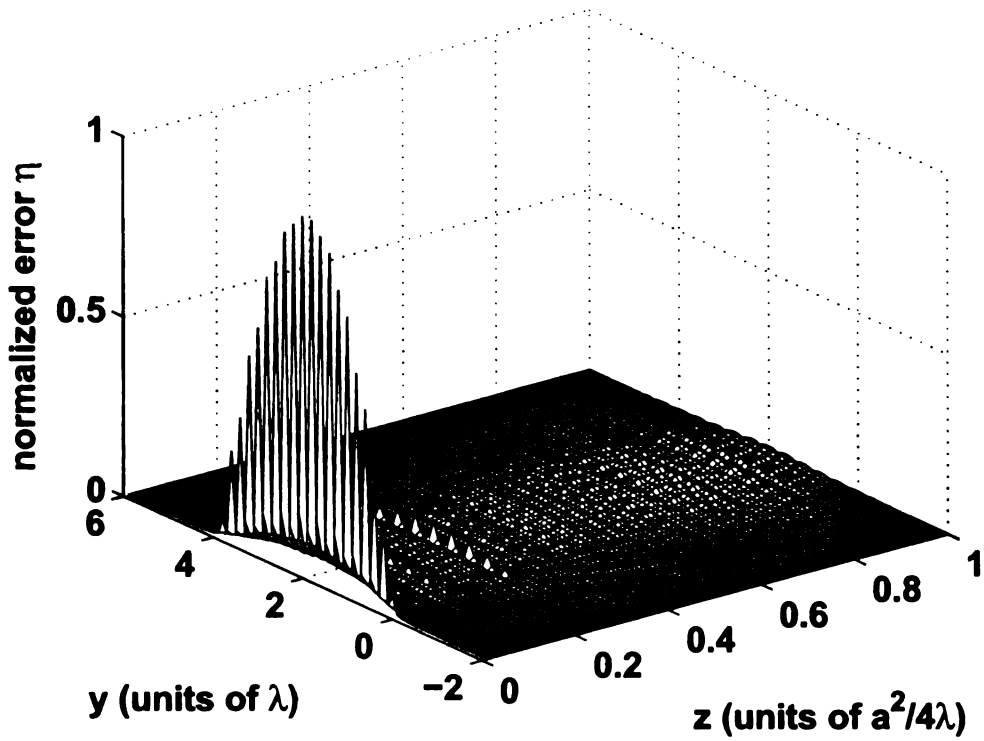

Figure 3.6. The normalized error distribution $\eta(x, y, z; k)$ describes the difference between the reference pressure field and the computed pressure field for an apodized 4λ by 4λ source. The error distribution η is plotted for the Field II program evaluated with $f_S = 48$MHz and 30 subdivisions in each direction.

FNM, the Rayleigh integral, and the Field II program are summarized in Table 3.3. To achieve an NRMSE of 0.1, the apodized FNM needs 6 abscissas in each direction, and the computation time is 0.07 seconds. The apodized FNM achieves an NRMSE of 0.01 in 0.18 seconds with 10 abscissas in each direction. Likewise, to achieve an NRMSE of 0.1, the Rayleigh-Sommerfeld integral needs 12 abscissas in each direction, and the computation time is 0.29 seconds. The Rayleigh-Sommerfeld integral achieves an NRMSE of 0.01 in 2.25 seconds with 34 abscissas in each direction. Instead of evaluating an integral with a certain number of abscissas, the Field II program subdivides the aperture into small rectangular sources and calculates the impulse

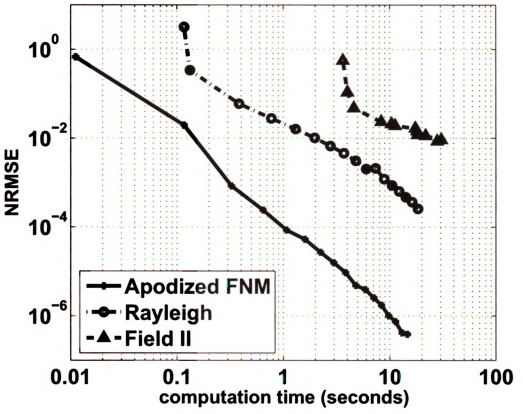

Figure 3.7. Normalized root mean square error (NRMSE) plotted as a function of the computation time for time-harmonic calculations with the apodized FNM, the apodized Rayleigh-Sommerfeld integral, and the Field II program. This figure demonstrates that the apodized FNM achieves the smallest errors for a given computation time, and the apodized FNM requires the smallest amount of time to achieve a given error value.

response at a specified sampling frequency. To achieve an NRMSE of 0.1, the Field II program requires a temporal sampling frequency of 64MHz and 20 subdivisions in each direction, and the result is obtained in 4.61 seconds. The Field II program achieves an NRMSE of 0.01 with a temporal sampling frequency of 160MHz and 50 subdivisions in each direction. This calculation is completed in 27.91 seconds. Thus, for an NRMSE of 0.1, the apodized FNM is 4.14 times faster than the Rayleigh integral, and the apodized FNM is 59.43 times faster than the Field II program. For an NRMSE of 0.01, the apodized FNM is 12.50 times faster than the Rayleigh integral, and the apodized FNM is 155.06 times faster than the Field II program. These results are specific to the grid and piston geometry in Figure 3.3 and the apodization function in Eq. (3.22). Although the results vary somewhat for different parameter combinations, the apodized FNM consistently achieves the best performance in time vs. error comparisons. The apodized FNM is also an ideal reference for time-harmonic calculations due to the rapid convergence of Eq. (3.19).

3.3.2 Transient field calculations

Reference pressure field

The reference transient field is computed using the transient Rayleigh-Sommerfeld integral in Eq. (3.2), where the numerical integration is performed with 100,000 Gauss abscissas applied in both the height and width directions. The input pulse is the Hanning-weighted pulse in Eq. (3.23) with center frequency $f_0 = 1.5$MHz and pulse length $W = 2.0\mu$s. The speed of sound is $c = 1.5\text{mm}/\mu\text{s}$, and the wavelength at the center frequency is $\lambda = 1.0$mm. The sampling frequency is 16MHz. The transient field is evaluated in the $x = 2.0\lambda$ plane, where the computational grid extends from -2λ to 6λ in the y direction and from $0.01a^2/4\lambda$ to $1.0a^2/4\lambda$ in the z direction as shown in Figure 3.1. The reference transient field is calculated on an 81×100 spatial grid evaluated at 192 time points. Figure 3.8 shows two transient plots of the reference

Table 3.3. Simulation parameters for time-harmonic calculations that achieve normalized root mean square error (NRMSE) values of 0.1 and 0.01. Parameters listed include the number of Gauss abscissas or the corresponding Field II parameters, the resulting computation time, and computation time relative to the apodized FNM for the Rayleigh integral and the Field II program. (a) For a 0.1 NRMSE and (b) for a 0.01 NRMSE.

(a)

	Time-Harmonic Calculations		
	0.1 NRMSE		
	Apodized FNM	Rayleigh	Field II
Simulation Parameters	6×6 abscissas	12×12 abscissas	f_S = 64MHz 20×20 subdivisions
Time	0.07s	0.29s	4.61s
Computation Time Relative to Apodized FNM	1×	4.14×	59.43×

(b)

	Time-Harmonic Calculations		
	0.01 NRMSE		
	Apodized FNM	Rayleigh	Field II
Simulation Parameters	10×10 abscissas	34×34 abscissas	f_S = 160MHz 50×50 subdivisions
Time	0.18s	2.25s	27.91s
Computation Time Relative to Apodized FNM	1×	12.50×	155.06×

pressure evaluated at times $t = 1.5625\mu$s and $t = 3.0625\mu$s.

Time vs. error comparisons for a Hanning-weighted input pulse

Figure 3.9 shows the computation times and the numerical errors for the transient pressure field generated by the Hanning-weighted input pulse evaluated with the transient apodized FNM, the transient Rayleigh-Sommerfeld integral, and the Field II program. For both the transient apodized FNM and the transient Rayleigh-Sommerfeld integral, the simplified time space decomposition approach is applied as described in Section 3.2.5. In Figure 3.9, the transient apodized FNM achieves the smallest errors for a given computation time, and the transient apodized FNM requires the smallest amount of time to achieve a given error. Comparisons between the transient apodized FNM, the transient Rayleigh integral, and the Field II program are summarized in Table 3.4. To achieve an NRMSE of 0.1 with the Hanning weighted pulse, the transient apodized FNM needs 8 abscissas in each direction, and the computation time is 0.64 seconds. The transient apodized FNM achieves an NRMSE of 0.01 in 0.72 seconds with 10 abscissas applied in each direction. To achieve an NRMSE of 0.1 with the Hanning weighted pulse, the transient Rayleigh-Sommerfeld integral needs 14 abscissas in each direction, and the computation time is 1.48 seconds. The transient Rayleigh-Sommerfeld integral achieves an NRMSE of 0.01 in 8.57 seconds with 34 abscissas in each direction. To achieve an NRMSE of 0.1 with the Hanning weighted pulse, the Field II program requires a temporal sampling frequency of 64MHz and 20 subdivisions in each source direction, and the result is obtained in 4.68 seconds. The Field II program achieves an NRMSE of 0.01 with a temporal sampling frequency of 128MHz and 50 subdivisions of the source in each direction. This calculation is completed in 24.04 seconds. Thus, for an NRMSE of 0.1, the transient apodized FNM is 2.31 times faster than the transient Rayleigh integral, and the transient apodized FNM is 4.66 times faster than the Field II program. For an NRMSE of 0.01, the

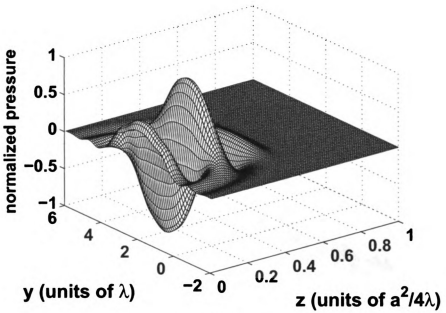

a) $t = 1.5625\mu s$.

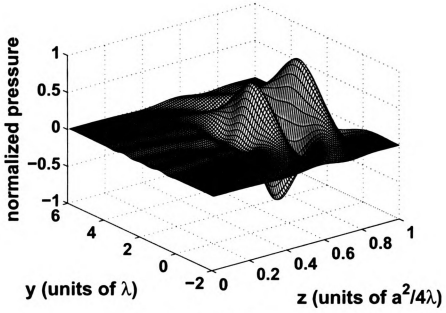

b) $t = 3.0625\mu s$.

Figure 3.8. Simulated reference transient field for an apodized square source excited by the Hanning-weighted pulse in Eq. (3.23) with $f_0 = 1.5$ MHz and $W = 2.0\lambda$. The sides of the square source are equal to 4λ. The apodization function is given by Eq. (3.22). The transient reference pressure, evaluated in the $x = 2.0\lambda$ plane, is computed with 100,000 Gauss abscissas in each direction using the Rayleigh integral. Results are plotted at a) $t = 1.5625\mu$s and b) $t = 3.0625\mu$s.

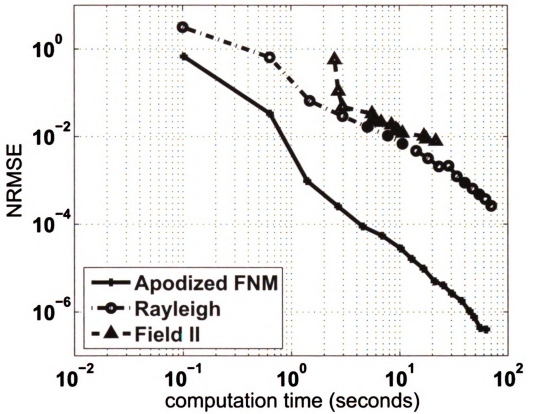

Figure 3.9. Normalized root mean square error (NRMSE) plotted as a function of the computation time for transient pressure calculations evaluated with the apodized FNM, the apodized Rayleigh-Sommerfeld integral, and the Field II program. For the same computation time, the apodized FNM achieves the smallest errors, and for the same error, the apodized FNM requires the least amount of time.

transient apodized FNM is 11.90 times faster than the transient Rayleigh integral, and the transient apodized FNM is 24.04 times faster than the Field II program. Once again, these results are specific to the grid, apodization function, and piston geometry utilized in this paper. Overall, the transient apodized FNM achieves the best performance in time vs. error comparisons with the Hanning-weighted pulse.

3.4 Discussion

3.4.1 Large-scale computation

Despite the dramatic increase in processor speeds and computer memory in recent decades, nearfield pressure calculations that numerically evaluate the Rayleigh-Sommerfeld integral are still very slow. This is especially evident in calculations performed on large grids, which take an hour or more on the fastest modern desktop computers. For example, more than one hour was needed in a recent paper to compute the reference pressure field in the Fresnel zone for a single element using the Rayleigh-Sommerfeld approach [14]. More recently, nearfield pressure calculations with the Rayleigh-Sommerfeld approach for a single element required 117 hours [39] per simulation to achieve a NRMSE of 10^{-7}. Thus, even for simulations of single elements performed in the nearfield region, traditional computational methods perform poorly, and faster methods such as the FNM are needed.

Computation times with the Rayleigh-Sommerfeld integral can also be excessively long for phased array simulations. Extending the results shown in Tables 3.3 and 3.4 and Figures 3.7 and 3.9 to a linear phased array with 1024 rectangular elements evaluated on a computational grid with $100 \times 100 \times 100$ points in the x, y, and z directions, the Rayleigh-Sommerfeld integral will require about 10 hours for a 0.1 NRMSE and about 80 hours for a 0.01 NRMSE. For the same array evaluated on the same grid, the FNM will require only 2.5 hours for a 0.1 NRMSE and 6.5 hours for

Table 3.4. Simulation parameters for transient calculations that achieve normalized root mean square error (NRMSE) values of 0.1 and 0.01. Parameters listed include the number of Gauss abscissas or the corresponding Field II parameters, the resulting computation time, and the computation time relative to the apodized FNM for the Rayleigh integral and the Field II program. (a) For a 0.1 NRMSE and (b) for a 0.01 NRMSE.

(a)

	Transient Calculations		
	0.1 NRMSE		
	Apodized FNM	Rayleigh	Field II
Simulation Parameters	8×8 abscissas	14×14 abscissas	f_S = 64MHz 20×20 subdivisions
Time	0.64s	1.48s	2.98s
Computation Time Relative to the Apodized FNM	1×	2.31×	4.66×

(b)

	Transient Calculations		
	0.01 NRMSE		
	Apodized FNM	Rayleigh	Field II
Simulation Parameters	10×10 abscissas	34×34 abscissas	f_S = 128MHz 50×50 subdivisions
Time	0.72s	8.57s	17.26s
Computation Time Relative to the Apodized FNM	1×	11.90×	24.04×

a 0.01 NRMSE. Thus, for large-scale computations, the time savings achieved by the apodized FNM is substantial. The apodized FNM is also an ideal reference for both time-harmonic and transient calculations.

3.4.2 Time and error comparisons

In addition to the results presented shown in Tables 3.3 and 3.4 and Figures 3.7 and 3.9 that compare the Rayleigh-Sommerfeld integral and the apodized FNM, the individual computation times and error values were also determined as a function of the number of abscissas. Those results show that, for a given number of abscissas, the apodized FNM achieves much smaller errors than the Rayleigh-Sommerfeld integral, and the computation time of the apodized FNM is slightly less than that of the Rayleigh integral for the same number of abscissas. Therefore, the rapid convergence of the apodized FNM is responsible for the enhancement in performance relative to other methods. However, fair comparisons of these methods require the evaluation of both times and errors as shown in Tables 3.3 and 3.4 and Figures 3.7 and 3.9. Otherwise, a method that generates large errors in a similar amount of time or a method that requires much more time to achieve a similar error could be incorrectly identified as having comparable performance. The method with superior performance should consistently achieve the smallest error in the shortest time.

3.4.3 Apodization functions

Eq. (4.24) and Eq. (3.21) can be applied to a large class of apodization functions. The only requirement for the apodization functions is that $\partial f(\mu,\nu)/\partial\mu$ and $\partial f(\mu,\nu)/\partial\nu$ exist. Other approaches have different requirements. For example, Fresnel approximations have been obtained for several apodization functions including exponential, sinusoidal, Gaussian, or error-function apodization functions [14]. One restriction for these Fresnel approximations is that the surface velocity distribution should be

separable such that $f(\mu,\nu) = f_x(\mu)f_y(\nu)$. The advantages of the apodized FNM expressions in Eq. (4.24) and Eq. (3.21) are that: 1. separability of the apodization function is not required, and 2. accurate results are obtained very close to the piston face.

Pressures generated by a Gaussian apodization function [40, 41, 42], given by $f(\mu,\nu) = e^{-(u-u_0)^2/2\sigma_\mu^2} e^{-(\nu-\nu_0)^2/2\sigma_\nu^2}$ where μ_0, ν_0, σ_μ, and σ_ν are constants, were also evaluated with Eq. (4.24). When the Gaussian apodization function is applied, the entire expressions in Eqs. (4.24) and (3.21) are needed because the T_{2i} terms are nonzero in this case. Furthermore, the integration limits of the single integrals are either (0, a) or (0, b), so the abscissas and weights computed for the single integrals can also be used for the double integrals. The computation time needed for all terms in Eqs. (4.24) and (3.21) is only slightly more than that needed to evaluate only the double integrals, especially when the number of abscissas is larger than 10 in one direction.

3.4.4 Time Space Decomposition

The expressions for the transient nearfield pressures are computed with the simplified time space decomposition approach outlined in section 3.2.5 for both the transient apodized FNM expression and the transient Rayleigh-Sommerfeld integral in Eq. (3.21) and Eq. (3.2), respectively. The simplified time space decomposition approach provides an important advantage in that, unlike the original time space decomposition method described by Kelly and McGough [36], one dimensional and two dimensional nearfield diffraction integrals are readily computed. The original time space decomposition method of Kelly and McGough [36] stores a 3D K matrix that captures the arrival and departure information for a finite duration pulse, where the transient pressure propagation is described by a single integral FNM expression. Extending the original time space decomposition to handle transient calculations with

the 2D apodized FNM expressions in Eq. (3.21) or the Rayleigh-Sommerfeld integral in Eq. (3.2) involves replacing the three dimensional K matrix with a complicated five dimensional K matrix. With the simplified time space decomposition approach, no matrix storage is needed. Thus, the algorithm complexity and the memory usage are greatly reduced. The simplified time space decomposition in section 3.2.5 is preferred for transient calculations with 2D integrals, where a significant reduction in the computation time is achieved relative to other approaches without increasing the numerical error. For transient calculations with 1D integrals, there is a trade-off between the simplified time space decomposition and the original time space decomposition method. The original time space decomposition requires more memory, is more complicated to program, and is slightly faster, while the simplified time space decomposition is much easier to program.

CHAPTER 4

A 1D Fast Nearfield Method for Rectangular Pistons with Polynomial Apodization

Pressure fields generated from apodized rectangular sources are readily calculated using the Rayleigh-Sommerfeld integral [6] and the analytically equivalent 2D apodized FNM expression [43]. Both of these methods evaluate double integrals, which handle various types of apodization functions. However, the numerical performance of those methods are quite different. Numerical calculations of the Rayleigh-Sommerfeld integral converge very slowly in the nearfield region due to a $1/R$ singularity. The performance of the 2D apodized FNM is much better than the Rayleigh-Sommerfeld integral in the nearfield since the singularities have been eliminated. Thus, the 2D apodized FNM is a better choice if a general 2D apodization function is given. However, the computation time can be reduced further if the 2D FNM integral can be converted into a 1D FNM integral. This is achieved with polynomial apodization functions.

To improve the numerical performance of nearfield calculations with polynomial

apodized rectangular pistons, a 1D polynomial apodized FNM expression is derived from the instantaneous impulse response proposed by Scarano et al [44]. The derivation of the apodized FNM for rectangular pistons starts by convolving the instantaneous impulse response with the polynomial apodized particle velocity. Then, after obtaining a double integral and specifying the particular polynomial apodization functions, the inner integral can be integrated analytically, and the polynomial apodized FNM is obtained. Two polynomial apodization functions are considered, where one is a 1D quadratic polynomial and the other is the product of two 1D quadratic polynomials. The results show that the convergence of the polynomial apodized FNM is much better than the 2D apodized FNM and the Rayleigh-Sommerfeld integral for both of these apodization functions.

4.1 Polynomial apodization derivation

4.1.1 Instantaneous Impulse Response

The instantaneous impulse response [44] is obtained at a fixed time t on a specific plane where the value of z is a constant. The spatial particle velocity distribution $s(x, y)$ on the piston face is given by

$$s(x, y) = u(x)\text{rect}(x/a)w(y)\text{rect}(y/b) \tag{4.1}$$

where $u(x)$ and $w(y)$ are the normal particle velocity distributions on the vibrating surface along the x and y directions, $\text{rect}(x) = 1$ for $|x| \leq 1$ and $\text{rect}(x) = 0$ for $|x| > 1$ and a and b are the width and height of the rectangular piston in the x and y directions, respectively. The separable particle velocity distribution can also be expressed by means of two-dimensional convolution as

$$s(x, y) = (u(x)\text{rect}(x/a)\delta(y)) * *(w(y)\text{rect}(y/b)\delta(x)) \tag{4.2}$$

The impulse response $h(z;t)$ is given by

$$h(z;t) = \frac{c}{2\pi} u(x)\text{rect}(x/a)\delta(y) ** \left[w(y)\text{rect}(y/b)\delta(x) ** \frac{\delta(r-r_0)}{r_0} \right]$$

$$= \frac{c}{2\pi} u(x)\text{rect}(x/a)\delta(y) ** f(x,y) \tag{4.3}$$

where $r = \sqrt{x^2+y^2}$, and $r_0 = \sqrt{c^2t^2 - z^2}$. The instantaneous impulse response for $y > b$ is given by [44]

$$h(z;t) = \begin{cases} 0 & r_0 < y-b \\ \frac{c}{2\pi}\theta(\xi_1,\xi_2)\text{rect}(\frac{x}{a+x_1}) & y-b \le r_0 \le y+b \\ \frac{c}{2\pi}\left[\theta(\xi_1,\xi_2)\text{rect}(\frac{x}{a+x_1}) \right. & \\ \left. -\theta(\xi_3,\xi_4)\text{rect}(\frac{x}{a+x_2})\right] & r_0 \ge y+b \end{cases}, \tag{4.4}$$

where $\theta(\xi_1,\xi_2) = \int_{\xi_1}^{\xi_2} u(x-\xi)\frac{w(\sqrt{r_0^2-x^2}-y)}{(r_0^2-\xi^2)^{1/2}}d\xi$, $x_1 = \sqrt{r_0^2-(y-b)^2}$,
$x_2 = \sqrt{r_0^2-(y+b)^2}$, $\xi_1 = \max(x-a,-x_1)$, $\xi_3 = \max(x-a,-x_2)$,
$\xi_2 = \min(x+a,x_1)$, $\xi_4 = \min(x+a,x_2)$.

The apodized pressure based on these expressions is readily extended to all values of y.

4.1.2 Time-harmonic pressure calculations

The time-harmonic pressure generated by a polynomial apodized rectangular piston is given by

$$P(x,y,z;k) = j\omega\rho e^{j\omega t} \int_{-\infty}^{+\infty} e^{-j\omega\tau} h(z;\tau)d\tau \tag{4.5}$$

where ω is the excitation frequency in radians per second, ρ is the density of the medium, $h(z;t)$ is the instantaneous impulse response in Eq. (4.4) which accounts for the apodization, k is the wavenumber, and t is the elapsed time. Distance parameters are defined as $d_1 = \sqrt{(x-a)^2+(y-b)^2+z^2}$, $d_2 = \sqrt{(x-a)^2+(y+b)^2+z^2}$, $d_3 = \sqrt{(x+a)^2+(y-b)^2+z^2}$, and $d_4 = \sqrt{(x+a)^2+(y+b)^2+z^2}$, and then $h(z;t)$ in Eq. (4.4) is substituted into the pressure calculation expression in Eq. (4.5). For $x \geq a$, the expression for the nearfield pressure is obtained,

$$P(x,y,z;k) = \frac{c}{2\pi}\sum_{i=1}^{3} q_{1i}\int_{m_{1i}}^{n_{1i}} e^{-jk\beta}\int_{m_{2i}}^{n_{2i}} f(\xi,\beta)d\xi d\beta, \tag{4.6}$$

where the values of q_i are $q_{11} = q_{12} = 1$ and $q_{13} = -1$, the values of (m_{1i}, n_{1i}) are $(m_{11}, n_{11}) = (d_3, d_4)$, $(m_{12}, n_{12}) = (d_1, d_3)$, and $(m_{13}, n_{13}) = (d_2, d_4)$, the values of (m_{2i}, n_{2i}) are $(m_{21}, n_{21}) = (x-a, x+a)$, $(m_{22}, n_{22}) = (x-a, x_1)$, and $(m_{23}, n_{23}) = (x-a, x_2)$, and $f(\xi,\beta) = u(x-\xi)w(\sqrt{r_0^2 - x^2} - y)/\sqrt{\beta^2 - z^2 - \xi^2}$.

The inner integrals $\int_{m_{2i}}^{n_{2i}} f(\xi,\beta)d\xi$ in Eq. (4.6) can be represented as the sum of two integrals,

$$\int_{m_{2i}}^{n_{2i}} f(\xi,\beta)d\xi = \int_{0}^{n_{2i}} f(\xi,\beta)d\xi + \int_{m_{2i}}^{0} f(\xi,\beta)d\xi. \tag{4.7}$$

Using Eq. (4.7), the pressure expression for $x \geq a$ and $y \geq b$ in Eq. (4.6) forms six double integrals which are given by

$$P(x,y,z;k) = \frac{c}{2\pi}\sum_{i=1}^{3} q_{1i}\int_{m_{1i}}^{n_{1i}} e^{-jk\beta}\int_{0}^{n_{2i}} f(\xi,\beta)d\xi d\beta$$

$$+\frac{c}{2\pi}\sum_{i=1}^{3} q_{1i}\int_{m_{1i}}^{n_{1i}} e^{-jk\beta}\int_{m_{2i}}^{0} f(\xi,\beta)d\xi d\beta \tag{4.8}$$

And by combining the limits in the outer integral, Eq. (4.6) can be simplified as

$$P(x,y,z;k) = \frac{c}{2\pi}\sum_{i=1}^{4} q_{2i}\int_{m_{3i}}^{n_{3i}} e^{-jk\beta}\int_{0}^{n_{4i}} f(\xi,\beta)d\xi d\beta, \tag{4.9}$$

where the values of q_i are $q_{21} = q_{24} = -1$ and $q_{22} = q_{23} = 1$, the values of (m_{3i}, n_{3i}) are $(m_{31}, n_{31}) = (d_1, d_2)$, $(m_{32}, n_{32}) = (d_3, d_4)$, $(m_{33}, n_{33}) = (d_1, d_3)$ and $(m_{34}, n_{34}) = (d_2, d_4)$, and the values of n_{4i} are $n_{41} = x - a$, $n_{42} = x + a$, $n_{43} = x_1$, and $n_{44} = x_2$, and $f(\xi, \beta) = u(x - \xi)w(\sqrt{r_0^2 - x^2} - y)/\sqrt{\beta^2 - z^2 - \xi^2}$.

4.1.3 1D quadratic apodization

In the derivation of the FNM expressions for 1D quadratic apodization, the apodization function $u(x)$ is a quadratic function with $u(x) = p + qx + rx^2$, where p, q, and r are constant coefficients and $w(y) = 1$. Then, $u(x - \xi)$ is written as $u(x - \xi) = A + B\xi + C\xi^2$, where $A = p + qx + rx^2$, $B = -(q + 2rx)$, and $C = r$ and $w(\sqrt{r_0^2 - x^2} - y)$=1. The inner integral in Eq. (4.9) is computed as

$$\int_0^{\xi_2} u(x - \xi) \frac{d\xi}{\sqrt{r_0^2 - \xi^2}} = I_{term1} + I_{term2} + I_{term3}, \tag{4.10}$$

where $I_{term1} = (A + \frac{1}{2}Cr_0^2) \tan^{-1}\left(\xi_2/\sqrt{r_0^2 - \xi_2^2}\right)$, $I_{term2} = -\left(B + \frac{1}{2}C\xi_2\right)\sqrt{r_0^2 - \xi_2^2}$, $I_{term3} = B\sqrt{\beta^2 - z^2}$, and $r_0 = \sqrt{\beta^2 - z^2}$.

The first term

After substituting the first term from Eq. (4.10) into Eq. (4.9), the $\tan^{-1}(\cdot)$ term is converted into an equivalent integral expression using the identity $\tan^{-1}(x) + \tan^{-1}(1/x) = \pi/2$. The $\tan^{-1}(\cdot)$ term then becomes

$$\tan^{-1}\left(\frac{x - a}{\sqrt{\beta^2 - z^2 - (x - a)^2}}\right) =$$

$$\frac{\pi}{2} - \int_0^{\sqrt{\beta^2 - z^2 - (x-a)^2}} \frac{x - a}{(x - a)^2 + \sigma^2} d\sigma. \tag{4.11}$$

By substituting Eq. (4.11) into Eq. (4.9) and exchanging the order of integration, the pressure calculation result for I_{term1} in Eq. (4.10) becomes

$$P_{term1}(x,y,z;k) = \frac{c}{2\pi}\left(\sum_{i=1}^{4} q_{3i}\int_{m_i}^{n_i}\int_{\sigma_i}^{0} g(\beta)d\beta\frac{h_i}{h_i^2+\sigma^2}d\sigma\right), \tag{4.12}$$

where the values of the q_i are $q_{31} = q_{33} = 1$ and $q_{32} = q_{34} = -1$, the values of σ_i are $\sigma_1 = \sqrt{\sigma^2+(x-a)^2+z^2}$, $\sigma_2 = \sqrt{\sigma^2+(x+a)^2+z^2}$, $\sigma_3 = \sqrt{\sigma^2+(y-b)^2+z^2}$, and $\sigma_4 = \sqrt{\sigma^2+(y+b)^2+z^2}$, the values of (m_i,n_i) are $(m_1,n_1) = (m_2,n_2) = (y-b,y+b)$ and $(m_3,n_3) = (m_4,n_4) = (x-a,x+a)$, and the values of h_i are $h_1 = x-a$, $h_2 = x+a$, $h_3 = y-b$, and $h_4 = y+b$.

The four integrals in Eq. (4.12) are double integrals, but the inner integral with respect to β can be evaluated analytically. The resulting 1D integral for Eq. (4.12) is given by

$$P_{term1}(x,y,z;k) = \frac{c}{2\pi}\sum_{i=1}^{4} q_{3i}\int_{m_i}^{n_i}\left[\frac{j(Ak^2-C)h_i}{k^3(h_i^2+\sigma^2)}\left(e^{-jk\sigma_i}-e^{-jkz}\right)\right.$$

$$\left.+\frac{Cj}{2k}h_i e^{-jk\sigma_i}+\frac{C}{k^2}\frac{h_i}{h_i^2+\sigma^2}\left(\sigma_i e^{-jk\sigma_i}-ze^{-jkz}\right)\right]d\sigma. \tag{4.13}$$

The second term

Substituting I_{term2} into each double integral in Eq. (4.9) and performing the change the variable $\sigma = \sqrt{\beta^2-z^2-\xi_2^2}$ produces the analytical expression given by

$$P_{term2}(x,y,z;k) = -\frac{c}{2\pi}B\left[\sum_{i=1}^{2} q_{2i}\int_{m_i}^{n_i}\left(\frac{e^{-jk\sigma_i}\sigma^2}{\sigma_i}\right)d\sigma\right.$$

$$\left.+\frac{y-b}{-jk}\left(e^{-jkd_3}-e^{-jkd_1}\right)-\frac{y+b}{-jk}\left(e^{-jkd_4}-e^{-jkd_2}\right)\right]$$

$$-\frac{cC}{4\pi}\sum_{i=1}^{4} q_{2i}h_i \int_{m_i}^{n_i}\left(\frac{e^{-jk\sigma_i\sigma^2}}{\sigma_i}\right)d\sigma, \tag{4.14}$$

where the values of the q_{2i} are $q_{21} = q_{24} = -1$ and $q_{22} = q_{23} = 1$.

The third term

After substituting I_{term3} into Eq. (4.9), the integrands of all four double integrals are the same. The first and fourth double integrals can be combined to form a new double integral with the integration limits from $\sqrt{(x-a)^2+(y-b)^2+z^2}$ to $\sqrt{(x+a)^2+(y+b)^2+z^2}$ with the integrand $-e^{-jk\beta}B\sqrt{\beta^2-z^2}$, and the second and third double integrals are combined into a double integral with the integration limits from $\sqrt{(x-a)^2+(y-b)^2+z^2}$ to $\sqrt{(x+a)^2+(y+b)^2+z^2}$ for the integrand $e^{-jk\beta}B\sqrt{\beta^2-z^2}$, thus

$$P_{term3}(x,y,z;k) = 0. \tag{4.15}$$

The final equation for the 1D quadratic apodization

The total pressure in Eq. (4.9) is the sum of three terms given by Eq. (4.13), Eq. (4.14) and Eq. (4.15), where $P(x,y,z;k) = P_{term1}(x,y,z;k) + P_{term2}(x,y,z;k) + P_{term3}(x,y,z;k)$, which is

$$P(x,y,z;k) = \frac{c}{2\pi}\sum_{i=1}^{4} q_{3i}\int_{m_i}^{n_i}\left[\frac{j(Ak^2-C)h_i}{k^3(h_i^2+\sigma^2)}\left(e^{-jk\sigma_i}-e^{-jkz}\right)\right.$$

$$\left.+\frac{Cj}{2k}h_i e^{-jk\sigma_i}+\frac{C}{k^2}\frac{h_i}{h_i^2+\sigma^2}\left(\sigma_i e^{-jk\sigma_i}-ze^{-jkz}\right)\right]d\sigma$$

$$-\frac{c}{2\pi}B\left[\sum_{i=1}^{2} q_{2i}\int_{m_i}^{n_i}\left(\frac{e^{-jk\sigma_i\sigma^2}}{\sigma_i}\right)d\sigma\right.$$

$$+\frac{y-b}{-jk}\left(e^{-jkd_3}-e^{-jkd_1}\right)-\frac{y+b}{-jk}\left(e^{-jkd_4}-e^{-jkd_2}\right)\Bigg]$$

$$-\frac{cC}{4\pi}\sum_{i=1}^{4}q_{2i}h_i\int_{m_i}^{n_i}\left(\frac{e^{-jk\sigma_i\sigma^2}}{\sigma_i}\right)d\sigma. \tag{4.16}$$

4.1.4 2D Quadratic apodization

In the derivation of the FNM expression for 2D quadratic apodization, the apodization functions $u(x)$, $w(y)$ are quadratic functions with $u(x) = p_1 + q_1x + r_1x^2$ and $w(y) = p_2 + q_2y + r_2y^2$, where p_1, q_1, r_1, p_2, q_2, and r_2 are constant coefficients. The resulting expressions for $u(x-\xi)$ and $w(\sqrt{r_0^2-\xi^2}-y)$ are

$$u(x-\xi) = A_1 + B_1\xi + C_1\xi^2$$
$$w(\sqrt{r_0^2-\xi^2}-y) = A_2 + B_2\sqrt{r_0^2-\xi^2} + C_2(r_0^2-\xi^2)$$

where $A_1 = p_1 + q_1x + rx^2$, $B_1 = -(q_1 + 2r_1x)$, $C_1 = r_1$, $A_2 = p_2 - q_2y + r_2y^2$, $B_2 = (p_2 - q_2y)$, $C_2 = r_2$, and $r_0 = \sqrt{\beta^2 - z^2}$.

The inner integral in Eq. (4.9) is computed as

$$\int_0^{\xi_2} u(x-\xi)\frac{w(\sqrt{r_0^2-\xi^2})-y)d\xi}{\sqrt{r_0^2-\xi^2}} = I_{term1} + I_{term2} + I_{term3} \tag{4.17}$$

where $I_{term1} = \frac{1}{8}(C_1C_2r_0^4 + 4C_1A_2r_0^2 + 4A_1C_2r_0^2 + 8A_1A_2)\tan\left(\frac{\xi_2}{\sqrt{r_0^2-\xi^2}}\right)$, $I_{term2} = \sqrt{r_0^2-\xi_2^2}\frac{1}{8}\xi_2(4A_1C_2 - C_1C_2r_0^2 + 2C_1C_2\xi_2^2 - 4A_2C_1) - \sqrt{r_0^2-\xi^2}(B_1A_2 + \frac{1}{3}B_1C_2(r_0^2-\xi^2))$ and $I_{term3} = \frac{1}{3}C_1B_2\xi_2^3 + \frac{1}{2}B_1B_2\xi_2^2 + A_1B_2\xi$.

The first term

The I_{term1} is rewritten as

$$T(\beta) = t_1\beta^4 + t_2\beta^2 + t_3$$

where $t_1 = \frac{1}{8}C_1C_2$, $t_2 = \frac{1}{2}(C_1A_2 + A_1C_2) - \frac{1}{4}C_1C_2z^2$ and $t_3 = \frac{1}{8}C_1C_2\beta^4 - \frac{1}{2}(C_1A_2 + A_1C_2)z^2 + A_1A_2$.

Substituting the first term I_{term1} from Eq. (4.17) into Eq. (4.9) and transforming $\tan^{-1}(\cdot)$ according to Eq. (4.11), the pressure calculation result for the first term I_{term1} in Eq. (4.17) becomes

$$P_{term1-2D}(x,y,z;k) = \frac{c}{2\pi}\left(\sum_{i=1}^{4} q_{3i}\int_{m_i}^{n_i}\int_{\sigma_i}^{0} T(\beta)e^{-jk\beta}d\beta\frac{h_i}{h_i^2+\sigma^2}d\sigma\right). \quad (4.18)$$

where $q_{31} = q_{33} = 1$ and $q_{32} = q_{34} = -1$.

The inner integral in Eq. (4.18) is computed analytically

$$\int_{\sigma_i}^{0} e^{-jk\beta}T(\beta)d\beta = \int_{\sigma_i}^{0} e^{-jk\beta}(t_1\beta^4 + t_2\beta^2 + t_3)d\beta$$

$$= \frac{1}{jk^5}e^{-jk\beta}(T_1\beta^4 + T_2\beta^3 + T_3\beta^2 + T_4\beta + T_5)|_{\sigma_i}^{0}$$

where $T_1 = -t_1k^4$, $T_2 = 4jk^3t_1$, $T_3 = 12k^2t_1$, $T_4 = 2jk^3t_2 - 24jkt_1$, and $T_5 = 2t_2k^2 - t_3k^4 - 24t_1$.

The first integral in Eq. (4.18) is given by

$$P_{term1-2D}(x,y,z;k) =$$

$$\frac{c}{-jk^5 2\pi}\sum_{i=1}^{4} q_{3i}\int_{m_i}^{n_i}\left[T_1h_i(\sigma^2+h_i^2)e^{-jk\sigma_i} + h_i(2T_1z^2 + T_2\sigma_i + T_3)e^{-jk\sigma_i}\right.$$

$$\left. + h_i(T_2z^2 + T_4)\frac{\sigma_i e^{-jk\sigma_i} - ze^{-jkz}}{\sigma^2+h_i^2} + (T_1z^4 + z^2T_3 + T_5)h_i\frac{e^{-jk\sigma_i} - e^{-jkz}}{h_i^2+\sigma^2}\right]. \quad (4.19)$$

The second term

Substituting I_{term2} in Eq. (4.17) into each double integral in Eq. (4.9) and performing the change the variable $\sigma = \sqrt{\beta^2 - z^2 - \xi_2^2}$ produces the analytical expression given by

$$P_{term2-2D}(x, y, z; k) =$$

$$\sum_{i=1}^{4} q_{2i} \int_{m_i}^{n_i} e^{-jk\sigma_i} \left[\frac{1}{8}\sigma h_i (4A_1C_2 - 4A_2C_1 + C_1C_2h_i^2 - C_1C_2\sigma^2) \right.$$

$$\left. -\sigma(B_1A_2 + \frac{1}{3}B_1C_2\sigma^2) + \sqrt{\sigma^2 + h_i^2}(B_1A_2 + \frac{1}{3}(\sigma^2 + h_i^2)) \right] \frac{\sigma}{\sigma_i} d\sigma, \qquad (4.20)$$

where the values of the q_{2i} are $q_{21} = q_{24} = -1$ and $q_{22} = q_{23} = 1$.

The third term

Substituting I_{term3} in Eq. (4.17) into each double integral in Eq. (4.9) and performing the change the variable $\sigma = \sqrt{\beta^2 - z^2 - \xi_2^2}$ produces the analytical expression given by

$$P_{term3-2D}(x, y, z; k) =$$

$$\frac{-1}{-jk} \left(\frac{1}{3}C_1B_2h_1^3 + \frac{1}{2}B_1B_2h_1^2 + A_1B_2h_1 \right) \left(e^{-jkd_2} - e^{-jkd_1} \right)$$

$$+\frac{1}{-jk} \left(\frac{1}{3}C_1B_2h_i^3 + \frac{1}{2}B_1B_2h_i^2 + A_1B_2h_i \right) \left(e^{-jkd_4} - e^{-jkd_3} \right)$$

$$+\Sigma_{i=3}^{4} q_{2i} \int_{m_i}^{n_i} e^{-jk\sigma_i} \frac{\left(\frac{1}{3}C_1B_2\sigma^3 + \frac{1}{2}B_1B_2\sigma^2 + A_1B_2\sigma \right)\sigma}{\sigma_i} d\sigma. \qquad (4.21)$$

The final equation for the 2D quadratic apodization

The total pressure in Eq. (4.9) is the sum of the three terms given by Eq. (4.19), Eq. (4.20) and Eq. (4.21), thus

$$P_{2D}(x,y,z;k) = P_{term1-2D}(x,y,z;k)$$

$$+P_{term2-2D}(x,y,z;k) + P_{term3-2D}(x,y,z;k). \tag{4.22}$$

4.1.5 The 2D apodized FNM

To obtain the formula for the 2D apodized FNM, origin of the coordinate system needs to be shifted from the center of the source to the lower left corner of the rectangular source. The observation point (x_1, y_1, z_1) is then defined as

$$\begin{aligned} x_1 &= x + a \\ y_1 &= y + b \\ z_1 &= z. \end{aligned} \tag{4.23}$$

The time-harmonic pressure generated by an apodized rectangular source computed with the 2D apodized FNM is now given by

$$p_{apod}(x_1,y_1,z_1;k) = -\frac{\rho c v_0 e^{j\omega t}}{2\pi} \sum_{i=1}^{4} \int_0^{2a}\int_0^{2b} T_{1i} h_{1i} \frac{e^{-jk\sqrt{\alpha_{1i}^2+z_1^2+h_{1i}^2}} - e^{-jkz_1}}{\alpha_{1i}^2 + h_{1i}^2} d\mu d\nu$$

$$-\frac{\rho c v_0 e^{j\omega t}}{2\pi} \sum_{i=1}^{4} \int_{n_i}^{m_i} T_{2i} h_{2i} \frac{e^{-jk\sqrt{\alpha_{2i}^2+z_1^2+h_{2i}^2}} - e^{-jkz_1}}{\alpha_{2i}^2 + h_{2i}^2} d\sigma \tag{4.24}$$

where the values of T_{1i} are $T_{11} = T_{12} = -\frac{\partial f(\mu,\nu)}{\partial \nu}$ and $T_{13} = T_{14} = -\frac{\partial f(\mu,\nu)}{\partial \mu}$, the values of α_{1i} are $\alpha_{11} = \alpha_{12} = \mu - x_1$ and $\alpha_{13} = \alpha_{14} = \nu - y_1$, and the values

of h_{1i} are $h_{11} = y_1$, $h_{12} = \nu - y_1$, $h_{13} = x_1$, and $h_{14} = \mu - x_1$. The values of T_{2i} are $T_{21} = T_{22} = f(\sigma, 2b)$ and $T_{23} = T_{24} = f(2a, \sigma)$, the values of α_{2i} are $\alpha_{21} = \alpha_{22} = \sigma - x_1$ and $\alpha_{23} = \alpha_{24} = \sigma - y_1$, the values of h_{2i} are $h_{21} = y_1$, $h_{22} = 2b - y_1$, $h_{23} = x_1$, and $h_{24} = 2a - x_1$, and the values of (m_i, n_i) are $(m_1, n_1) = (m_2, n_2) = (2a,\ 0)$ and $(m_3, n_3) = (m_4, n_4) = (2b,\ 0)$ for $i = 1, 2, 3, 4$.

4.1.6 The Rayleigh-Sommerfeld integral

The time-harmonic pressure generated by apodized rectangular source is also computed with the Rayleigh-Sommerfeld integral [6] via

$$P_{Rayleigh}(x_1, y_1, z_1; k) = \frac{j\omega\rho v_0 e^{j\omega t}}{2\pi} \int_0^{2a} \int_0^{2b} f(\mu, \nu) \frac{e^{-jkR}}{R} d\mu d\nu, \tag{4.25}$$

where $R = \sqrt{(x_1 - \mu)^2 + (y_1 - \nu)^2 + z_1^2}$ is the distance between the observation point $(x_1,\ y_1,\ z_1)$ and the source point $(\mu,\ \nu,\ 0)$.

4.1.7 Error Calculations

Let $P(x, y, z; k)$ represent the computed pressure field, and let $P_{ref}(x, y, z; k)$ represent the reference pressure field. The peak normalized error is given by

$$\eta_{max} = \frac{|P(x, y, z; k) - P_{ref}(x, y, z; k)|_{\max(x,y,z)}}{|P_{ref}(x, y, z; k)|_{\max(x,y,z)}}. \tag{4.26}$$

Table 4.1. Simulation parameters that achieve peak normalized error values of 10%, 1%, and 0.1% for the 1D quadratic apodization function $u(x) = u^2 - x^2$. Parameters listed include the number of Gauss abscissas, the computation time, and the computation time relative to the polynomial apodized FNM for the Rayleigh-Sommerfeld integral.

Peak Normalized Error	10%		1%		0.1%	
	FNM	Rayleigh	FNM	Rayleigh	FNM	Rayleigh
Gauss abscissas	8	32×32	10	74×74	11	122×122
Time (seconds)	0.0761	1.4147	0.0924	7.5038	0.0991	20.3334
Computation time relative to the polynomial apodized FNM	1×	18.58×	1×	81.17×	1×	205.11×

4.2 Results

4.2.1 1D quadratic apodization

Reference pressure field

Simulation are performed with a rectangular source, where each side is equal to $2a$ =4 wavelengths. The origin of the coordinate system is the center of the rectangular source. The reference pressure field is computed for the apodization function $u(x) = x^2 - a^2$ using the Rayleigh-Sommerfeld integral in Eq. (4.25) with 10,000 Gauss abscissas in each direction. The reference pressure shown in Figure 4.1 is evaluated in the $y = 0$ plane. The grid in the x direction extends from 0 to 4 wavelengths, and the grid in the z direction is evaluated from 0.04 to 4 wavelengths. The sample spacing in the x direction is 0.05 wavelengths and the sample spacing in the z direction is 0.04 wavelengths. The total number of grid points is 8100.

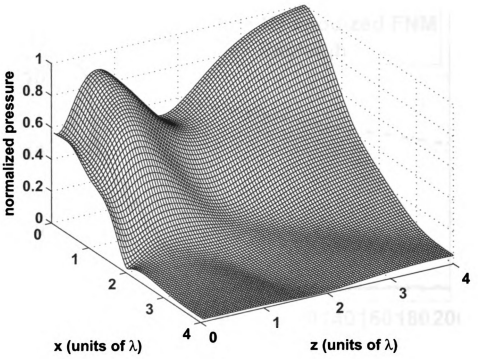

Figure 4.1. Normalized simulated time-harmonic reference pressure field in the $y = 0$ plane for a rectangular source with each side equal to 4 wavelengths. The pressure field is computed with $10,000$ Gauss abscissas in each direction using the Rayleigh-Sommerfeld integral with the 1D quadratic apodization $u(x) = x^2 - a^2$.

Error comparisons and computation times

The numerical errors and computation times for the polynomial apodized FNM and the Rayleigh-Sommerfeld integral are given in Figure 4.2. Figure 4.2 (a) shows that for a given number of Gauss abscissas in one direction, the polynomial apodized FNM always achieves a smaller error than the Rayleigh-Sommerfeld integral. The polynomial apodized FNM achieves a maximum error of 10^{-14} with less than 80 Gauss abscissas while the Rayleigh-Sommerfeld integral only achieves a maximum error of 10^{-5} when 200×200 Gauss abscissas are applied. Figure 4.2 (b) shows the computation times for the polynomial apodized FNM and the Rayleigh-Sommerfeld

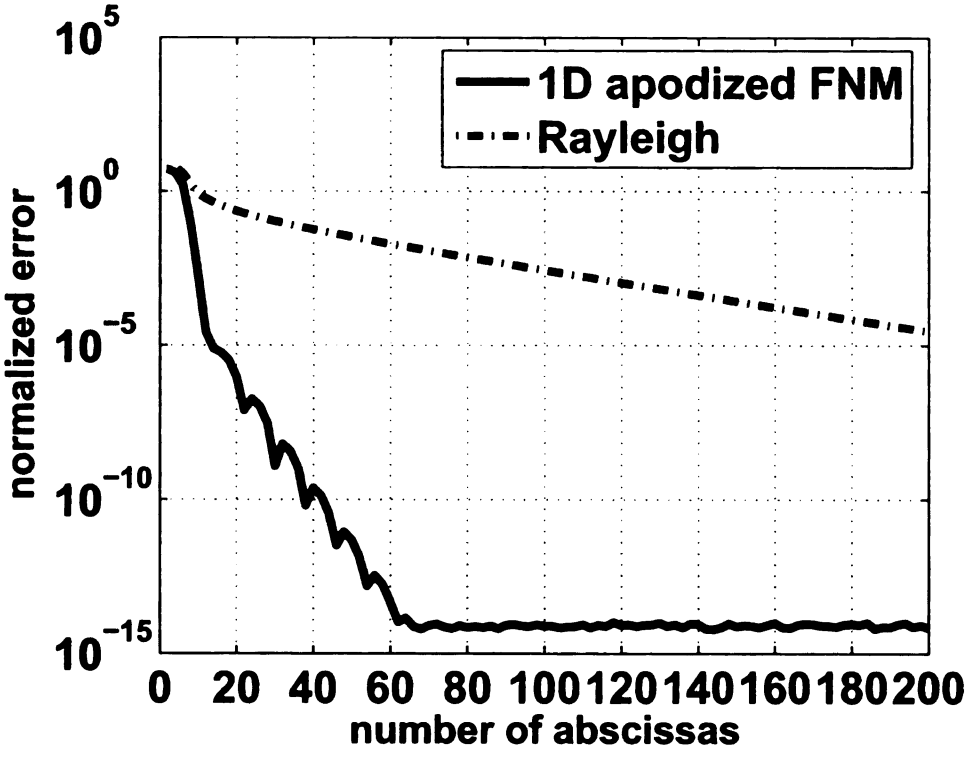

a) Maximum errors.

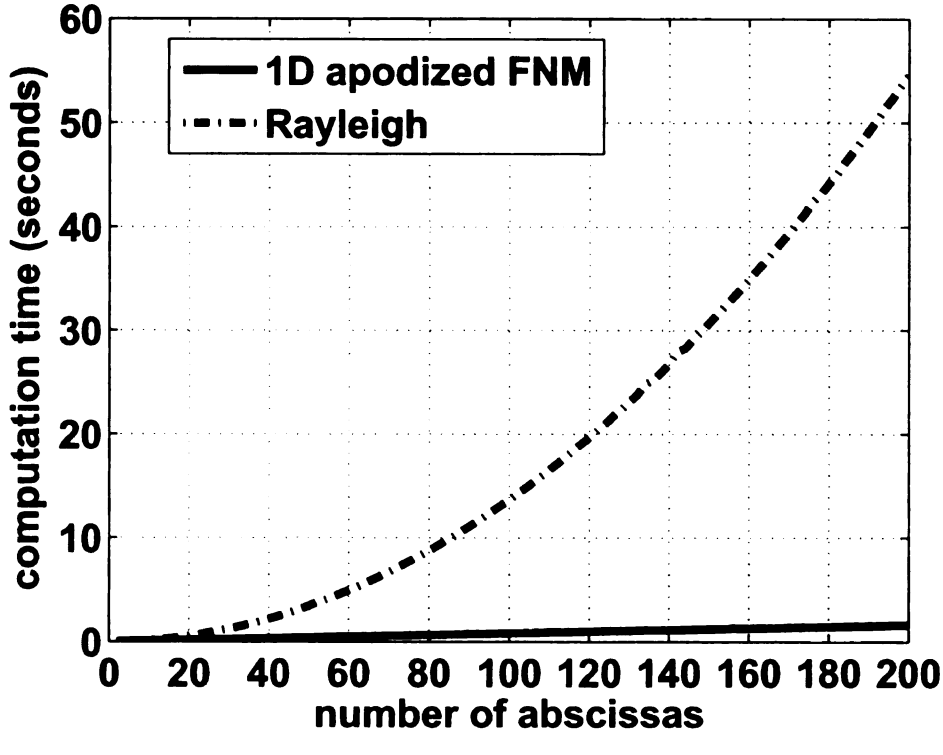

b) Computation times

Figure 4.2. a) Maximum errors and b) computation times for the polynomial apodized FNM and the Rayleigh-Sommerfeld integral.

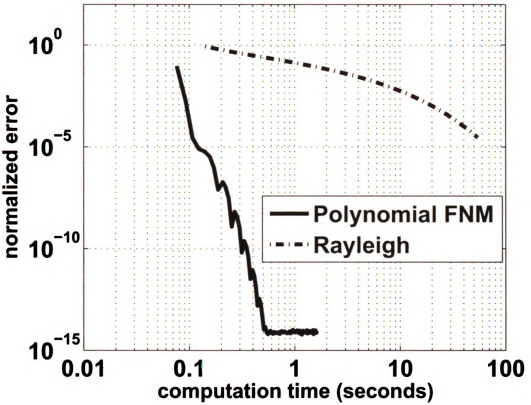

Figure 4.3. Time vs. error comparison between the polynomial apodized FNM and the Rayleigh-Sommerfeld integral. For the same computation time, the polynomial apodized FNM achieves smaller errors, and for the same error, the polynomial apodized FNM requires less time.

integral as a function of N, the number of Gauss abscissas in each direction. in Figure 4.2 (b), the polynomial apodized FNM consistently requires less time for the same value of N.

Figure 4.3 shows the computation times and the errors evaluated with the 1D polynomial apodized FNM and the Rayleigh-Sommerfeld integral on the same plot. In Figure 4.3, the polynomial apodized FNM achieves smaller errors for the same computation time, and the apodized FNM uses less time to achieve the same error value. Comparisons between the polynomial apodized FNM and Rayleigh-Sommerfeld inte-

gral are summarized in Table 4.1. For 10% peak normalized error, the polynomial apodized FNM is 18.58 times faster than the Rayleigh-Sommerfeld integral, for 1% peak normalized error, the polynomial apodized FNM is 81.17 times faster than the Rayleigh-Sommerfeld integral, and for 0.1% peak normalized error, the polynomial apodized FNM is 205.11 times faster than the Rayleigh-Sommerfeld integral. These values were obtained for the grid, quadratic apodization function, and piston geometry used here.

4.2.2 2D Apodization function

The pressure field is also evaluated for a square piston with an apodization function $u(x,y) = (x^2 - a^2)(y^2 - a^2)$. The reference pressure is computed using the Rayleigh-Sommerfeld integral in Eq. (4.25) with 10,000 Gauss abscissas in each direction. The reference pressure shown in Figure 4.1 is computed in the $y = 0$ plane. The grid in the x direction extends from 0 to 4 wavelengths, and the grid in the z direction is evaluated from 0.04 to 4 wavelengths. The sample spacing in the x direction is 0.05 wavelengths, and the sample spacing in the z direction is 0.04 wavelengths. The total number of grid points is 8100.

Error comparisons and computation times

The numerical errors and computation times for the 1D polynomial apodized FNM, 2D apodized FNM, and the Rayleigh-Sommerfeld integral are given in Figure 4.5. The apodization function is a 2D function given by $u(x,y) = (x^2 - a^2)(y^2 - a^2)$. Figure 4.5 (a) shows that, for a given number of Gauss abscissas in one direction, the computation time of 1D the polynomial apodized FNM is always smaller than the 2D apodized FNM and the Rayleigh-Sommerfeld integral. The 1D polynomial apodized FNM converges very rapidly, and an error of 10^{-14} is achieved with less than 80 Gauss abscissas. For the same piston and grid geometry, the 2D apodized

Table 4.2. Simulation parameters that achieve peak normalized error values of 10%, 1%, and 0.1% for the 2D apodization function $u(x,y) = (x^2 - a^2)(y^2 - a^2)$, where $a =$ 2 wavelengths. Parameters listed include the number of Gauss abscissas, computation time, and the ratio of the computation time relative to the polynomial apodized FNM. (a) 10% peak normalized error, (b) 1% peak normalized error and (c) 0.1% peak normalized error.

(a)

Peak normalized error	10%		
	1D FNM	2D FNM	Rayleigh-Sommerfeld
Gauss abscissas	10	8×8	34×34
Time (seconds)	0.0816	0.1306	1.1828
Computation time relative to the polynomial apodized FNM	1×	1.60×	14.49×

(b)

Peak normalized error	1%		
	1D FNM	2D FNM	Rayleigh-Sommerfeld
Gauss abscissas	10	14×14	78×78
Time (seconds)	0.0816	0.3708	6.1866
Computation time relative to the polynomial apodized FNM	1×	4.54×	75.78×

(c)

Peak normalized error	0.1%		
	1D FNM	2D FNM	Rayleigh-Sommerfeld
Gauss abscissas	12	28×28	126×126
Time (seconds)	0.0957	1.3986	16.3940
Computation time relative to the polynomial apodized FNM	1×	14.61×	171.25×

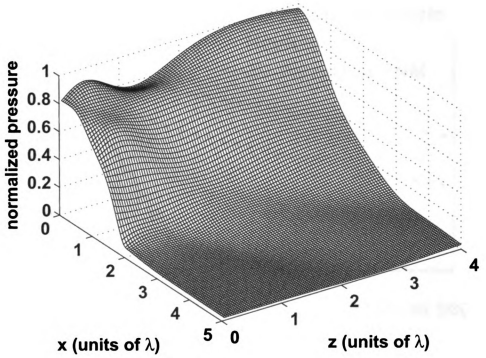

Figure 4.4. Absolute value of the simulated time-harmonic reference pressure field in the $y = 0$ plane for a square source with each side equal to 4 wavelengths. The apodization function is a 2D function given by $u(x, y) = (x^2 - a^2)(y^2 - a^2)$, where a =2 wavelengths. The pressure field is computed with 10,000 Gauss abscissas in each direction using the Rayleigh-Sommerfeld integral.

FNM achieves an error of 10^{-6} with 100×100 Gauss abscissas, and the Rayleigh-Sommerfeld integral acheives an error of 10^{-5} when 200×200 Gauss abscissas are applied.

Figure 4.2 shows the computation times and the errors evaluated with the 1D polynomial apodized FNM, 2D apodized FNM and the Rayleigh-Sommerfeld integral on the same plot. In Figure 4.2, the 1D polynomial apodized FNM converges to the smallest errors in the least amount of time. Comparisons among the 1D polynomial apodized FNM, the 2D apodized FNM and Rayleigh-Sommerfeld integral are summarized in Table 4.2. For 10% peak normalized error, the 1D polynomial apodized

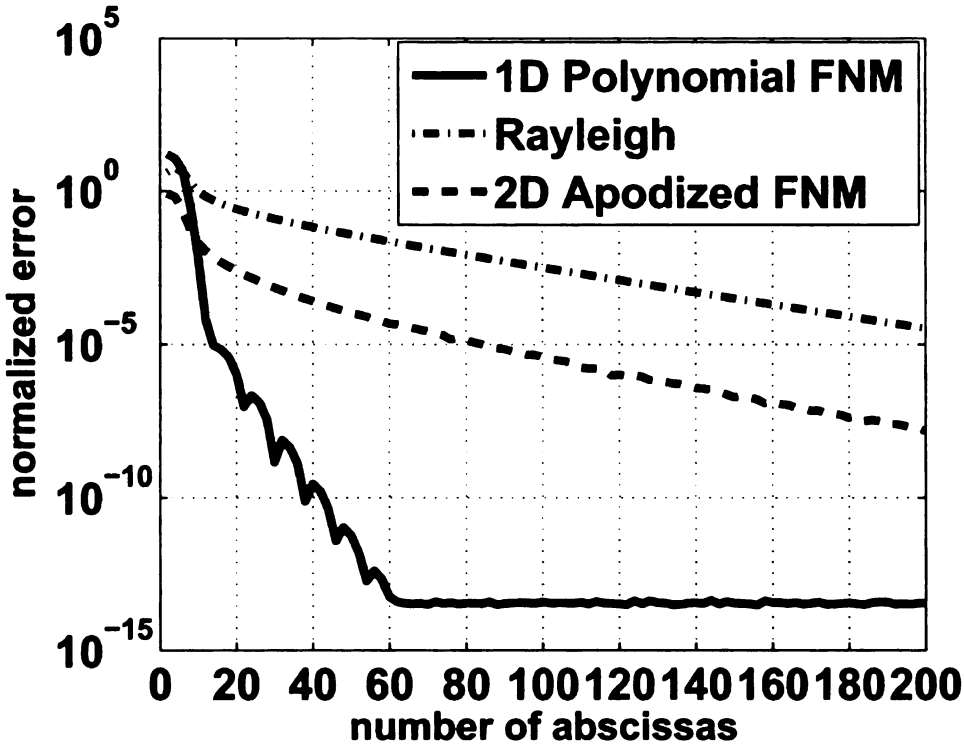

a) Maximum errors

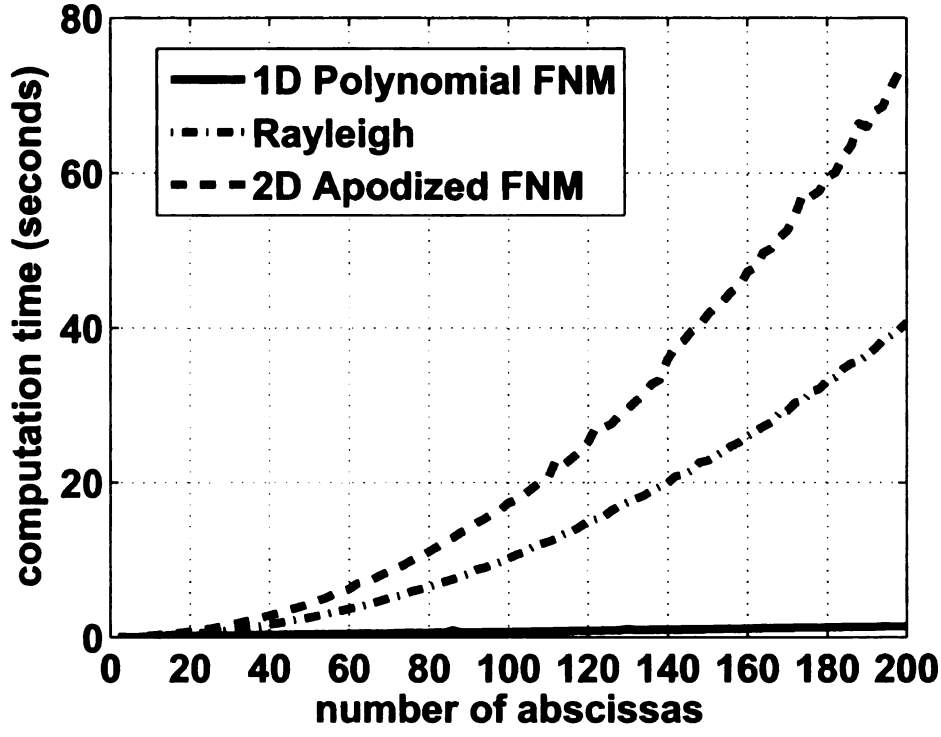

b) Computation times

Figure 4.5. a) Maximum errors and b) computation times plotted as a function of the number of Gauss abscissas for a 2D apodization function with the 1D polynomial apodized FNM, the 2D apodized FNM and the Rayleigh-Sommerfeld integral.

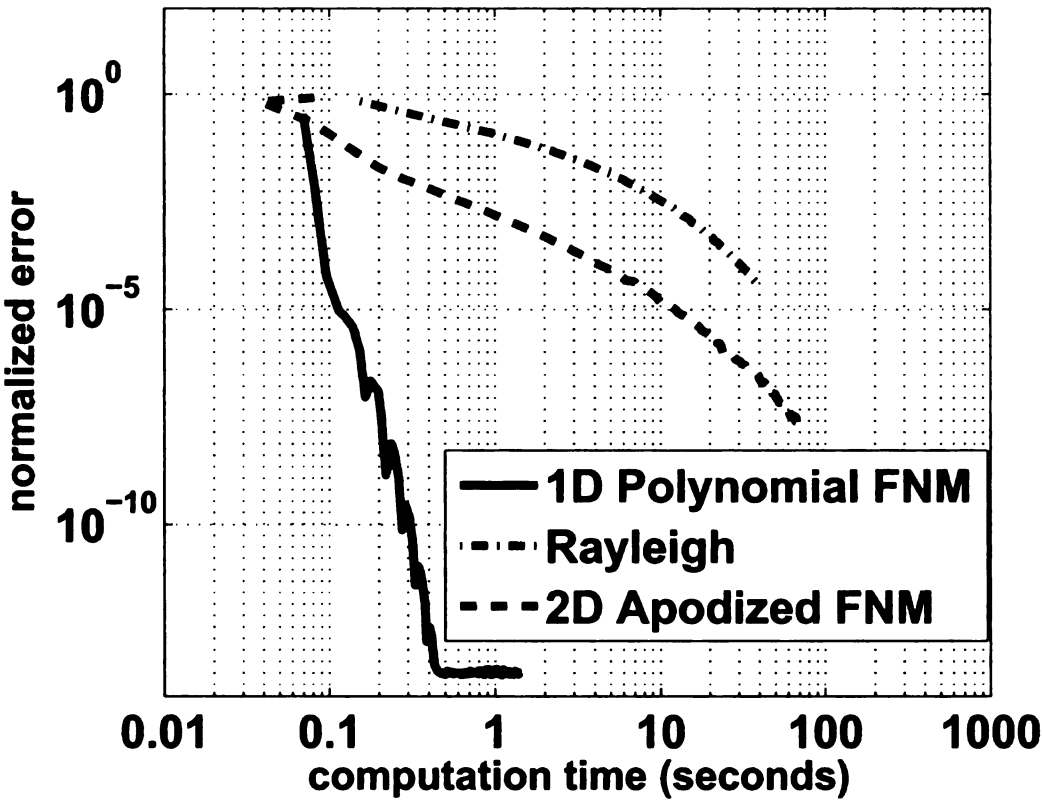

Figure 4.6. Time vs. error comparison between the 1D polynomial apodized FNM, 2D apodized FNM and the Rayleigh-Sommerfeld integral. The polynomial apodized FNM converges to smallest errors with least time.

FNM is 1.6 and 14.49 times faster than the 2D apodized FNM and the Rayleigh-Sommerfeld integral, respectively. The 1D polynomial apodized FNM is 4.54 and 75.78 times faster than the 2D apodized FNM and the Rayleigh-Sommerfeld integral for a 1% peak normalized error, respectively. For 0.1% peak normalized error, the polynomial apodized FNM is 14.61 and 171.25 times faster than the 2D apodized FNM and the Rayleigh-Sommerfeld integral for the grid, 2D apodization function, and piston geometry used in this paper.

4.3 Discussion

4.3.1 Advantages and disadvantages

The 1D polynomial apodized FNM successfully reduces the two-dimensional apodized pressure calculation integral in Eq. (3.1) into a single integral in Eqs. (4.16) and (4.22). As shown in Section 4.2, the performance of the 1D polynomial apodized FNM outperforms the 2D apodized FNM and the Rayleigh-Sommefeld integral for peak normalized errors of 10%, 1% and 0.1%. Furthermore, due to the rapid convergence of this method, the 1D polynomial apodized FNM is an ideal method for reference pressure field calculations.

The 1D polynomial apodized FNM equations in Eqs. (4.16) and (4.22) are applicable to polynomials of order up to two. When the order of the polynomial apodization function is increased, the polynomial apodized FNM formula needs to be rederived. For 2D apodization functions, the current polynomial apodized FNM only handle apodization functions that are separable in the spatial coordinates. For example, the apodization function $f(\mu, \nu) = \sqrt{\mu^2 + \nu^2}$ can not be evaluated with expressions in Eqs. (4.16) and (4.22). For this apodization function, the 2D apodized FNM expression is required.

4.3.2 Interpolation of the apodization function

The convergence of the 1D polynomial apodized FNM is very fast compared to the 2D apodized FNM and the Rayleigh-Sommerfeld integral. Though equations (4.16) and (4.22) are specialized for the polynomial apodization functions, other apodization functions can be approximated with polynomials. The most commonly used apodization functions are $\sin(\cdot)$, $\cos(\cdot)$ and $\exp(\cdot)$, which can all be approximated using polynomials within a certain input range of parameters. For these apodization functions, expressions for the 1D polynomial apodized FNM with higher order

polynomial apodization functions are needed.

4.4 Conclusion

A 1D polynomial apodized fast nearfield method for calculating nearfield pressures generated by a polynomial apodized rectangular piston is derived and evaluated. The derivation is based on the instantaneous impulse response for rectangular piston given by Scarano et al [44]. The 1D polynomial apodized FNM expressions for two apodization function, $u(x) = x^2 - a^2$ and $u(x, y) = (x^2 - a^2)(y^2 - a^2)$, are given. The results of the 1D polynomial apodized FNM are compared with the 2D apodized FNM and the Rayleigh-Sommerfeld integral. The results show that the 1D polynomial FNM achieves the best performance among all of the three methods for the same number of Gauss abscissas. Thus, the 1D polynomial apodized FNM is an ideal method for calculating nearfield pressure generated by a polynomial apodized rectangular source.

CHAPTER 5

A Fast Nearfield Method for the Numerical Evaluation of 3D Potential Integrals

The evaluation of potential integrals over a volume domain are important calculations in scattering problems. For example, Moraros and Popovic [23] optimize the volume potential integrals involved in the moment-method analysis of 3D dielectric scatters. The precorrected-FFT solution is proposed by Nie et. al. [45] to solve the volume-surface integral equation for scattering from conducting-dielectric objects. Potential integrals are often singular and thus direct evaluation potential integrals may encounter numerical difficulties. For potential integrals with singularities, singularity subtraction [23, 25, 26, 27, 28] or singularity cancellation methods [30, 31, 32, 33] are often used. Both singularity subtraction methods and singularity cancellation methods retain the same number of dimension over the integration as the original potential integrals. Typically, those methods manipulate the integrands to eliminate singularties and to achieve better performance. This approach is reasonable for general potential integrals; however, when uniform potential integrals are considered,

more efficient methods can further improve the numerical performance by reducing the number of dimension over the integration.

Pressure fields from uniformly excited planar sources can be computed using both the Rayleigh-Sommerfeld integral [6] and the fast nearfield method (FNM) [8, 12]. Those two methods are mathematically equivalent but the numerical performance differs. Of these, the FNM achieves a smaller error in less time because the FNM eliminates the $1/R$ singularity in the Rayleigh-Sommerfeld integral by subtracting the singularity in the integrand. The integrands of the potential integrals and the pressure integrals are the same. For potentials from uniform planar sources, the FNM can be directly applied. However, the FNM expressions for uniformly excited volume sources are also needed.

To improve the performance of potential integral calculations for volume sources, a single FNM integral is derived from the FNM expression for uniformly excited polygonal pistons. The derivation begins after the relationship between FNM expressions and potential integrals is established. Then, FNM expressions for potential integrals are obtained for a polygonal source. The prism is subdivided into five subdomains, and the total potential is obtained by superposing by the potential produced by all of the subdomains. After substituting the FNM expression for polygonal source into the potential integral for the subvolume, performing a change of variable and exchanging the order of integration, a 1D FNM volume integral is obtained for a volume source that is nuiformly excited. The resulting 1D FNM expression for the potential and the singularity cancellation method are then evaluated on six single observation points and on a large 3D grid. The results indicate that, when compared to calculations performed with the singularity cancellation method, the FNM requires fewer sample points to achieve a given accuracy.

5.1 FNM Calculations for Rectangular and Triangular Sources

5.1.1 The potential integral

The time-harmonic pressure produced by a triangular transducer can be obtained using the Rayleigh-Sommerfeld diffraction integral

$$P(x,y,z,t) = \frac{j\rho w v_0 e^{-j\omega t}}{\lambda k} \iint_s \frac{e^{-jkR}}{R} ds \tag{5.1}$$

where s is area of the triangular source, ω is the excitation frequency in radians per second, ρ is the density of the medium, v_0 is a constant normal velocity evaluated at the surface of the triangular piston, k is the wavenumber, t is the elapsed time and R is the distance from the source point to the observation point.

The potential integral considered is given by

$$\Phi(x,y,z) = \iiint_V \frac{e^{-jkR}}{4\pi R} dV \tag{5.2}$$

where V is the integration domain over which the integral is evaluated. The potential in Eq. (5.2) is normalized with respect to $-v_0 e^{jwt}$. The integrands in Eq. (5.1) and Eq. (5.2) are the same, but the former is evaluated over a surface and the latter is evaluated over a volume. Thus, the FNM expression that is analytically equivalent to Eq. (5.1) can also be extended to solve for the potential generated by a 3D source.

5.1.2 FNM calculations for a planar source

Let ΔABC denote a triangular source, and a, b, and c are the length of the corresponding sides that are located oppsite angles A, B, and C. According to the fast near-field method (FNM) [12], the potential integral evaluated over this triangular source at the observation point above the point A is given by

$$\Phi(x,y,z) = \iint_S \frac{e^{-jkR}}{4\pi R} ds = \frac{j}{4\pi k} l \int_{\frac{a^2-b^2-c^2}{2c}}^{\frac{a^2-b^2+c^2}{2c}} \frac{e^{-jk\sqrt{\sigma^2+z^2+l^2}} - e^{-jkz}}{\sigma^2+l^2} d\sigma, \tag{5.3}$$

where $(a^2-b^2-c^2)/(2c)$ and $(a^2-b^2+c^2)/(2c)$ are the lower and upper limits of the integration, respectively, z is the the orthogonal distance between the observation point and the source plane, and l represents the orthogonal distance between the vertex A and the base of the triangle (i.e., the height of the triangle).

The FNM expression for a planar source at an observation point (x,y,z) is obtained by first subdividing the planar source into several triangular subelements that share the vertex D that is defined by the projection of the observation point onto the planar source. Then, the pressure generated by each subelement is computed using Eq. (5.3), and finally the total pressure generated by the planar source is the summation of the pressure generated by each subelement

$$\Phi(x,y,z) = \frac{j}{4\pi k} \left(\sum_{i=1}^{N} \frac{E_i x + F_i y + G_i}{\sqrt{E_i^2+F_i^2}} \right.$$
$$\left. \times \int_{\frac{a_i^2-b_i^2-c_i^2}{2c_i}}^{\frac{a_i^2-b_i^2+c_i^2}{2c_i}} \frac{e^{-jk\sqrt{\sigma^2+z^2+h_i^2}} - e^{-jkz}}{\sigma^2+h_i^2} d\sigma \right), \tag{5.4}$$

where $E_i x + F_i y + G_i = 0$ describes the line that is coincident with each side of the planar source, a_i, b_i, and c_i are the parameters defined by Figure 5.1, and $h_i = \frac{E_i x+F_i y+G_i}{\sqrt{E_i^2+F_i^2}}$ is the distance from the projection of the observation point D to the edge of the trianguar source. The sign of h_i is defined such that the superposition of subelements correctly respresents the total potential generated by the flat planar source. The parameter N describes the number of sides/vertexes in the flat planar source where $N = 3$ for a triangular source and $N = 4$ a rectangular source.

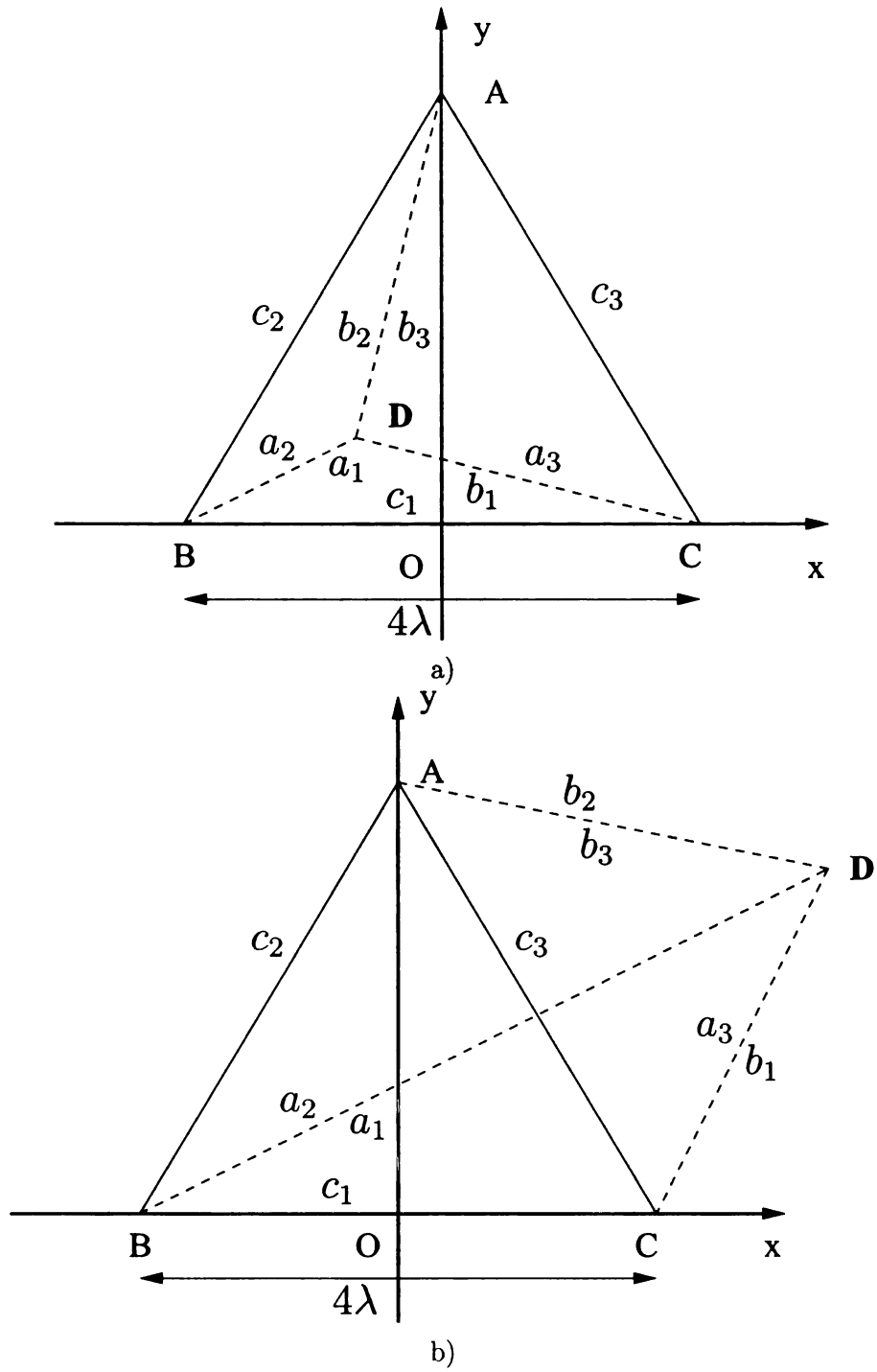

Figure 5.1. Parameters defined for FNM calculations with a triangular source ΔABC. The lengths a_i, b_i, and c_i are defined for three different triangles that share the vertex D in each subfigure. a). The projection of the observation point D is located inside of the triangular source. b). The projection of the observation point D is located outside of the triangular source.

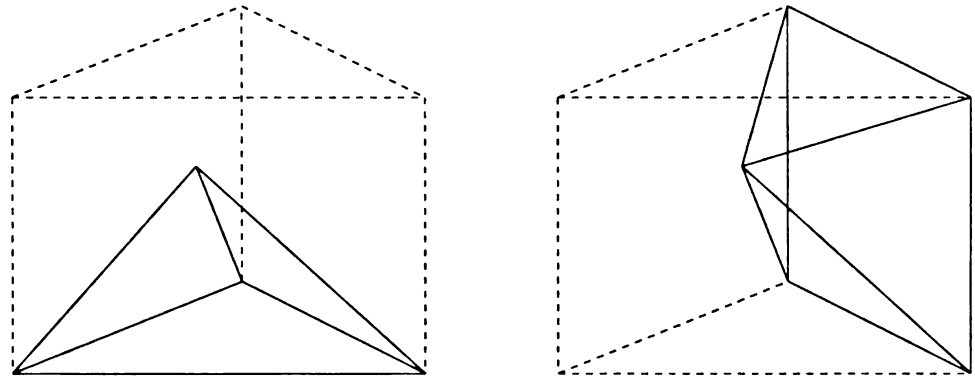

a) Subtetrahedron. b) Subpyramid.

Figure 5.2. Subdividing a prism about an observation point to form subtetrahedrons and subpyramids. (a). Subtetrahedron. (b). Subpyramid.

5.1.3 FNM calculations for a volume source

Three common examples of volume elements are tetrahedrons, bricks, and prisms. In order to calculate the volume potential integral, the volume is subdivided with respect to the observation point. For the volumes considered here, the domain can be subdivided into subtetrahedrons and/or subpyramids according to whether the face shape is a triangle or rectangle [31] as shown in Figure 5.2. Thus, efficient formulas for the subtetrahedrons and subpyramids are obtained.

FNM for subvolumes

In order to utilize the FNM expression for a planar source, the subvolumes are subdivided into layers of triangles and quadrilaterals. The procedure for calculating potential integrals for subvolumes is given by Khayat and Wilton [31] and is adapted here for the fast nearfield method.

1. Subdivide the volume element about the observation point into subdomains including subtetrahedrons and subpyramids.

2. For each subtetrahedron, choose the number of sample points along the height

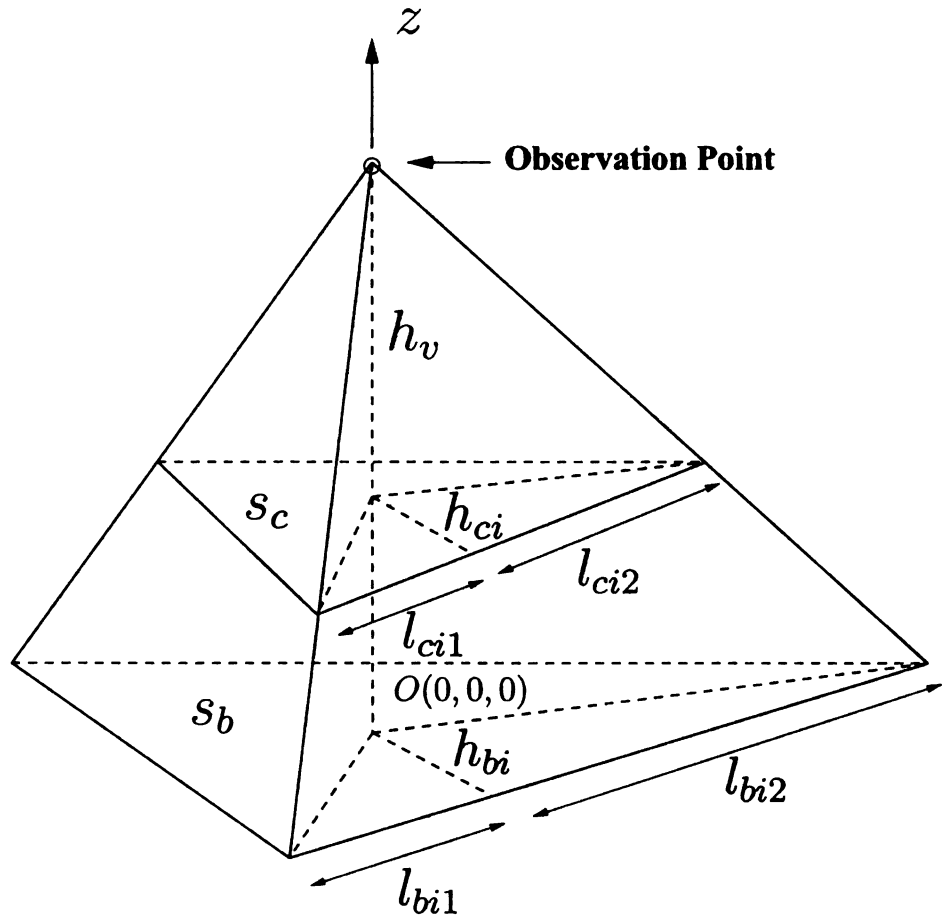

Figure 5.3. The geometric configuration indicating how the potential integral is evaluated for a subtetrahedron.

direction of the subtetrahedron. The cross-section at each sample point is a planar element.

3. Find the vertices and the projection of the observation point for each planar element.

4. Calculate each potential integral over the planar element using the fast nearfield method (FNM).

5. Transform the observation point from the global coordinate system to the local coordinate system.

For potential calculations within subdomains, a local coordinate system is used as shown in Figure 5.3 where the projection of the observation point onto the base plane is the origin of the local coordinate system and the base plane is located in the $z = 0$ plane of the local coordinate system. Let (x, y, z) denote the coordinates of the observation point in the local coordinate system. The potential integration over a subdomain V is given by

$$\Phi(x, y, z) = \iiint_V \frac{e^{-jkR}}{4\pi R} dV = \int_0^{h_v} \iint_s \frac{e^{-jkR}}{4\pi R} ds dz', \tag{5.5}$$

where h_v is the distance from the observation point to the base of the subtetrahedron (i.e., h_v is the height of the subtetrahedron). In the local coordinate system, $h_v = z$, where z is the local coordinate of the observation point. The inner integration over the source plane s represents the potential produced by a triangular source distribution, which is the shape of the subtetrahedronal cross-section. Figure 5.3 illustrates the geometrical configuration of the potential calculations over the subtetrahedron. The base plane is denoted as s_b, where b indicates the *base* plane, and the plane with a triangular cross-section is s_c at $z = z'$, where c represents the *cross* plane. The result of the inner integral is given by [12]

$$\iint_s \frac{e^{-jkR}}{4\pi R} ds = \frac{j}{4\pi k} \sum_{i=1}^{N} h_{ci} \int_{l_{ci1}}^{l_{ci2}} \frac{e^{-jk\sqrt{\sigma^2+(z-z')^2+h_{ci}^2}} - e^{-jk(z-z')}}{\sigma^2 + h_{ci}^2} d\sigma, \tag{5.6}$$

where the subscript c indicates that the parameters are all calculated in the s_c plane, h_i is the distance between the projection of the observation point on the s_c plane and each side of the source in the s_c plane, and l_{i1} and l_{i2} are the corresponding limits of integration. Since these parameters are related to the value of z', the relationship

$$\frac{h_{ci}}{h_{bi}} = \frac{l_{ci1}}{l_{bi1}} = \frac{l_{ci2}}{l_{bi2}} = \frac{z - z'}{z} \tag{5.7}$$

is defined using the similar triangles in Figure 5.3. In Eq. 5.7, the subscript b indicates the parameters that are all calculated in the s_b plane, and the subscript c indicates the parameters that are calculated in the s_c plane. Then, all terms containing the subscript c are substituted for the terms containing the subscript b according to Eq. (5.7), and then a change of variable according to the formula $\sigma = (z - z')/z * Q$ is performed, yielding

$$\iint_s \frac{e^{-jkR}}{4\pi R} ds = \frac{j}{4\pi k} \sum_{i=1}^{N} h_{bi} \int_{l_{bi1}}^{l_{bi2}} \frac{e^{-jk\frac{z-z'}{z}\sqrt{Q^2+z^2+h_{bi}^2}} - e^{-jk(z-z')}}{Q^2 + h_{bi}^2} dQ. \tag{5.8}$$

Eq. (5.8) readily computes the potential generated by the cross-section s_c when the position of the cross-section z' is known. The parameters h_i, l_{i1}, and l_{i2} are computed in the base plane and are the same for all cross-sections. Thus, the complexity compared to Eq. (5.6) is greatly reduced. After substituting Eq. (5.8) into Eq. (5.5) and exchanging the order of integration, Eq. (5.5) becomes

$$\Phi(x, y, z) = \frac{j}{4\pi k} \sum_{i=1}^{N} h_{bi} \int_{l_{bi1}}^{l_{bi2}} \int_0^z \frac{e^{-jk\frac{z-z'}{z}\sqrt{Q^2+z^2+h_{bi}^2}} - e^{-jk(z-z')}}{Q^2 + h_{bi}^2} dz' dQ. \tag{5.9}$$

The inner integral (with respect to z') is integrated analytically, so a single integral for the potential is obtained, which is described by

$$\Phi(x, y, z) = \frac{-1}{4\pi k^2} \sum_{i=1}^{N} h_{bi} \int_{l_{bi1}}^{l_{bi2}}$$

$$\frac{z(e^{-jk\sqrt{Q^2+z^2+h_{bi}^2}} - 1) - (e^{-jkz} - 1)\sqrt{Q^2 + z^2 + h_{bi}^2}}{(Q^2 + h_{bi}^2)\sqrt{Q^2 + z^2 + h_{bi}^2}} dQ. \tag{5.10}$$

Eq. (5.10) and Eq. (5.5) are analytically equivalent, but the numerical performance of each expression differs. Eq. (5.5) is a triple integral that includes a $1/R$ singularity. In Eq. (5.5), the total number of sample points is the multiplication of the number of sample points in each direction, which is much larger than the number of sample points required to evaluate the single integral in Eq. (5.10).

Volume FNM for the prism

To calculate the potential generated by a prism, the prism is subdivided about the observation point to form five subvolumes including three subpyramids and two subtetrahedrons. The potential of the prism is the superposition of the contributions from the five subdomains. Let $A_m x + B_m y + C_m z + D_m = 0$ denote the general form of the plane that passes through each face of the prism, where Φ_m is the result of the potential integral over each subdomain, then the overall potential over the prism Φ_{prism} is given by

$$\Phi_{prism} = \sum_{m=1}^{5} \frac{(A_m x + B_m y + C_m z + D_m)}{|A_m x + B_m y + C_m z + D_m|} \Phi_m. \tag{5.11}$$

The term $(A_m x + B_m y + C_m z + D_m)/|A_m x + B_m y + C_m z + D_m|$ is the sign function, which determines whether the contribution from a subdomain is positive or negative. The values of A_m, B_m, C_m and D_m are selected such that the contributions from all the subdomains for an observation point inside the prism are all positive.

5.1.4 Error calculations

For potential field calculations, the numerical error $\eta(x,\ y,\ z)$ is defined as the normalized difference between the reference field and the computed field according to

$$\eta(x,y,z) = \frac{|\Phi(x,y,z) - \Phi_{ref}(x,y,z)|}{max|\Phi_{ref}(x,y,z)|}, \tag{5.12}$$

Table 5.1. The geometry of the prism.

Vertex	1	2	3	4	5	6
(x, y, z) [m]	(0, 1, 0)	(0, 0, 0)	(1, 0, 0)	(0, 1, 1)	(0, 0, 1)	(1, 0, 1)

where $\Phi_{ref}(x, y, z)$ is the reference potential and $\Phi(x, y, z)$ is the computed pressure field. The maximum error η_{max} is defined as

$$\eta_{max} = \max_{x,y,z} \eta(x,\ y,\ z), \tag{5.13}$$

and the number of significant digits n is given as

$$n = log10(\eta_{max}). \tag{5.14}$$

5.2 Results

5.2.1 Comparisons of potential evaluated at single points

The shape of the prism is shown in Figure 5.4, and the coordinates of each vertex are given in Table 5.1. This is the same prism used in thesingularity cancellation method [31]. The wavelength is 10m. The observation points are located at (x, y, z) = (1/3m, 1/3m, d) where d = 0.5, 1.0, and 1.25 [m]. The reference potential given in Table 5.2 is calculated using the singularity cancellation method with 30, 30, and 30 Gauss abscissas in the x, y, and z directions, respectively. The reference potential is accurate to 15 digits. The input parameters and the values for the reference potential are given in Table 5.2.

The number of significant digits in each result is plotted as a function of the number of sample points for the FNM and the singularity cancellation method in Figure 5.5, which shows that the uniformly excited 1D FNM expression for the volume integral converges much faster than the singularity cancellation method. For the point

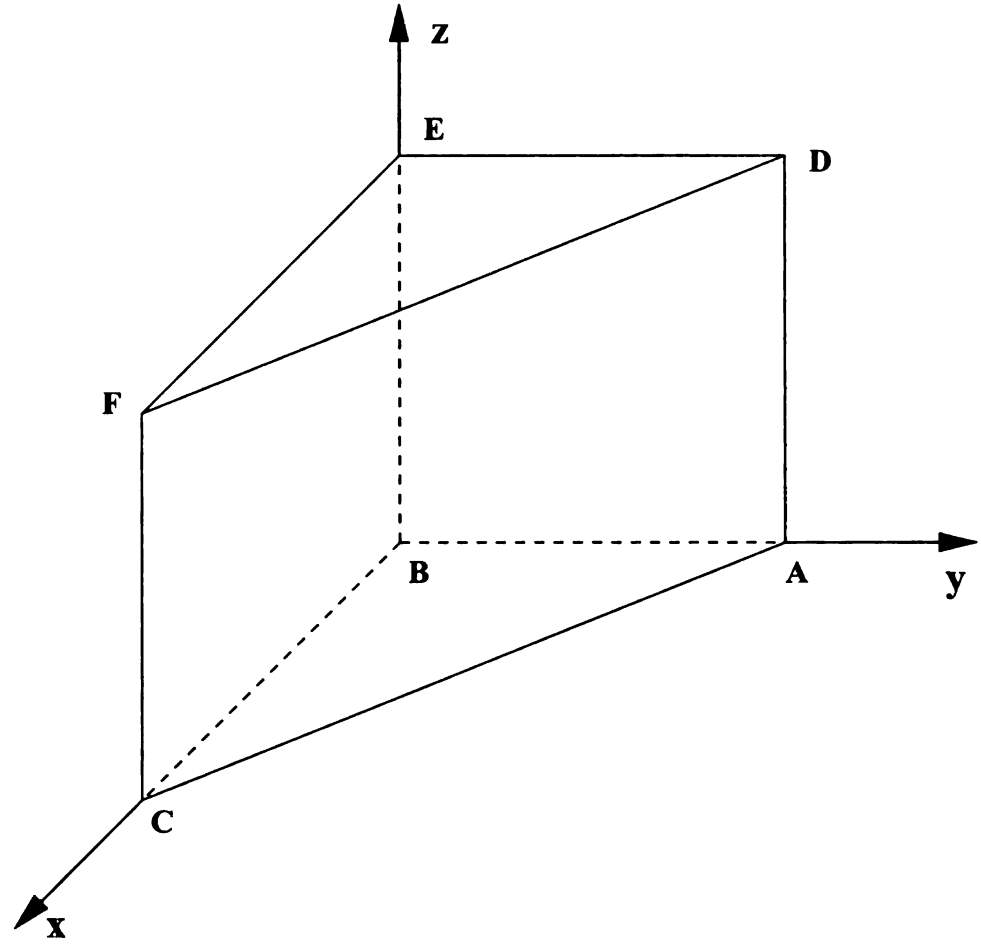

Figure 5.4. The prism geometry, where vertex B is coincident with the origin, and vertices C, A, and E are located on the x, y, and z axes, respectively.

(1/3m, 1/3m, 0.5m), the the uniformly excited 1D FNM expression for the volume integral uses 9, 9, 6, and 9 times fewer sample points than the singularity cancellation method for answers accurate to 2, 3, 4, and 5 significant digits, respectively. For the point (1/3m, 1/3m, 1.0m), the the uniformly excited 1D FNM expression for the volume integral uses 6, 12, 27, and 15.75 times fewer sample points than the singularity cancellation method for answers accurate to 2, 3, 4, and 5 significant digits, respectively. For the point (1/3m, 1/3m, 1.25m), the uniformly excited 1D FNM expression for the volume integral uses 6, 5, 12, and 10.125 times fewer sample

Table 5.2. Reference potential fields are evaluated at three points $(x,\ y,\ z) = (1/3m,\ 1/3m,\ d)$, where d = 0.5m, 1.0m and 1.25m. The reference fields are computed using the singularity cancellation method with 30, 30, and 30 abscissas in the x, y, and z directions, respectively.

Abscissas			Observation point			Real{Φ}	Imaginary{Φ}
x	y	z	x	y	z		
30	30	30	1/3	1/3	0.5	0.1101990007812	-0.0246818749055
30	30	30	1/3	1/3	1.0	0.07701456144055	-0.02427846658870
30	30	30	1/3	1/3	1.5	0.04833922443213	-0.02377978649190

points than the singularity cancellation method for answers accurate to 2, 3, 4, and 5 significant digits, respectively.

Next, the potentials are compared for values computed with the FNM and the singularity cancellation method where the observation points have small z values. The observation points are located at $(x,\ y,\ z) = (1/3\text{m},\ 1/3\text{m},\ d)$, where d = 0.1m, 0.01m, and 0.0001m. The reference potentials at the three observation points are given in Table 5.2.

The number of significant digits are plotted as a function of the number of sample points for the FNM and the singularity cancellation method in Figure 5.6. The FNM demonstrates similar performance to that demonstrated in Figure 5.5 for larger z values in terms of convergence for all three observation points with small z values. In contrast, the singularity cancellation method converges much more slowly for smaller z values such as z = 0.01m and z = 0.0001m. A comparison between Figure 5.6 and Figure 5.5 indicates that, as the z coordinate approaches zero, the uniformly excited 1D FNM expression for the volume integral and the singularity cancellation method converge more slowly. Table 5.5 summarizes the ratio of the number of sample points required to achieve a given accuracy with the uniformly excited 1D FNM expression for the volume integral and the singularity cancellation method for three points $(x,\ y,\ z) = (1/3\text{m},\ 1/3\text{m},\ d)$, where d = 0.1m, 0.01m, and 0.0001m.

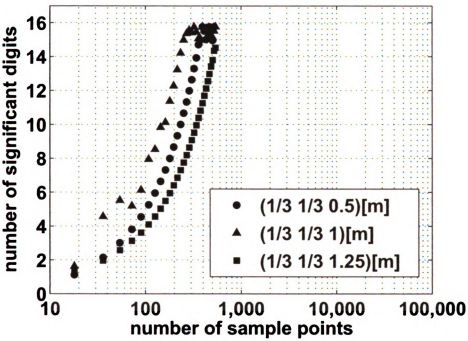

a) FNM

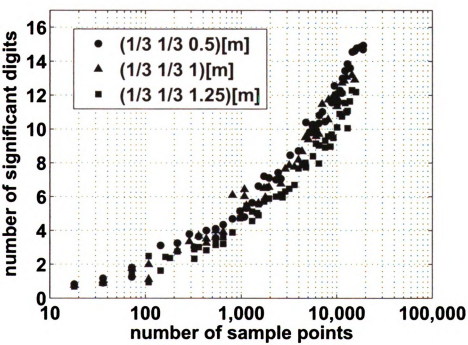

b) Singularity cancellation method

Figure 5.5. The number of significant digits in the computed potential for a prism plotted as a function of the number of sample points for three observation points $(x,\ y,\ z) = (1/3\text{m},\ 1/3\text{m},\ d)$, where $d = 0.5\text{m},\ 1.0\text{m}$, and 1.25m.

Table 5.3. Simulation parameters that achieve between 2 to 5 significant digits with the FNM and the singularity cancellation method for the potential evaluated on the observation points $(x,\ y,\ z) = (1/3,\ 1/3,\ d)$, where $d = 0.5,\ 1.0$, and 1.25 [m]. Parameters listed include the number of sample points for each observation point and the ratios of the number of sample points required to achieve a specific accuracy relative to the number required with the FNM. (a) Significant digits 2 and 3 and (b) Significant digits 4 and 5.

(a)

Observations	Significant digits	2		3	
		FNM	Sigularity cancellation	FNM	Sigularity cancellation
d =0.5	Sample points	36	324	54	324
	Sample points relative to FNM	1×	9×	1×	6×
d =1.0	Sample points	36	216	36	432
	Sample points relative to FNM	1×	6×	1×	12×
d =1.25	Sample points	54	324	72	360
	Sample points relative to FNM	1×	6×	1×	5×

(b)

Observations	Significant digits	4		5	
		FNM	Sigularity cancellation	FNM	Sigularity cancellation
d =0.5	Sample points	90	54	108	972
	Sample points relative to FNM	1×	6×	1×	9×
d =1.0	Sample points	36	972	72	1134
	Sample points relative to FNM	1×	27×	1×	15.75×
d =1.25	Sample points	108	1296	144	1458
	Sample points relative to FNM	1×	12×	1×	10.125×

Table 5.4. Reference potentials evaluated at three points (x, y, z) = (1/3m, 1/3m, d), where d = 0.1m, 0.01m, and 0.0001m. The reference potentials are computed using the singularity cancellation method with 30, 30, and 30 abscissas in the x, y and z directions, respectively.

Abscissas			Observation point			Re{Φ}	Imag{Φ}
x	y	z	x	y	z		
30	30	30	1/3	1/3	0.1	-0.09045651713588	0.02442323471174
30	30	30	1/3	1/3	0.01	-0.07858100147339	0.02429436586981
30	30	30	1/3	1/3	0.0001	-0.07703049150655	0.02427862714031

For the point (1/3m, 1/3m, 0.1m), the the uniformly excited 1D FNM expression for the volume integral uses 6, 7.7, 6.3, and 7.38 times fewer sample points than the singularity cancellation method to achieve 2, 3, 4, and 5 significant digits, respectively. For the point (1/3m, 1/3m, 0.01m), the uniformly excited 1D FNM expression for the volume integral uses 8, 10.8, 10.125, and 17.14 times fewer sample points than the singularity cancellation method to achieve 2, 3, 4, and 5 significant digits, respectively. For the point (1/3m, 1/3m, 0.0001m), the uniformly excited 1D FNM expression for the volume integral uses 12, 27, 25, and 10 times fewer sample points than the singularity cancellation method to achieve 2, 3, 4, and 5 significant digits, respectively.

5.2.2 The potential evaluated on a 3D grid

In this section, the potential is evaluated on a 3D grid. The x and y directions extend from -0.5m to 1.5m with an interval of 0.02m, and the z direction extends from 0 to 1.5m with an interval of 0.03m. The reference is computed using the singularity cancellation method evaluated with 1000 Gauss abscissas in each dimension. Figure 5.7 shows the number of sample points and the number of significant digits for the uniformly excited 1D FNM expression for the volume integral and the singularity cancellation method evaluated on a 3D grid. Table 5.6 summarizes the ratio of the number of sample points required to achieve a given accuracy with the uniformly

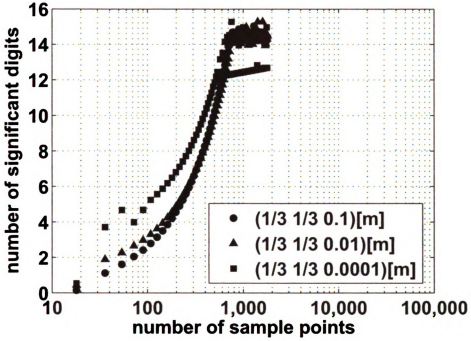

a) FNM.

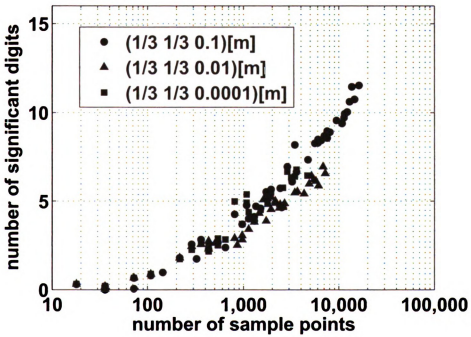

b) Singularity cancellation method.

Figure 5.6. The number of significant digits in the calculated potential achieved for the prism in Figure 5.4 plotted as a function of the number of sample points for three observation points $(x,\ y,\ z) = (1/3\text{m},\ 1/3\text{m},\ d)$, where $d = 0.1\text{m},\ 0.01\text{m}$, and 0.0001m.

Table 5.5. Simulation parameters that achieve between 2 to 5 significant digits with the uniformly excited 1D FNM expression for the volume integral and the singularity cancellation method for the potential evaluated at the observation points $(x,\ y,\ z) = (1/3\text{m},\ 1/3\text{m},\ d)$, where $d = 0.1\text{m},\ 0.01\text{m}$, and 0.0001m. Parameters listed include the number of sample points required at each observation point and the number of sample points required to achieve a specified error relative to the FNM. (a) Significant digits 2 and 3. (b) Significant digits 4 and 5.

(a)

Observations	Significant digits	2		3	
		FNM	Sigularity cancellation	FNM	Sigularity cancellation
d =0.1	Sample points	72	432	126	972
	Sample points relative to FNM	1×	6×	1×	7.7×
d =0.01	Sample points	54	432	90	972
	Sample points relative to FNM	1×	8×	1×	10.8×
d = 0.0001	Sample points	36	432	36	972
	Sample points relative to FNM	1×	12×	1×	27×

(b)

Observations	Significant digits	4		5	
		FNM	Sigularity cancellation	FNM	Sigularity cancellation
d =0.1	Sample points	180	1134	234	1728
	Sample points relative to FNM	1×	6.3×	1×	7.38×
d =0.01	Sample points	144	1458	126	2160
	Sample points relative to FNM	1×	10.125×	1×	17.14×
d = 0.0001	Sample points	72	1080	108	1080
	Sample points relative to FNM	1×	15×	1×	10×

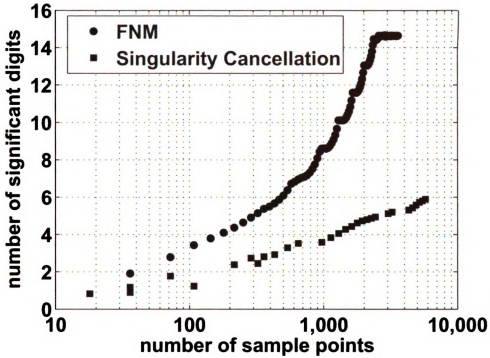

Figure 5.7. The number of significant digits achieved in calculations of the potential of the prism shown in Figure 5.4 plotted as a function of the number of sample points evaluated over a 3D grid. The results show that the FNM is accurate to a large number of significant digits than the singularity cancellation method for the same number of sample points.

excited 1D FNM expression for the volume integral and the singularity cancellation method on the 3D computational grid. For this computational grid, the uniformly excited 1D FNM expression for the volume integral uses 3, 5, 7.2, 9.33 times fewer sample points less than the singularity cancellation method for results accurate to 2, 3, 4, and 5 significant digits, respectively.

Table 5.6. Simulation parameters that achieve between 2 and 5 significant digits with the uniformly excited 1D FNM expression for the volume integral and the singularity cancellation method for the potential evaluated on a 3D grid. Parameters listed include the number of sample points for each observation point and the number of sample points required to achieve a specified error relative to the uniformly excited 1D FNM expression for the volume integral. (a) Significant digits 2 and 3. (b) Significant digits 4 and 5.

(a)

Significant digits	2		3	
	FNM	Singularity cancellation	FNM	Singularity cancellation
Sample points	72	216	108	540
Sample points relative to the FNM	1×	3×	1×	5×

(b)

Significant digits	4		5	
	FNM	Singularity cancellation	FNM	Singularity cancellation
Sample points	180	1296	324	3024
Sample points relative to the FNM	1×	7.2×	1×	9.33×

5.3 Discussion

5.3.1 Other geometries

The potential integral in Eq. (5.1) is a triple integral, and the uniformly excited 1D FNM expression for the volume integral reduces this integral to a single integral when the excitation is uniform. The single integral needs far fewer sample points to converge than the triple integral that is evaluated for the singularity cancellation method. Thus, the uniformly excited 1D FNM expression for the volume integral is an ideal method for calculating the reference potential. The fast approach demonstrated here can be easily extended to any volume source with polygonal faces. The potential integrals over those domains are the sum of the contributions from each side of the polygonal sources or each face of the volume sources. As seen in Eq. (5.4), the number

of terms required for a triangular source is 3 and for a rectangular source is 4.

5.3.2 Sample point calculations

Both the singularity cancellation method and the uniformly excited 1D FNM expression for the volume integral subdivide the prism into five subdomains including two subtetrahedrons and three subpyramids. Both methods evaluate three integrals for each subtetrahedron and four integrals for each subpyramids. In sum, both methods evaluate 18 integrals at each point for the prism shown in Figure 5.4. Each integral in the singularity cancellation method is calculated with the same number of sample points. If n_x, n_y, and n_z denote the number of Gauss abscissas used for each integral in the singularity cancellation method, then the number of sample points used for each integral is $n_s = n_x n_y n_z$. Thus, the total number of sample points for the singularity cancellation method is $18n_s$. For the uniformly excited 1D FNM expression for the volume integral, each integral is a single integral, and the lower and upper limits are given by l_{bi1} and l_{bi2} in Eq. (5.10). In each calculation, the integral is further subdivided into the summation of two integrals if l_{bi1} and l_{bi2} have opposite signs, where the limits of the subintegrals are from 0 to l_{bi2} and from l_{bi1} to 0. When l_{bi1} and l_{bi2} have the same sign, no subdivisions are needed. Thus, if the number of abscissas for each integral in the uniformly excited 1D FNM expression for the volume integral is n, then the total number of sample points for the uniformly excited 1D FNM expression for the volume integral calculations performed at a point due to a prism volume source is between $18n$ and $36n$. Thus, the FNM calculations is $O(n)$, and the singularity cancellation method is $O(n^3)$ for calculations at a single point.

5.3.3 Future work

The FNM algorithm is capable of calculating the uniformly excited potential integral. However, the FNM formulas have not yet been derived for non-uniform potential

sources. This difficulty can in part addressed by applying the polynomial apodization from Chapter 4 to the potential integrals. Thus, certain apodized potential integrals can be solved. Meanwhile, a large variety of functions can be approximated very well using polynomials.

5.4 Conclusion

A fast 1D integral for calculating uniformly excited 3D potential integrals is derived and evaluated. The 1D integral is based on the FNM expressions that were derived for acoustic radiation problems [8, 12]. The FNM subdivides the prism volume source into five subdomains, and on each subdomain, the FNM eliminates the singularities and reduces each triple integral into a single integral. The FNM expressions can be extended to different volume sources which consist of polygons on each face. The results are compared at single points and on a large three-dimensional grid. For the six observation points evaluated here, the FNM reduces the number of sample points by a factor of 5 to 27 relative to the singularity cancellation method, where the number of significant digits ranges in each result from 2 to 5. The FNM reduces the number of sample points by a factor of 3 to 9.33 relative to the singularity cancellation method when evaluated on a 3D grid and the result is accurate between 2 and 5 significant digits. Thus, the FNM is an ideal method for calculating uniformly excited potential integrals.

CHAPTER 6

A Fast Nearfield Method for Numerical Evaluation of Surface Integrals with Polynomial Apodization

Numerical calculation of surface integrals involved in integral equations are very important in scattering problems. Polynomial functions which are popularly used to approximate the electric and magnetic currents. For example, the most common used Rao-Wilton-Glisson basis function is also a linear basis function [24]. Potential integrals over a surface domain are often singular and direct evaluation of potential integrals may encounter numerical difficulties. Singularity subtraction methods [23, 25, 26, 27, 28] or singularity cancellation methods [30, 31, 32, 33] are often used to acheive better performance. Typically, those methods don't diminish the number of integraion of the potential integrals but manipulate the integrands to eliminate singularities instead. This approach is reasonable for general surface integrals, however, more efficient expressions can be acheived when polynomial apodized surface integrals

are considered. By ultilizing the fast nearfield method (FNM) [8, 12] for planar source that is uniformly exicited, which is proved to achieve much better accuacy than the Rayleigh-Sommerfeld integral, the 1D FNM expressions for the surface integrals with polynomial apodization is obtained.

To improve the numerical performance of surface integral calculations with the polynomial apodization, a single integral FNM expression is derived based on the FNM expressions for a planar source that is uniformly excited. The FNM expressions for planar sources with linear, quadratic, and cubic apodization functions are is obtained by utilizing the two derivatives. After the 1D FNM integrals are obtained, the 1D FNM integrals and the Rayleigh-Sommerfeld integral are both evaluated on a 2D grid. The results indicate that the 1D FNM expressions requires fewer abscissas than the Rayleigh-Sommerfeld integral to achieves a given accuracy.

6.1 Method

The potential generated by a planar source that is uniformly excited is given by

$$\Phi(x,y,z) = \iint_s \frac{e^{-jkR}}{4\pi R} ds \tag{6.1}$$

where $R = \sqrt{(x'-x)^2 + (y'-y)^2 + (z-z')^2}$ is the distance between the observation point (x,y,z) and the point (x',y',z') on the piston face and s is the area of the planar source. The potential in Eq. (6.1) is normalized with respect to $-v_0 e^{jwt}$, where v_0 is the constant normal particle velocity evaluated on the source of the planar source, ω is the excitation frequency in radians per second. Two derivatives can be evaluated with respect to R,

$$\frac{\partial R}{\partial x'} = \frac{(x'-x)}{R} \text{ and } \frac{\partial R}{\partial y'} = \frac{(y'-y)}{R}. \tag{6.2}$$

Thus the following two equations are easily obtained,

$$\frac{(x'-x)e^{-jkR}}{R} = \frac{j}{k}\frac{\partial e^{-jkR}}{\partial x'} \quad \text{and} \quad \frac{(y'-y)e^{-jkR}}{R} = \frac{j}{k}\frac{\partial e^{-jkR}}{\partial y'}. \tag{6.3}$$

The potential in Eq. (6.1) is rewritten as

$$\Phi(x,y,z) = \iint_s \frac{e^{-jkR}}{4\pi R} ds = \int_0^b \int_{L_1(y')}^{L_2(y')} \frac{e^{-jkR}}{4\pi R} dx'dy' \tag{6.4}$$

where b is the height of the triangular or the rectangular source, $L_2(y') = \frac{-B_2y'-C_2}{A_2}$ and $L_1(y') = \frac{-B_1y'-C_1}{A_1}$ for a triangle which is formed by the three lines $y = 0$, $A_1x + B_1y + C_1 = 0$ and $A_2x + B_2y + C_2 = 0$, and $L_2(y') = a$ and $L_1(y') = 0$ for a rectangle that has width a and height b.

6.1.1 Uniformly excited source

The FNM for the uniformly excited planar source is equivalent to the Rayleigh-Sommerfeld integral given by the following expression,

$$FNM = \iint_s \frac{e^{-jkR}}{4\pi R} ds$$

$$= \frac{j}{4\pi k}\left(\sum_{i=1}^{N} S_i l_i \int_{\frac{a_i^2-b_i^2-c_i^2}{2c_i}}^{\frac{a_i^2+c_i^2-b_i^2}{2c_i}} \frac{e^{-jk\sqrt{\sigma^2+z^2+l_i^2}} - e^{-jkz}}{\sigma^2+l_i^2} d\sigma\right), \tag{6.5}$$

where $S_i l_i = (E_i x + F_i y + G_i)/\sqrt{E_i^2 + F_i^2}$ combines the sign and the height terms within a single expression, $N = 3$ for the triangular source and $N = 4$ for the rectangular source. Calculations with Eq. 6.5 compute the values of c_i, E_i, F_i, and G_i only once for each edge of the planar source, whereas the values of a_i and b_i are calculated once for each (x, y) pair. Unlike the expressions for the impulse response that change depending on the spatial coordinate, Eq. 6.5 is a general formula that computes the nearfield pressure generated by any triangular source. The distance R

is given by $R = \sqrt{(x'-x)^2 + (y'-y)^2 + z^2}$, where $(x', y', 0)$ and (x, y, z) represent the source point and the observation point, respectively. In the following derivation of surface integrals with polynomial apodization, the following FNM expression is also needed.

$$FNM2 = \iint_s \frac{e^{-jkR}}{4\pi} ds = \frac{1}{4\pi k^2} \sum_{i=1}^{N} S_i l_i \int_{\frac{a_i^2 - b_i^2 - c_i^2}{2c_i}}^{\frac{a_i^2 + c_i^2 - b_i^2}{2c_i}} \times$$

$$\frac{e^{-jk\sqrt{z^2+\sigma^2+l_i^2}} \left(jk\sqrt{z^2+\sigma^2+l_i^2}+1\right) - e^{-jkz}(jkz+1)}{\sigma^2 + l_i^2} d\sigma, \qquad (6.6)$$

where $N = 3$ for the triangular source and $N = 4$ for the rectangular source.

6.1.2 Linear apodization

Let $f(x)$ represent an apodization function defined in the x direction and $f(x') = x'$. First, $f(x') = x'$ is written as $x' = (x' - x) + x$. The potential for the linear apodized triangular source is the sum of the following two integrals,

$$\Phi_1(x', y', z') = \iint_s x' \frac{e^{-jkR}}{4\pi R} dx' dy'$$

$$= \iint_s (x' - x) \frac{e^{-jkR}}{4\pi R} dx dy + \iint_s x \frac{e^{-jkR}}{4\pi R} dx' dy'. \qquad (6.7)$$

The first of the two double integrals on the right hand side of Eq. (6.7) is reduced to a single integral by

$$\iint_s (x' - x) \frac{e^{-jkR}}{4\pi R} ds = \int_0^b \int_{L_1(y')}^{L_2(y')} (x' - x) \frac{e^{-jkR}}{4\pi R} dx' dy'$$

is given by $R=\sqrt{(x'-x)^2+(y'-y)^2+z^2}$, where $(x',y',0)$ and (x,y,z) represent the source point and the observation point, respectively. In the following derivation of surface integrals with polynomial apodization, the following FNM expression is also needed.

$$FNM2=\iint_s \frac{e^{-jkR}}{4\pi}ds=\frac{1}{4\pi k^2}\sum_{i=1}^{N} S_i l_i \int_{\frac{a_i^2-b_i^2-c_i^2}{2c_i}}^{\frac{a_i^2+c_i^2-b_i^2}{2c_i}} \times$$

$$\frac{e^{-jk\sqrt{z^2+\sigma^2+l_i^2}}\left(jk\sqrt{z^2+\sigma^2+l_i^2}+1\right)-e^{-jkz}\left(jkz+1\right)}{\sigma^2+l_i^2}d\sigma, \qquad (6.6)$$

where $N=3$ for the triangular source and $N=4$ for the rectangular source.

6.1.2 Linear apodization

Let $f(x)$ represent an apodization function defined in the x direction and $f(x')=x'$. First, $f(x')=x'$ is written as $x'=(x'-x)+x$. The potential for the linear apodized triangular source is the sum of the following two integrals,

$$\Phi_1(x',y',z')=\iint_s x'\frac{e^{-jkR}}{4\pi R}dx'dy'$$

$$=\iint_s (x'-x)\frac{e^{-jkR}}{4\pi R}dxdy+\iint_s x\frac{e^{-jkR}}{4\pi R}dx'dy'. \qquad (6.7)$$

The first of the two double integrals on the right hand side of Eq. (6.7) is reduced to a single integral by

$$\iint_s (x'-x)\frac{e^{-jkR}}{4\pi R}ds=\int_0^b \int_{L_1(y')}^{L_2(y')} (x'-x)\frac{e^{-jkR}}{4\pi R}dx'dy'$$

$$= \frac{j}{4\pi k} \int_0^b \int_{L_1(y')}^{L_2(y')} \frac{\partial e^{-jkR}}{\partial x'} dx'dy' = \frac{j}{4\pi k} \int_0^{+b} e^{-jkR}|_{x'=L_1(y')}^{x'=L_2(y')} dy'$$

$$= \frac{j}{4\pi k} \int_0^{+b} (e^{-jk\sqrt{(L_2(y')-x)^2+(y'-y)^2+z^2}} - e^{-jk\sqrt{(L_1(y')-x)^2+(y'-y)^2+z^2}}) dy. \tag{6.8}$$

Denote $M_1(u) = \frac{j}{k} \int_0^{+b} ue^{-jkR}|_{x'=L_1(y')}^{x'=L_2(y')} dy'$, thus

$$\iint_s (x'-x)\frac{e^{-jkR}}{R} ds = M_1(1). \tag{6.9}$$

The second of the two double integrals on the right hand side of Eq. (6.7) is also reduced to a single integral easily by

$$\iint_s x\frac{e^{-jkR}}{4\pi R} dS = xFNM \tag{6.10}$$

Eqs. (6.9) and (6.10) are added together and, the pressure for the linear apodized triangular source is given by

$$\Phi_1(x', y', z') = M_1(1) + xFNM. \tag{6.11}$$

6.1.3 Quadratic apodization

Let $f(x)$ represent a quadratic apodization function defined in the x direction and $f(x') = x'^2$. First, $f(x') = (x')^2$ is written as $(x')^2 = x'(x'-x) + xx'$. The pressure for the quadratic apodized triangular source is the sum of the following two integrals,

$$\Phi_2(x', y', z') = \iint_s (x')^2 \frac{e^{-jkR}}{4\pi R} dx'dy'$$

$$= \iint_s x'(x'-x)\frac{e^{-jkR}}{4\pi R} dx'dy' + \iint_s xx'\frac{e^{-jkR}}{4\pi R} dx'dy'. \tag{6.12}$$

The first double integral on the right hand side of Eq. (6.12) is reduced to a single integral by

$$\int_0^b \int_{L_1(y')}^{L_2(y')} x'(x'-x)\frac{e^{-jkR}}{4\pi R}dx'dy' = \frac{j}{4\pi k}\int_0^b \int_{L_1(y')}^{L_2(y')} x'\frac{\partial e^{-jkR}}{\partial x'}dx'dy'$$

$$= \frac{j}{4\pi k}\int_0^{+b} x'e^{-jkR}\Big|_{x'=L_1(y')}^{x'=L_2(y')}dy' - \frac{j}{4\pi k}\int_0^b \int_{L_1(y')}^{L_2(y')} e^{-jkR}dx'dy' \qquad (6.13)$$

Denote $M_2(u) = \frac{j}{4\pi k}\int_0^b \int_{L_1(y')}^{L_2(y')} ue^{-jkR}dx'dy'$, thus

$$\int_0^b \int_{L_1(y')}^{L_2(y')} x'(x'-x)\frac{e^{-jkR}}{4\pi R}dx'dy' = M_1(x') - M_2(1) = M_1(x') - FNM2. \qquad (6.14)$$

The second of the two double integrals on the right hand side of Eq. (6.12) is reduced to a single integral by applying the the result from Eq. (6.11)

$$\int_0^b \int_{L_1(y')}^{L_2(y')} xx'\frac{e^{-jkR}}{4\pi R}dx'dy' = xM_1(1) + x^2FNM. \qquad (6.15)$$

Eqs. (6.14) and (6.15) are added together, and the pressure for the quadratic apodized triangular source is given by

$$\Phi_2(x', y', z') = M_1(x') - FNM2 + xM_1(1) + x^2FNM. \qquad (6.16)$$

6.1.4 Cubic apodization

Let $f(x)$ represent an cubic apodization function defined in the x direction and $f(x') = (x')^3$. First, $f(x') = (x')^3$ is written as $(x')^3 = x'^2(x'-x) + x(x')^2$.

The pressure for the cubic apodized triangular source is the sum of the following two integrals,

$$\Phi_3(x',y',z') = \int\int_s (x')^3 \frac{e^{-jkR}}{4\pi R} ds$$

$$= \int_0^b \int_{L_1(y')}^{L_2(y')} (x')^2(x'-x)\frac{e^{-jkR}}{4\pi R}dx'dy' + x\int_0^b \int_{L_1(y')}^{L_2(y')} (x')^2 \frac{e^{-jkR}}{4\pi R}dx'dy'. \quad (6.17)$$

The first double integral on the right hand side of Eq. (6.17) is denoted as

$$\int_0^b \int_{L_1(y')}^{L_2(y')} (x')^2(x'-x)\frac{e^{-jkR}}{4\pi R}dx'dy'$$

$$= \frac{j}{4\pi k}\int_0^{+b}\left[(x')^2 e^{-jkR}\Big|_{x'=L_1(y')}^{x'=L_2(y')} - \int_{L_1(y')}^{L_2(y')} 2x'e^{-jkR}dx'\right]dy'$$

$$= M_1(x'^2) - 2M_2(x') \quad (6.18)$$

where $M_2(x') = \frac{j}{4\pi k}\int_0^b \int_{L_1(y')}^{L_2(y')} x'e^{-jkR}dx'dy'$ and is rewritten as

$$M_2(x') = \frac{j}{4\pi k}\int_0^b \int_{L_1(y')}^{L_2(y')} (x'-x)e^{-jkR}dx'dy' + \frac{j}{4\pi k}\int_0^b \int_{L_1(y')}^{L_2(y')} xe^{-jkR}dx'dy'$$

$$= \frac{j}{k}(M_1(R) - \frac{j}{k}M_1(1)) + xM_2(1). \quad (6.19)$$

The second double integral on the right hand side of Eq. (6.17) is also reduced to a single integral by

$$x\int_0^b\int_{L_1(y')}^{L_2(y')} x'^2\frac{e^{-jkR}}{4\pi R}dx'dy' = x(M_1(x') - M_2(1) + xM_1(1) + x^2FNM) \quad (6.20)$$

Combining Eqs. (6.18), (6.20) and (6.19), the pressure for the cubic apodized triangular source is represented by

$$\Phi_3(x', y', z') = M_1(x^2)$$

$$-\frac{2}{k}(jM_1(R) - 3xM_2(1) + xM_1(x) + (x^2 - \frac{2}{k^2})M_1(1) + x^3FNM). \quad (6.21)$$

6.1.5 Error calculations

The numerical error $\eta(x,\ y,\ z;\ k)$ is defined as the normalized difference between the reference potential $\Phi_{ref}(x, y, z; k)$ and the computed potential $\Phi(x, y, z; k)$ according to

$$\eta(x, y, z;\ k) = \frac{|\Phi(x, y, z;\ k) - \Phi_{ref}(x, y, z;\ k)|}{max|\Phi_{ref}(x, y, z;\ k)|}. \quad (6.22)$$

The maximum error η_{max} is defined as

$$\eta_{max} = \max_{x,y,z} \eta(x,\ y,\ z). \quad (6.23)$$

6.2 Results

The results are evaluated for a triangular source located in the $z = 0$ plane, where the positions of the three peaks are $(0, 4\lambda, 0)$, $(-2\lambda, 0, 0)$ and $(2\lambda, 0, 0)$. The reference potential is computed for the linear, quadratic, and cubic apodization functions

Table 6.1. Simulation parameters that achieve 10%, 1% and 0.1% peak normalized error in the potential obtained with the fast nearfield method and the Rayleigh-Sommerfeld integral computed using linear apodization for a triangular source. Parameters listed include the number of Gauss abscissas, the computation time, and the ratios of the computation times relative to the times obtained with the fast nearfield method.

	Linear Apodization					
	10%		1%		0.1%	
	FNM	Rayleigh	FNM	Rayleigh	FNM	Rayleigh
Abscissas	12	42×42	14	99×99	15	190×180
Time	0.14s	1.39s	0.16s	7.71s	0.17s	25.47s
Computation Time relative to the FNM	1×	9.97×	1×	46.85×	1×	145.82×

$f(x)$ described in the Section 6.1, namely $f(x) = x$, $f(x) = x^2$, and $f(x) = x^3$, respectively. The potential is evaluated in the $x = 1.0\lambda$ plane, where the grid in the $x = 1.0\lambda$ plane extends from -2λ to 6λ in the y direction, and the grid spacing in the y-direction is 0.08λ. The grid extends from 0.02λ to 1.0λ in the z direction with a spacing of 0.02λ. The potential in the z direction is shifted by 0.02λ relative to the piston source in the $z = 0$ plane for both the Rayleigh-Sommerfeld integral and the fast nearfield method in order to avoid the most severe singularities in this location for the Rayleigh-Sommerfeld integral. The reference potential is obtained using the Rayleigh-Sommerfeld integral evaluated with 100,000 Gauss abscissas in each direction, and the results are computed on a 50×101 spatial grid.

6.2.1 Linear apodization

The linear apodization function evaluated here is $f(x) = x$. The results for the fast nearfield method and the Rayleigh-Sommerfeld integral are plotted in Figures 6.1 and 6.2. The numerical errors and the computation times are plotted in Figure 6.1 a)

Table 6.2. Simulation parameters that achieve 10%, 1%, and 0.1% peak normalized error in the potential obtained with the fast nearfield nearfield method and the Rayleigh-Sommerfeld integral computed using quadratic apodization for a triangular source. Parameters listed include the number of Gauss abscissas, the computation time, and the ratios of the computation times relative to the times obtained with the fast nearfield method.

	Quadratic Apodization					
	10%		1%		0.1%	
	FNM	Rayleigh	FNM	Rayleigh	FNM	Rayleigh
Abscissas	12	33×33	14	94×94	15	190×180
Time	0.17s	0.88s	0.22s	7.40s	0.21s	25.96s
Computation time relative to the FNM	1×	5.25×	1×	34.01×	1×	123.18×

and Figure 6.1 b), respectively as a function of the number Gauss abscissas used in one integration direction for the fast nearfield method and the Rayleigh-Sommerfeld method. The time vs. error comparison is also plotted in Figure 6.2. Figures 6.1 and 6.2 show that the fast method converges much faster than the Rayleigh-Sommerfeld integral for the linear apodization function evaluated here. For 10% peak normalized error, the fast nearfield method is 9.97 times faster than Rayleigh-Sommerfeld integral. For 1% peak normalized error, the fast nearfield method is 46.85 times faster than Rayleigh-Sommerfeld integral. For 0.1% peak normalized error, the fast nearfield method is 145.82 times faster than Rayleigh-Sommerfeld integral.

6.2.2 Quadratic apodization

The quadratic apodization function evaluated here is $f(x) = x^2$. The results for the fast nearfield method and the Rayleigh-Sommerfeld integral are plotted in Figures 6.3 and 6.4. The numerical errors and the computation times are plotted in Figure 6.3 a) and Figure 6.3 b), respectively, as a function of the number Gauss abscissas

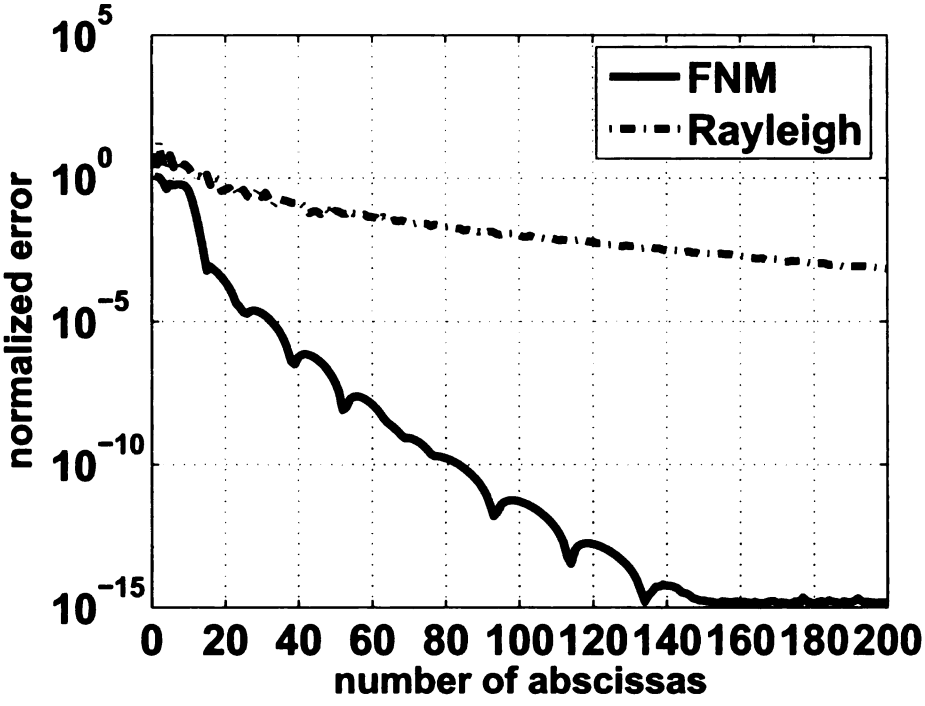

a) Maximum errors for linear apodization.

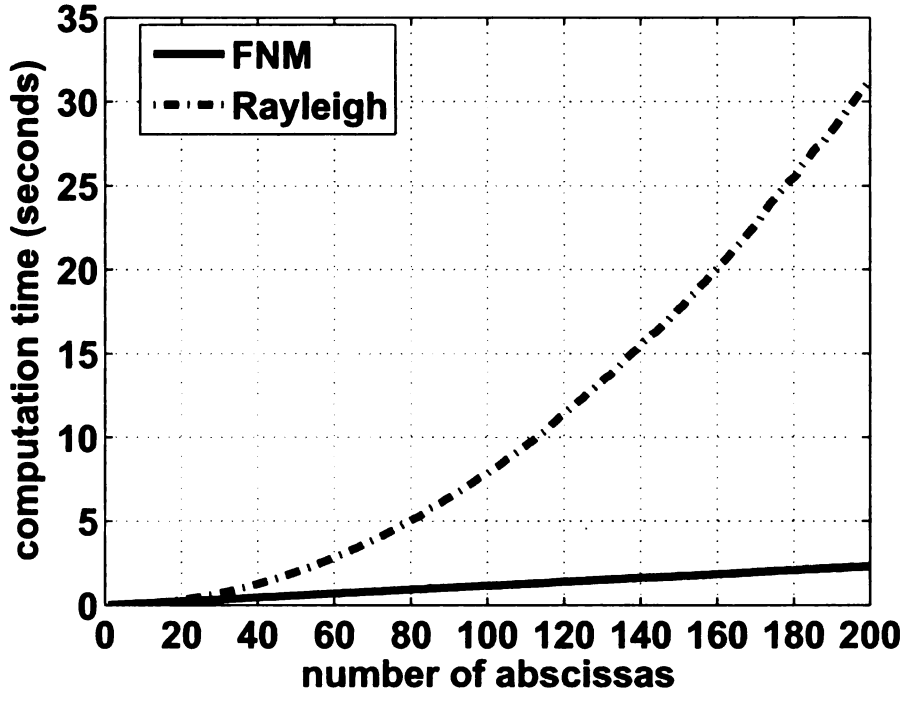

b) Computation times for linear apodization.

Figure 6.1. a) Maximum errors and b) computation times obtained with the fast nearfield method and the Rayleigh-Sommerfeld integral for a triangular source with linear apodization.

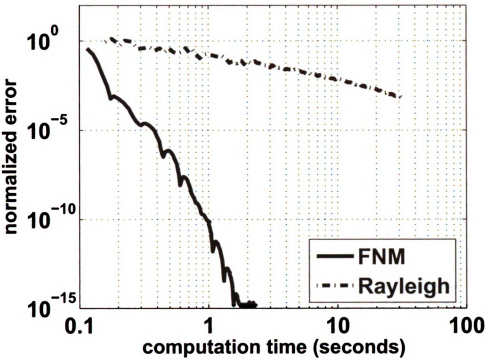

Figure 6.2. Numerical errors plotted as a function of the computation time for a triangular source with linear apodization. The results show that the fast nearfield method achieves much better convergence performance than the Rayleigh-Sommerfeld integral.

used in one integration direction for the fast method and the Rayleigh-Sommerfeld integral. The time vs. error comparison is also plotted in Figure 6.4. Figures 6.3 and 6.4 show that the fast nearfield method converges much faster than the Rayleigh-Sommerfeld integral for the quadratic apodization function evaluated here. For 10% peak normalized error, the fast nearfied method is 5.25 times faster than Rayleigh-Sommerfeld integral. For 1% peak normalized error, the fast nearfield method is 34.01 times faster than Rayleigh-Sommerfeld integral. For 0.1% peak normalized error, the fast nearfield method is 123.18 times faster than Rayleigh-Sommerfeld integral.

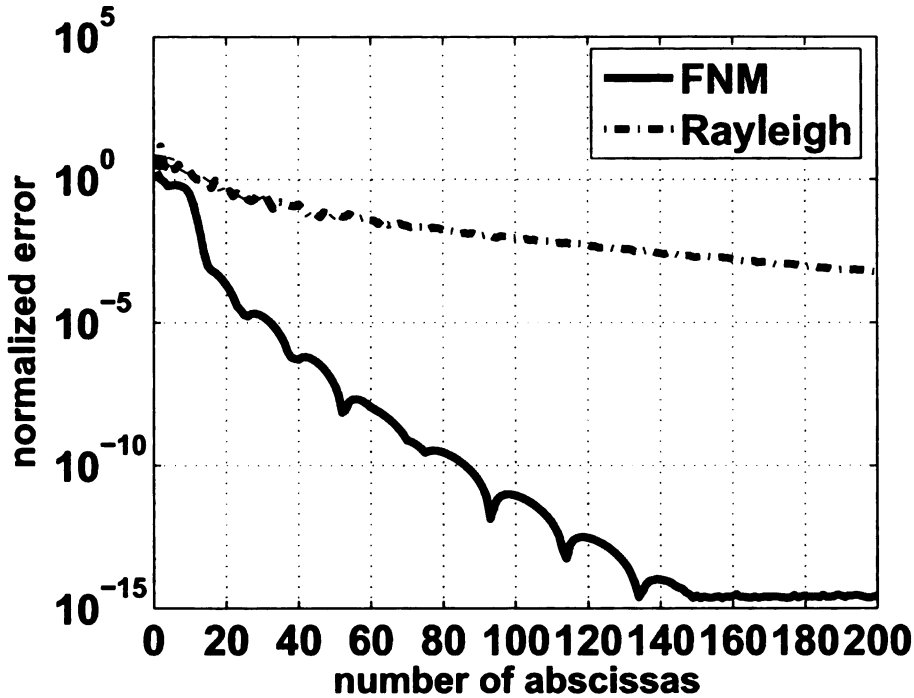

a) Maximum errors for quadratic apodization.

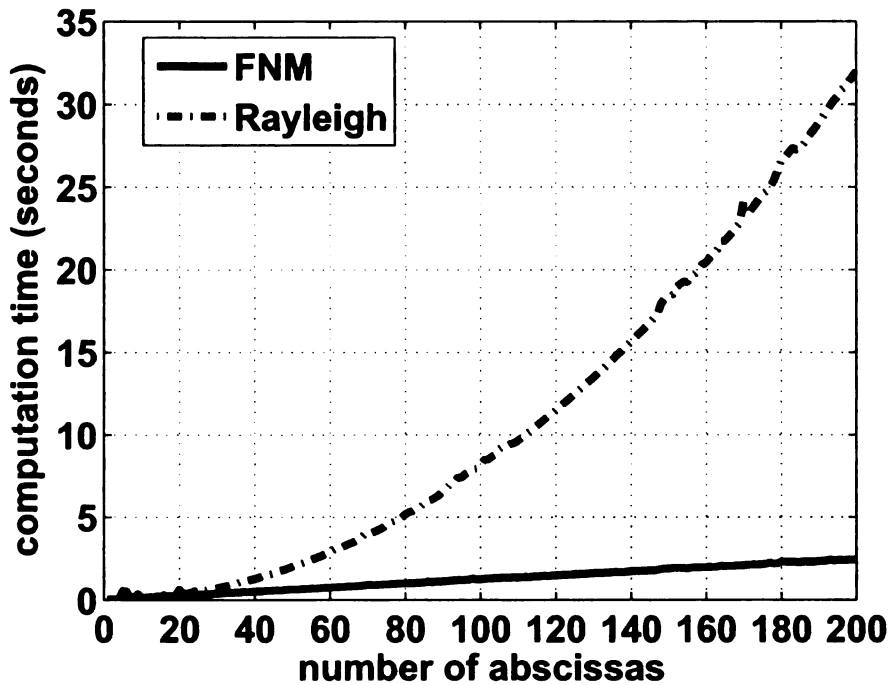

b) Computation times for the quadratic apodization.

Figure 6.3. a) Maximum errors and b) computation times obtained with the fast nearfield method and the Rayleigh-Sommerfeld integral for a triangular source with quadratic apodization.

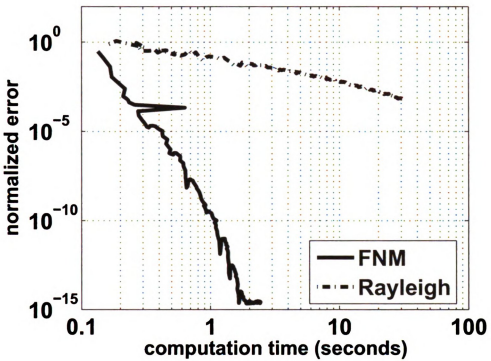

Figure 6.4. Numerical errors plotted as a function of the computation time for a triangular source with quadratic apodization. The results show that the fast nearfield method achieves much better convergence than the Rayleigh-Sommerfeld integral.

6.2.3 Cubic apodization

The cubic apodization function evaluated here is $f(x) = x^3$. The results for the fast nearfield method and the Rayleigh-Sommerfeld integral are plotted in Figures 6.5 and 6.6. The numerical errors and the computation times are plotted in Figure 6.5 a) and Figure 6.5 b), respectively, as a function of the number Gauss abscissas used in one integration direction for the fast nearfield method and the Rayleigh-Sommerfeld integral. The time vs. error comparison is also plotted in Figure 6.6. Figures 6.5 and 6.6 show that the fast nearfield method converges much faster than the Rayleigh-Sommerfeld integral for cubic apodization function evaluataed here. For 10% peak normalized error, the fast nearfield method is 5.22 times

Table 6.3. Simulation parameters that achieve 10%, 1% and 0.1% peak normalized error in the potential obtained with the fast nearfield method and the Rayleigh-Sommerfeld integral computed using cubic apodization for a triangular source. Parameters listed include the number of Gauss abscissas, the computation time, and the ratios of the computation times relative to the times obtained with the fast nearfield method.

	Cubic Apodization					
	10%		1%		0.1%	
	FNM	Rayleigh	FNM	Rayleigh	FNM	Rayleigh
Abscissas	12	33×33	13	89×89	15	190×180
Time	0.40s	2.07s	0.43s	14.94s	0.50s	55.25s
Computation time relative to the FNM	1×	5.22×	1×	34.76×	1×	111.28×

faster than Rayleigh-Sommerfeld integral. For 1% peak normalized error, the fast nearfield method is 34.76 times faster than Rayleigh-Sommerfeld integral. For 0.1% peak normalized error, the fast nearfield method is 111.28 times faster than Rayleigh-Sommerfeld integral.

6.3 Discussions

6.3.1 Other Polygonal Sources

The fast nearfield method for poynomial apodized triangular source and rectangular source are derived in this paper. The derivation process can be generalized to other polygonal sources. The FNM for the uniformly excited polygonal source is readily computed using Eq. (6.5) and Eq. (6.6), and the number of 1D integrals evaluated is equal to the number of sides of the polygonal source. The computation of Eq. (??) also needs to be adapted according to the specific polygonal source.

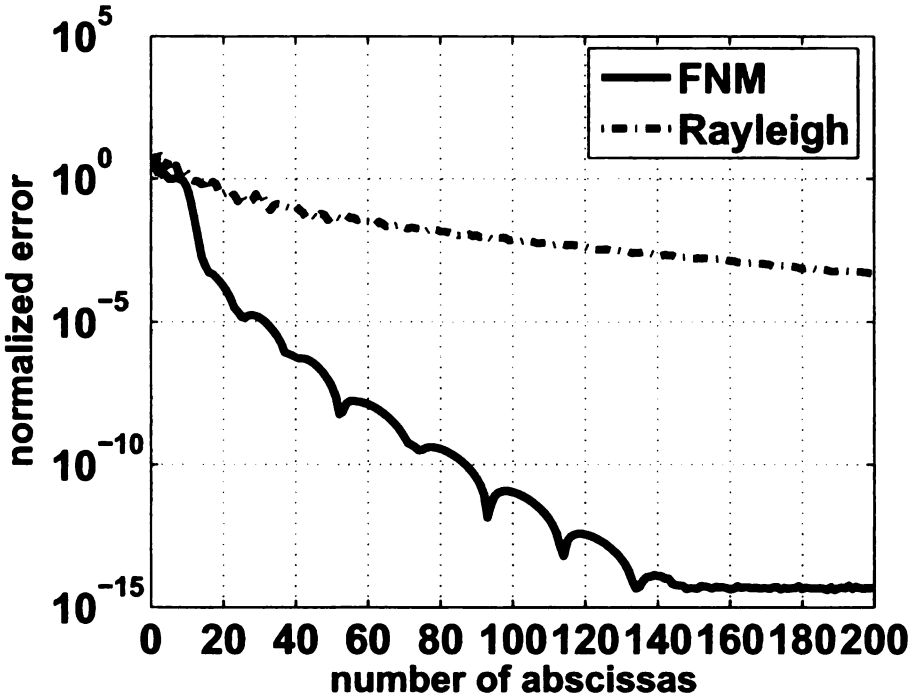

a) Maximum errors for cubic apodization.

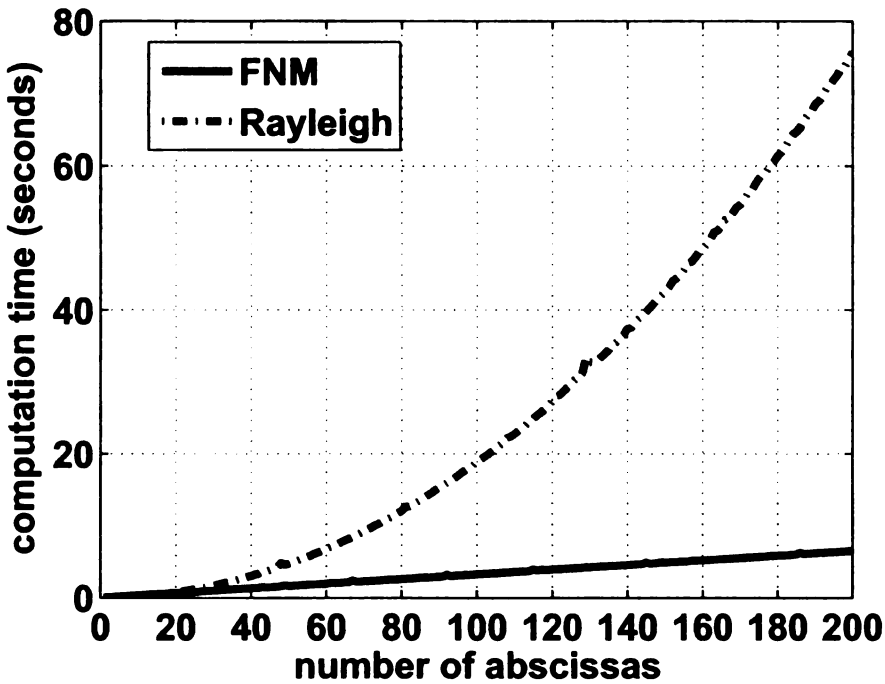

b) Computation times for cubic apodization.

Figure 6.5. a) Maximum errors and b) computation times obtained with the fast nearfield method and the Rayleigh-Sommerfeld integral for a triangular source with cubic apodization.

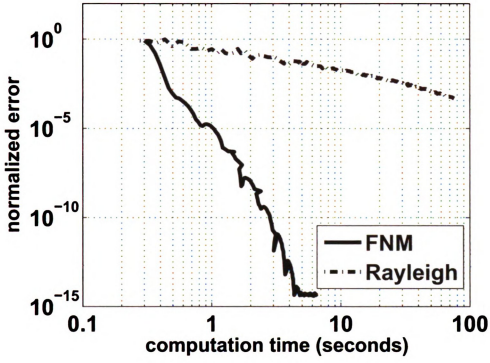

Figure 6.6. Numerical errors plotted as a function of the computation time for a triangular source with cubic apodization. The results show that the fast method achieves much better convergence performance than the Rayleigh-Sommerfeld integral.

6.3.2 Higher order polynomials

In this paper, the FNM expressions for surface potential integrals with linear, quadratic, and cubic polynomial apodization are derived. The FNM expressions of the surface potential integrals with higher order polynomial apodization can be derived using the same strategy. Many apodization functions, like sin(), cos(), exp(), etc., can be approximated using higher order polynomials, thus potential integrals with such apodizations can be approximated with higher order polynomials combined with appropriate 1D FNM expressions. Since the FNM expressions converge very rapidly, the accuracy of numerical evaluation of the potential integrals with general apodization is mainly dependent on the accuracy of the approximation to the apodization

function.

6.4 Conclusion

Single integral expressions for calculating the potential generated by polynomial apodized planar sources are derived and evaluated. Starting from the FNM for the uniformly excited planar source, three polynomial apodizations including linear, quadratic, and cubic apodizations are reduced to a 1D integral. Higher order polynomials can be obtained using the same strategy. These fast expressions remove the singularities that appear in the Rayleigh-Sommerfeld integral and thus achieve very fast convergence with a very small number of Gauss abscissas. Simulation results are compared between the fast nearfield method and the Rayleigh-Sommerfeld integral. For a given peak normalized error, the fast nearfield method always converges much faster than the Rayleigh-Sommerfeld integral when polynomial apodization is evaluated with the appropriate 1D FNM expression.

CHAPTER 7

A Fast Nearfield Method for Numerical Evaluation of Volume Integrals with Polynomial Apodization

Numerical calculation of volume potential integrals involved in integral equations are of great importance in scattering problems and the polynomial function is a very popular function to approximate the electric and magnetic currents. For examples, three-dimensional polynomials are adopted to approximate the entire-domain normalized current density by Moraros and Popovic [23] when applied to optimize the volume potential integrals involved in the moment-method analysis of 3D dielectric scatters. Potential integrals over a volume domain are often singular and direct evaluation of potential integrals may encounter numerical difficulties. Often, Singularity subtraction methods [23, 25, 26, 27, 28] or singularity cancellation methods [30, 31, 32, 33] are used to improve the accuracy of the potential integrals. Those methods retain the same number of dimensions over which the integration is performed. This approach

is reasonable for general potential integrals, however, more efficient expressions can be acheived when polynomial apodized volume potential integrals are considered.

Potentials generated by uniformly excited planar sources are computed with both the Rayleigh-Sommerfeld integral [6] and the fast nearfield method (FNM) [8, 12]. The existing FNM achieves much higher accuracies by eliminating the $1/R$ singularity from the Rayleigh-Sommerfeld integral and by decreasing a 2D integral to a 1D integral. Numerical evaluation of potential integrals with polynomial apodization is an important problem for scattering calculations, which motivates the derivatiaon of a similar fast nearfield method to improve the numerical performance of those integrals.

A single FNM integral is derived based on the FNM expressions for uniformly excited and polynomial apodized polygonal sources in order to improve the performance of potential integral calculations for volume sources with polynomial apodization. The FNM expressions for uniformly excited sources are first reviewed, and then the FNM expressions for the polynomial apodized planar source are obtained. The volume source is then subdivided into five subdomains, and local coordinate system is defined for calculations of the potential for a subdomain. The potential generated by the entire volume source is the superposition of the potentials evaluated over each subdomain, where each contribution is represented by a single integral. Thus, 1D FNM expressions for a polynomial apodized volume source is obtained. The 1D FNM expressions and the singularity cancellation method are evaluated on a 3D grid. The results indicate that the FNM requires less time to achieve a given accuracy than the singularity cancellation method for a polynomial apodized volume source.

7.1 Method

The volume integrals evaluated in this article are given by

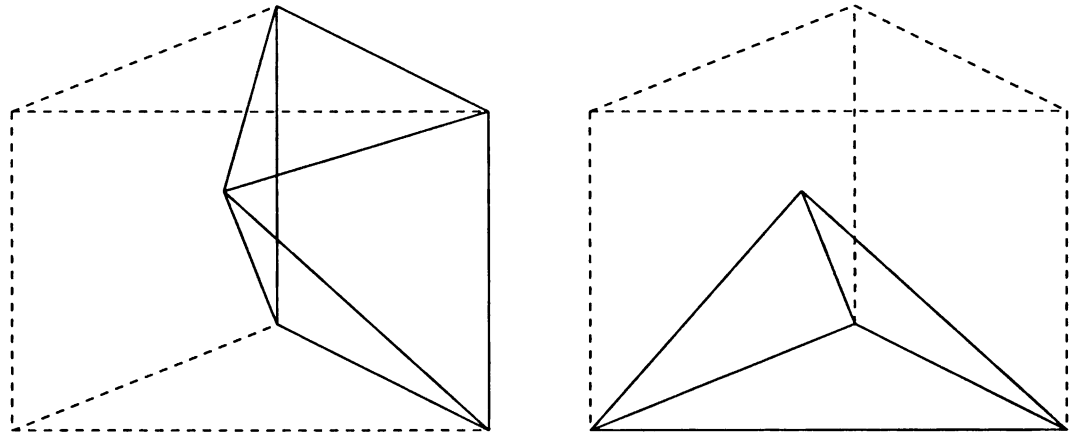

a) Subpyramid. b) Subtetrahedron.

Figure 7.1. Subdomains defined for a prism where the shared vertex is defined at the observation point.

$$\Phi(x,y,z) = \iiint_V \Lambda(r')\frac{e^{-jkR}}{4\pi R}dV, \tag{7.1}$$

where V is the volume integration domain, $\Lambda(r')$ represents the apodization over the integration domain, R is the distance between the observation point (x,y,z) and the source point (x',y',z'), and k is the wavenumber. The potential in Eq. (7.1) is normalized with respect to $-v_0 e^{jwt}$, where v_0 is the constant normal particle velocity evaluated on the volume source, ω is the excitation frequency in radians per second. Here, the special case $\Lambda(r') = x'$ is considered.

The volume is first subdivided about the observation point into subdomains. Figure (7.1) illustrates a subpyramid and a subtetrahedron for a prism.

The volume integral shown in Eq. (7.1) is first rewritten as

$$\Phi(x,y,z) = \iiint_V x'\frac{e^{-jkR}}{4\pi R}dV = \iiint_V \frac{(x'-x)e^{-jkR}}{4\pi R}dV + x\iiint_V \frac{e^{-jkR}}{4\pi R}dV. \tag{7.2}$$

Then, two derivatives are evaluated with respect to R,

$$\frac{\partial R}{\partial x'} = \frac{(x'-x)}{R} \text{ and } \frac{\partial R}{\partial y'} = \frac{(y'-y)}{R}. \tag{7.3}$$

The following equations are then obtained,

$$\frac{(x'-x)e^{-jkR}}{R} = \frac{j}{k}\frac{\partial e^{-jkR}}{\partial x'} \text{ and } \frac{(y'-y)e^{-jkR}}{R} = \frac{j}{k}\frac{\partial e^{-jkR}}{\partial y'}. \tag{7.4}$$

The potential integral in Eq. (6.1) for a triangular base is rewritten as

$$\Phi(x,y,z) = \iint_s \Lambda(r')\frac{e^{-jkR}}{4\pi R}ds = \int_0^{-C_1/B_1}\int_{L_1(y')}^{L_2(y')} \Lambda(r')\frac{e^{-jkR}}{4\pi R}dx'dy'$$

$$= \int_{-C_1/A_1}^{0}\int_0^{L_3(x')} \Lambda(r')\frac{e^{-jkR}}{4\pi R}dx'dy' + \int_0^{-C_2/A_2}\int_0^{L_4(x')} \Lambda(r')\frac{e^{-jkR}}{4\pi R}dx'dy', \tag{7.5}$$

where $L_1(y') = (-B_1y' - C_1)/A_1$, $L_2(y') = (-B_2y' - C_2)/A_2$, $L_3(x') = (-A_1x' - C_1)/B_1$ and $L_4(x') = (-A_2x' - C_2)/B_2$ for a triangular base which is formed by the three lines $y = 0$, $A_1x + B_1y + C_1 = 0$ and $A_2x + B_2y + C_2 = 0$. The potential integral in Eq. (6.1) for a rectangular base is rewritten as

$$\Phi(x,y,z) = \iint_s \Lambda(r')\frac{e^{-jkR}}{4\pi R}ds = \int_{-a}^{a}\int_{-b}^{b} \Lambda(r')\frac{e^{-jkR}}{4\pi R}dx'dy', \tag{7.6}$$

where the center of the rectangular source is the origin of the coordinate system, and the width and height of a rectangular source is $2a$, and $2b$, respectively.

7.1.1 Uniformly excited planar source

The FNM for a planar source that is uniformly excited is equivalent to the Rayleigh-Sommerfeld integral given by the following expression,

$$FNM = \iint_s \frac{e^{-jkR}}{4\pi R}ds$$

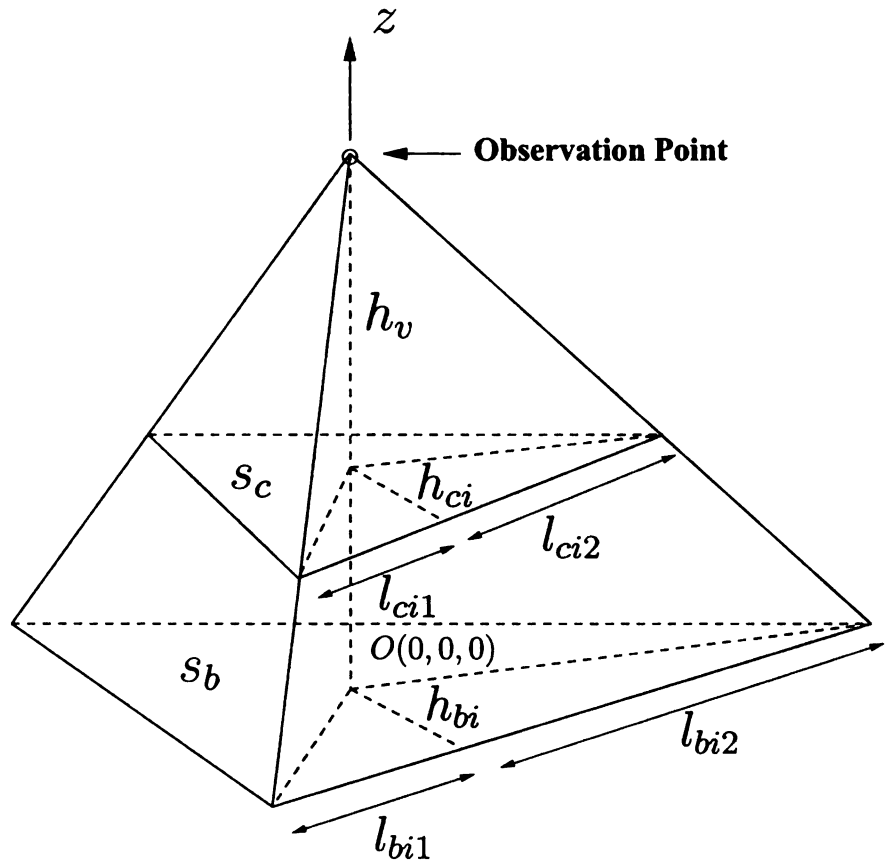

Figure 7.2. Geometric parameters defined for the potential calculations in a tetrahedral subdomain.

$$= \frac{j}{4\pi k}\left(\sum_{i=1}^{N} S_i l_i \int_{\frac{a_i^2-b_i^2-c_i^2}{2c_i}}^{\frac{a_i^2+c_i^2-b_i^2}{2c_i}} \frac{e^{-jk\sqrt{\sigma^2+z^2+l_i^2}} - e^{-jkz}}{\sigma^2+l_i^2} d\sigma\right), \qquad (7.7)$$

where $S_i l_i = (E_i x + F_i y + G_i)/\sqrt{E_i^2 + F_i^2}$ combines the sign and the height terms within a single expression. The number of 1D integrals is given by $N = 3$ for a triangular source and $N = 4$ for a rectangular source. Calculations with Eq. 7.7 compute the values of c_i, E_i, F_i, and G_i only once for each edge of the planr source, whereas the values of a_i and b_i are calculated once for each (x, y) pair.

The fast nearfield method expressions for the uniformly excited potential integrals derived previously for a prism, denote by Φ_u, are given by

$$\Phi_u = \iiint_V \frac{e^{-jkR}}{4\pi R} dV = \sum_{m=1}^{M} \frac{(A_m x + B_m y + C_m z + D_m)}{|A_m x + B_m y + C_m z + D_m|} \Phi_{um}, \tag{7.8}$$

where $M = 5$ is the number of faces that the volume has, $A_m x + B_m y + C_m z + D_m = 0$ denotes the general form of the plane that passes through each face of the prism, and Φ_{um} is the potential generated by each subdomain. The expressions for Φ_{um} are

$$\Phi_{um} = \frac{-1}{4\pi k^2} \sum_{i=1}^{N} h_{bi}$$

$$\times \int_{l_{bi1}}^{l_{bi2}} \frac{z(e^{-jk\sqrt{Q^2+z^2+h_{bi}^2}} - 1) - (e^{-jkz} - 1)\sqrt{Q^2 + z^2 + h_{bi}^2}}{(Q^2 + h_{bi}^2)\sqrt{Q^2 + z^2 + h_{bi}^2}} dQ, \tag{7.9}$$

for each subvolume, where $h_v = z$ is the distance from the observation point to the base of the subdomain, and the parameters h_{bi}, l_{bi1}, l_{bi2} are shown in Figure (7.2).

7.1.2 Linear apodization for a planar source

Linear apodization in the x direction

The potential integral for the apodization function $f(x', y', z') = x'$ applied to a planar source is given by

$$\iint_s x' \frac{e^{-jkR}}{4\pi R} dx'dy' = \iint_s (x' - x) \frac{e^{-jkR}}{4\pi R} dx'dy' + \iint_s x \frac{e^{-jkR}}{4\pi R} dx'dy'$$

$$= \frac{j}{4\pi k} \iint_s \frac{\partial e^{-jkR}}{\partial x'} dx'dy' + xFNM_{uniform}. \tag{7.10}$$

For a triangular source, substituting Eq. (7.5) into Eq. (7.10) yields

$$\iint_s x' \frac{e^{-jkR}}{4\pi R} dx'dy' = xFNM_{uniform} +$$

$$\frac{j}{4\pi k} \int_0^{-C_1/B_1} \left(e^{-jk\sqrt{(L_2(y')-x)^2+(y'-y)^2+(z-z')^2}} \right.$$

$$\left. -e^{-jk\sqrt{(L_1(y')-x)^2+(y'-y)^2+(z-z')^2}} \right) dy' \tag{7.11}$$

For a rectangular source, substituting Eq. (7.6) into Eq. (7.10) yields

$$\iint_s x' \frac{e^{-jkR}}{4\pi R} dx'dy' = xFNM_{uniform} + \frac{j}{4\pi k}$$

$$\times \int_{-b}^{b} (e^{-jk\sqrt{(a-x)^2+(y'-y)^2+(z-z')^2}} - e^{-jk\sqrt{(a+x)^2+(y'-y)^2+(z-z')^2}}) dy'. \tag{7.12}$$

Linear apodization in the y direction

The potential integral for the apodization function $f(x', y', z') = y'$ applied to a planar source is given by

$$\iint_s y' \frac{e^{-jkR}}{4\pi R} dx'dy' = \iint_s (y' - y) \frac{e^{-jkR}}{4\pi R} dx'dy' + \iint_s y \frac{e^{-jkR}}{4\pi R} dx'dy'$$

$$= \frac{j}{4\pi k} \iint_s \frac{\partial e^{-jkR}}{\partial y'} dx'dy' + yFNM_{uniform}. \tag{7.13}$$

For a triangular source, substituting Eq. (7.5) into Eq. (7.13) yields

$$\iint_s y' \frac{e^{-jkR}}{4\pi R} dx'dy' = yFNM_{uniform} + \frac{j}{4\pi k} \int_{-C_1/A_1}^{0}$$

$$\left(e^{-jk\sqrt{(x'-x)^2+(L_3(x')-y)^2+(z-z')^2}} - e^{-jk\sqrt{(x'-x)^2+y^2+(z-z')^2}} \right) dx'$$

$$+\frac{j}{4\pi k}\int_0^{-C_2/A_2} \left(e^{-jk\sqrt{(x'-x)^2+(L_4(x')-y)^2+(z-z')^2}} \right.$$

$$\left. -e^{-jk\sqrt{(x'-x)^2+y^2+(z-z')^2}} \right) dx'. \tag{7.14}$$

For a rectangular source, substituting Eq. (7.6) into Eq. (7.13) yields

$$\iint_s y' \frac{e^{-jkR}}{4\pi R} dx'dy' = yFNM_{uniform} + \frac{j}{4\pi k}$$

$$\int_{-a}^{a} \left(e^{-jk\sqrt{(x'-x)^2+(b-y)^2+(z-z')^2}} - e^{-jk\sqrt{(x'-x)^2+(b+y)^2+(z-z')^2}} \right) dx'. \tag{7.15}$$

Linear apodization in the z direction

The potential integral for the apodization function $f(x', y', z') = z'$ applied to a planar source is given by

$$\iint_s z' \frac{e^{-jkR}}{4\pi R} dx'dy' = z'FNM_{uniform}. \tag{7.16}$$

7.1.3 Linear apodization for a subdomain

The apodization function is defined as $f(x', y', z')$ for a subdomain of the volume source in the local coordinate system shown in Figure 7.2. The origin of the local coordinate system is the projection of the observation point onto the base plane of the subdomain. The base plane of the subdomain is either a triangular source which

is formed by three lines $y = 0$, $A_1x + B_1y + C_1 = 0$ and $A_2x + B_2y + C_2 = 0$ or a rectangular source with the width and height $2a$, and $2b$, respectively.

Linear apodization in the x direction

Consider the apodization function $f(x', y', z') = x'$ for a subdomain of the volume source in the local coordinate system shown in Figure 7.2. The potential generated by the subdomain is the linear superposition of the following two integrals,

$$\iiint_V x' \frac{e^{-jkR}}{4\pi R} dV = \iiint_V (x' - x) \frac{e^{-jkR}}{4\pi R} dV + \iiint_V x \frac{e^{-jkR}}{4\pi R} dV. \tag{7.17}$$

The first volume integral on the right side of Eq. (7.17) is computed as

$$\iiint_V (x' - x) \frac{e^{-jkR}}{4\pi R} dV = \int_0^{hv} \int\int_s (x' - x) \frac{e^{-jkR}}{4\pi R} ds dz'. \tag{7.18}$$

For a triangular base plane, substituting Eq.(7.11) into Eq. (7.18), then exchanging the order of integration and analytically evaluating the innermost integral gives

$$\iiint_V (x' - x) \frac{e^{-jkR}}{4\pi R} dV$$

$$= \int_0^{hv} \left(\frac{j}{4\pi k} \frac{z - z'}{z} \int_0^{-C_1/B_1} (e^{-jk\frac{z-z'}{z}R_{b2}} - e^{-jk\frac{z-z'}{z}R_{b1}}) dy') dz'$$

$$= \frac{j}{4\pi k} \int_0^{-C_1/B_1} \frac{e^{-jk(R_1+R_2)}}{k^2 R_1^2 R_2^2} (e^{jk(R_1+R_2)}(R_2^2 - R_1^2)z)$$

$$- \frac{e^{-jk(R_1+R_2)}}{k^2 R_1^2 R_2^2} (e^{jkR_2} R_2^2 z - e^{jkR_1} R_1^2 z + jR_1 R_2 kz(R_2 e^{jkR_2} - R_1 e^{jkR_1})) dy' \tag{7.19}$$

where $R_2 = \sqrt{(L_2(y') - x)^2 + (y' - y)^2 + z^2}$ and
$R_1 = \sqrt{(L_1(y') - x)^2 + (y' - y)^2 + z^2}$.

For a rectangular base plane, substituting Eq.(7.15) into Eq. (7.18), then exchanging the order of integration and analytically evaluating the innermost integral gives

$$\iiint_V (x'-x)\frac{e^{-jkR}}{4\pi R}dV$$

$$= \int_0^{h_v} (\frac{j}{4\pi k}\frac{z-z'}{z}\int_{-b}^{b}(e^{-jk\frac{z-z'}{z}}R_{b2} - e^{-jk\frac{z-z'}{z}}R_{b1})dy')dz'$$

$$= \frac{j}{4\pi k}\int_{-b}^{b}\frac{e^{-jk(R_1+R_2)}}{k^2R_1^2R_2^2}(e^{jk(R_1+R_2)}(R_2^2-R_1^2)z)$$

$$-\frac{e^{-jk(R_1+R_2)}}{k^2R_1^2R_2^2}(e^{jkR_2}R_2^2z - e^{jkR_1}R_1^2z + jR_1R_2kz(R_2e^{jkR_2} - R_1e^{jkR_1}))dy' \tag{7.20}$$

where $R_2 = \sqrt{(a-x)^2+(y'-y)^2+z^2}$ and $R_1 = \sqrt{(a+x)^2+(y'-y)^2+z^2}$.
The second volume integral on the right side of Eq. (7.17) is computed as

$$\iiint_V x\frac{e^{-jkR}}{R}dV = xFNM. \tag{7.21}$$

7.1.4 Linear apodization in the y direction

The apodization function is defined as $f(x',y',z') = y'$ for a subdomain of the volume source in the local coordinate system shown in Figure 7.2. The potential generated by the subdomain is the linear superposition of the following two integrals,

$$\iiint_V y'\frac{e^{-jkR}}{4\pi R}dV = \iiint_V (y'-y)\frac{e^{-jkR}}{4\pi R}dV + \iiint_V y\frac{e^{-jkR}}{4\pi R}dV. \tag{7.22}$$

For a triangular base plane, the first triple integral on the right hand side of Eq. (7.22) is given by,

$$\iiint_V (y'-y)\frac{e^{-jkR}}{4\pi R}dV = \frac{j}{4\pi k}\int_0^{-C_2/A_2} \frac{e^{-jk(R_1+R_2)}}{k^2R_1^2R_2^2}(e^{jk(R_1+R_2)}(R_2^2-R_1^2)z)$$

$$-\frac{e^{-jk(R_1+R_2)}}{k^2R_1^2R_2^2}(e^{jkR_2}R_2^2z - e^{jkR_1}R_1^2z + jR_1R_2kz(R_2e^{jkR_2} - R_1e^{jkR_1}))dx'$$

$$+\frac{j}{4\pi k}\int_{-C_1/A_1}^{0} \frac{e^{-jk(R_1+R_3)}}{k^2R_1^2R_3^2}(e^{jk(R_1+R_3)}(R_3^2 - R_1^2)z)$$

$$-\frac{e^{-jk(R_1+R_3)}}{k^2R_1^2R_3^2}(e^{jkR_2}R_3^2z - e^{jkR_1}R_1^2z + jR_1R_3kz(R_3e^{jkR_3} - R_1e^{jkR_1}))dx' \tag{7.23}$$

where $R_2 = \sqrt{(x'-x)^2 + (L_4(x') - y)^2 + z^2}$, $R_1 = \sqrt{(x'-x)^2 + y^2 + z^2}$ and $R_3 = \sqrt{(x'-x)^2 + (L_3(x') - y)^2 + z^2}$.

For a rectangular base plane, the first triple integral on the right hand side of Eq. (7.22) is given by

$$\iiint_V (y' - y)\frac{e^{-jkR}}{4\pi R}dV = \frac{j}{4\pi k}\int_{-a}^{a} \frac{e^{-jk(R_1+R_2)}}{k^2R_1^2R_2^2}(e^{jk(R_1+R_2)}(R_2^2 - R_1^2)z)$$

$$-\frac{e^{-jk(R_1+R_2)}}{k^2R_1^2R_2^2}(e^{jkR_2}R_2^2z - e^{jkR_1}R_1^2z + jR_1R_2kz(R_2e^{jkR_2} - R_1e^{jkR_1}))dx', \tag{7.24}$$

where $R_2 = \sqrt{(x'-x)^2 + (b-y)^2 + z^2}$ and $R_1 = \sqrt{(x'-x)^2 + (b+y)^2 + z^2}$.

The second triple integral on the right hand side of Eq. (7.22) is equivalent to,

$$\iiint_V y\frac{e^{-jkR}}{R}dV = yFNM. \tag{7.25}$$

7.1.5 Linear apodization in the z direction

The apodization function is defined as $f(x', y', z') = z'$ for a subdomain of the volume source in the local coordinate system shown in Figure 7.2. The potential is given by

$$\iiint_V z' \frac{e^{-jkR}}{4\pi R} dV = \int_0^z z' \iint_s \frac{e^{-jkR}}{4\pi R} ds dz'. \tag{7.26}$$

Substituting the FNM expression for the surface source into Eq. (7.26) and exchanging the order of integration yields

$$\iiint_V z' \frac{e^{-jkR}}{4\pi R} dV$$

$$= \int_0^z z' \frac{j}{4\pi k} \sum_{i=1}^{N} \int_{l_{bi1}}^{l_{bi2}} h_{bi} \frac{e^{-jk\frac{z-z'}{z}\sqrt{Q^2+z^2+h_{bi}^2}} - e^{-jk(z-z')}}{Q^2 + h_{bi}^2} dQ dz'$$

$$= \frac{j}{4\pi k} \sum_{i=1}^{N} \int_{l_{bi1}}^{l_{bi2}} \int_0^z z' h_{bi} \frac{e^{-jk\frac{z-z'}{z}\sqrt{Q^2+z^2+h_{bi}^2}} - e^{-jk(z-z')}}{Q^2 + h_{bi}^2} dz' dQ$$

$$= \frac{j}{4\pi k} \frac{h_{bi}}{Q^2 + h_{bi}^2} \sum_{i=1}^{N} \int_{l_{bi1}}^{l_{bi2}} \left(\frac{z^2(1 - jk\sqrt{Q^2 + z^2 + h_{bi}^2} - e^{-jk\sqrt{Q^2+z^2+h_{bi}^2}})}{k^2(Q^2 + z^2 + h_{bi}^2)} \right.$$

$$\left. - \frac{(1 - jkz - e^{-jkz})}{k^2} \right) dQ. \tag{7.27}$$

Then, the 1D integral for the linear apodization in the z direction is obtained.

7.1.6 The prism geometry

The prism source evaluated here is shown in Figure 7.3, and the coordinates of each vertex of the prism are given in Table 7.1.

Table 7.1. Vertex locations defined for the prism source..

Vertex	A	B	C	D	E	F
(x, y, z) [m]	(0, 1, 0)	(0, 0, 0)	(1, 0, 0)	(0, 1, 1)	(0, 0, 1)	(1, 0, 1)

7.1.7 Global and local systems

The global coordinate system is denoted by (x, y, z), and the rotated coordinate system is denoted by (X, Y, Z). The rotation is characterized by Euler angles using the Z-X-Z convention, where

α is the angle between the x-axis and the intersection of the xy and the XY coordinate planes.

β is the angle between the z-axis and the $Z-$axis.

γ is the angle between the intersection of the xy and the XY coordinate planes and the $X-$axis.

The relationship between the global coordinates (x, y, z) and the rotated coordinates (X, Y, Z) is given by

$$\begin{bmatrix} X \\ Y \\ Z \end{bmatrix} = \begin{bmatrix} \cos\alpha\cos\gamma - \cos\beta\sin\alpha\sin\gamma & \sin\alpha\cos\gamma + \cos\beta\cos\alpha\sin\gamma & \sin\beta\sin\gamma \\ -\cos\alpha\sin\gamma - \cos\beta\sin\alpha\cos\gamma & \cos\beta\cos\alpha\cos\gamma - \sin\alpha\sin\gamma & \sin\beta\cos\gamma \\ \sin\beta\sin\alpha & -\sin\beta\cos\alpha & \cos\beta \end{bmatrix} \begin{bmatrix} x \\ y \\ z \end{bmatrix} \tag{7.28}$$

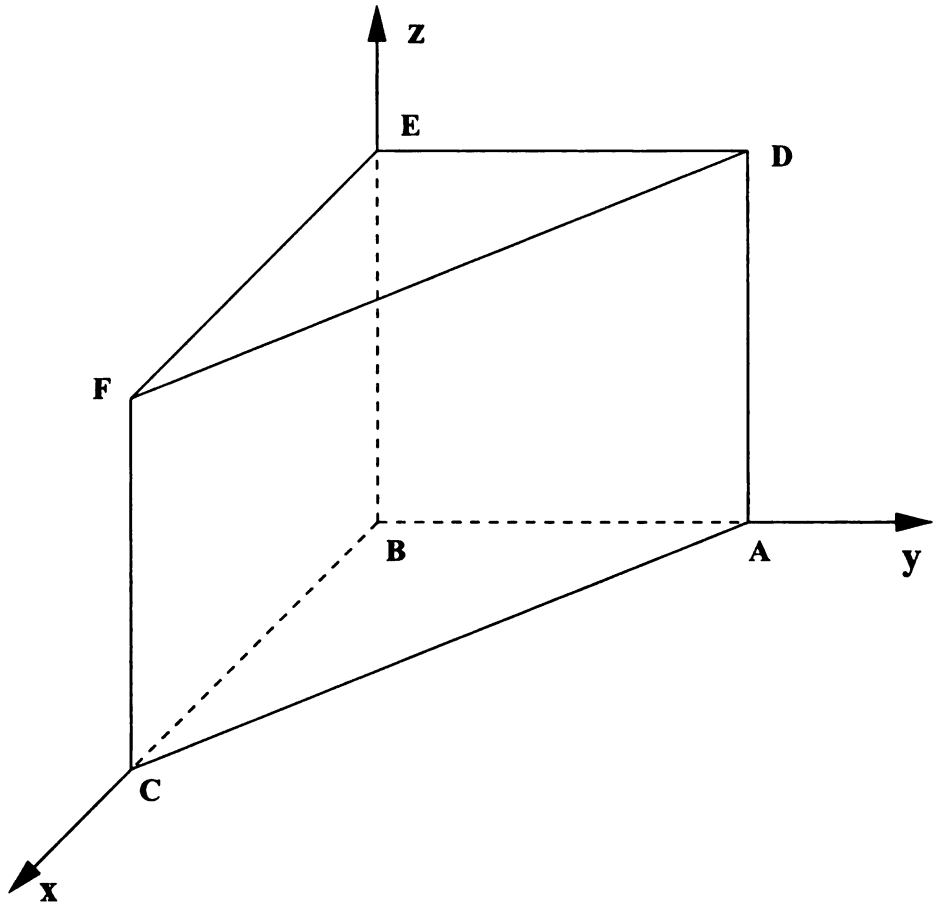

Figure 7.3. The prism geometry, where vertex B is coincident with the origin, and vertices C, A, and E are located on the x, y, and z axes, respectively.

The plane defined by the vertices $ADEB$

The Euler angles for the plane defined by the vertices $ADEB$ are $(\alpha, \beta, \gamma) = (\pi/2, \pi/2, 0)$. After rotating the global coordinate system xyz according to the Euler angles (α, β, γ), the origin of the rotated system $X_1Y_1Z_1$is translated to the center of the rectangle $ADEB$ which is denoted by (x_1, y_1, z_1). The values of (x_1, y_1, z_1) are given by $(\frac{1}{2}, \frac{1}{2}, 0)$. Substituting the Euler angles into Eq. (7.28) yields

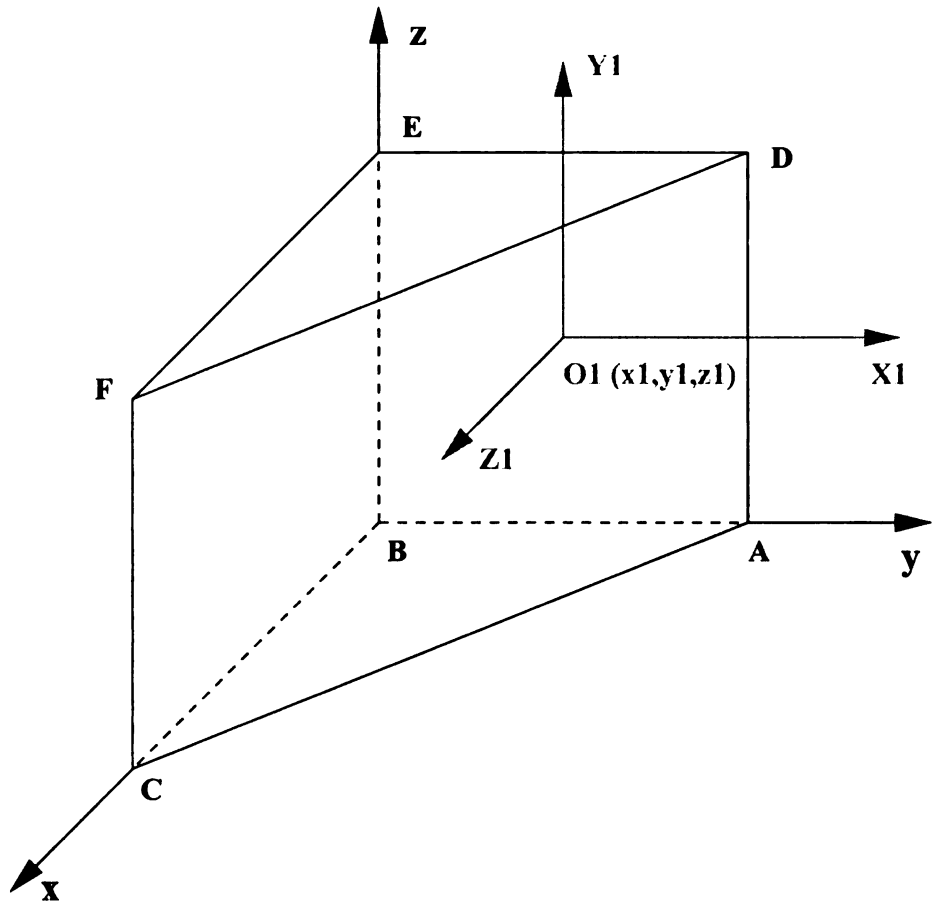

Figure 7.4. The local coordinate system for the plane $ADEB$.

$$\begin{bmatrix} X_1 \\ Y_1 \\ Z_1 \end{bmatrix} = \begin{bmatrix} 0 & 1 & 0 \\ 0 & 0 & 1 \\ 1 & 0 & 0 \end{bmatrix} \begin{bmatrix} x \\ y \\ z \end{bmatrix} - \begin{bmatrix} x_1 \\ y_1 \\ z_1 \end{bmatrix} = \begin{bmatrix} y - \frac{1}{2} \\ z - \frac{1}{2} \\ x \end{bmatrix}. \tag{7.29}$$

Rewriting Eq. (7.29) yields

$$\begin{bmatrix} x \\ y \\ z \end{bmatrix} = \begin{bmatrix} Z_1 \\ X_1 + \frac{1}{2} \\ Y_1 + \frac{1}{2} \end{bmatrix}. \tag{7.30}$$

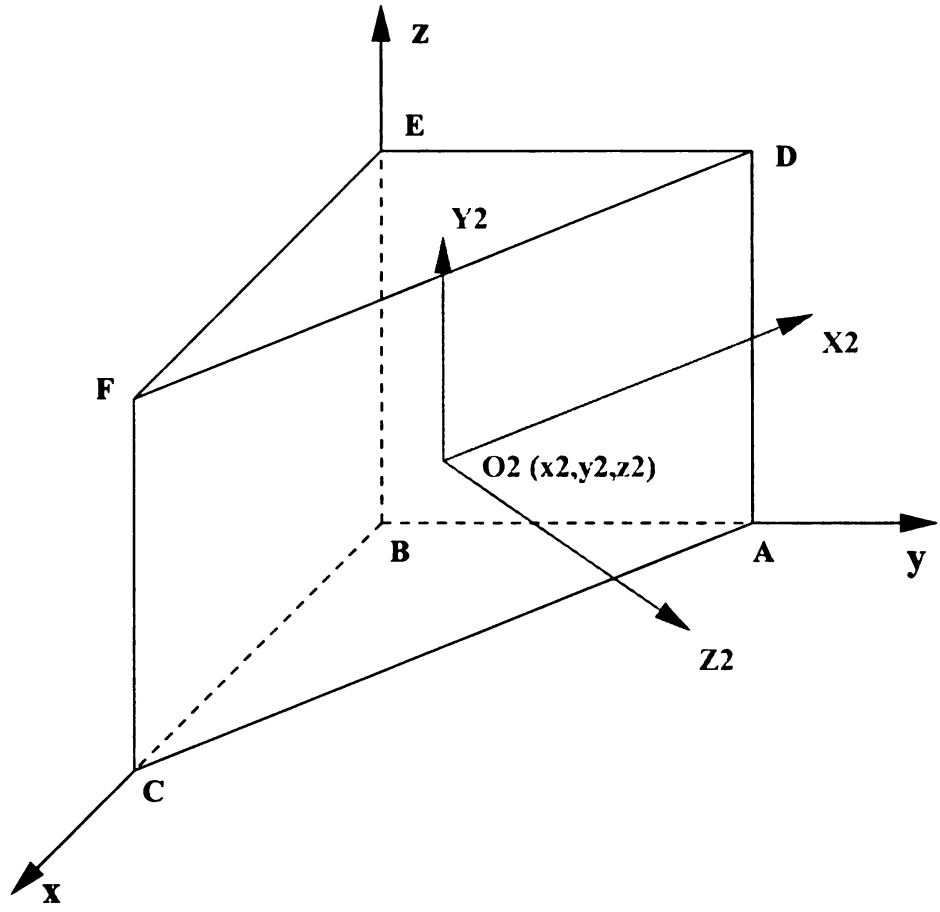

Figure 7.5. The local coordinate system for the plane *ADFC*.

The plane defined by the vertices *ADFC*

The Euler angles for the plane defined by the vertices *ADFC* is $(\alpha, \beta, \gamma) = (3\pi/4, \pi/2, 0)$. After rotating the global coordinate system xyz according to the Euler angles (α, β, γ), the origin of the rotated system $X_2Y_2Z_2$ is translated to the center of the rectangle *ADFC* which is denoted by (x_2, y_2, z_2). The values of (x_2, y_2, z_2) are given by $(0, \frac{1}{2}, \frac{\sqrt{2}}{2})$. Substituting the Euler angles into Eq. (7.28) yields

$$\begin{bmatrix} X_2 \\ Y_2 \\ Z_2 \end{bmatrix} = \begin{bmatrix} -\sqrt{2}/2 & \sqrt{2}/2 & 0 \\ 0 & 0 & 1 \\ \sqrt{2}/2 & \sqrt{2}/2 & 0 \end{bmatrix} \begin{bmatrix} x \\ y \\ z \end{bmatrix} - \begin{bmatrix} x_2 \\ y_2 \\ z_2 \end{bmatrix} = \begin{bmatrix} -\frac{\sqrt{2}}{2}x + \frac{\sqrt{2}}{2}y \\ z - \frac{1}{2} \\ \frac{\sqrt{2}}{2}x + \frac{\sqrt{2}}{2}y - \frac{\sqrt{2}}{2} \end{bmatrix}. \tag{7.31}$$

Rewrite Eq. (7.31) yields

$$\begin{bmatrix} x \\ y \\ z \end{bmatrix} = \begin{bmatrix} \frac{\sqrt{2}}{2}Z_2 - \frac{\sqrt{2}}{2}X_2 + \frac{1}{2} \\ \frac{\sqrt{2}}{2}X_2 + \frac{\sqrt{2}}{2}Z_2 + \frac{1}{2} \\ Y_2 + \frac{1}{2} \end{bmatrix}. \tag{7.32}$$

The plane defined by the vertices $BEFC$

The Euler angles for the plane defined by the vertices $BEFC$ is $(\alpha, \beta, \gamma) = (\pi, \pi/2, 0)$. After rotating the global coordinate system xyz according to the Euler angles (α, β, γ), the origin of the rotated system $X_3Y_3Z_3$ is translated to the center of the rectangle $BEFC$ which is denoted by (x_3, y_3, z_3). The values of (x_3, y_3, z_3) are given by $(-\frac{1}{2}, \frac{1}{2}, 0)$. Substituting the Euler angles into Eq. (7.28) yields

$$\begin{bmatrix} X_3 \\ Y_3 \\ Z_3 \end{bmatrix} = \begin{bmatrix} -1 & 0 & 0 \\ 0 & 0 & 1 \\ 0 & 1 & 0 \end{bmatrix} \begin{bmatrix} x \\ y \\ z \end{bmatrix} - \begin{bmatrix} x_3 \\ y_3 \\ z_3 \end{bmatrix} = \begin{bmatrix} -x + \frac{1}{2} \\ z - \frac{1}{2} \\ y \end{bmatrix}. \tag{7.33}$$

Rewriting Eq. (7.33) yields

$$\begin{bmatrix} x \\ y \\ z \end{bmatrix} = \begin{bmatrix} -X_3 + \frac{1}{2} \\ Y_3 + \frac{1}{2} \\ Z_3 \end{bmatrix}. \tag{7.34}$$

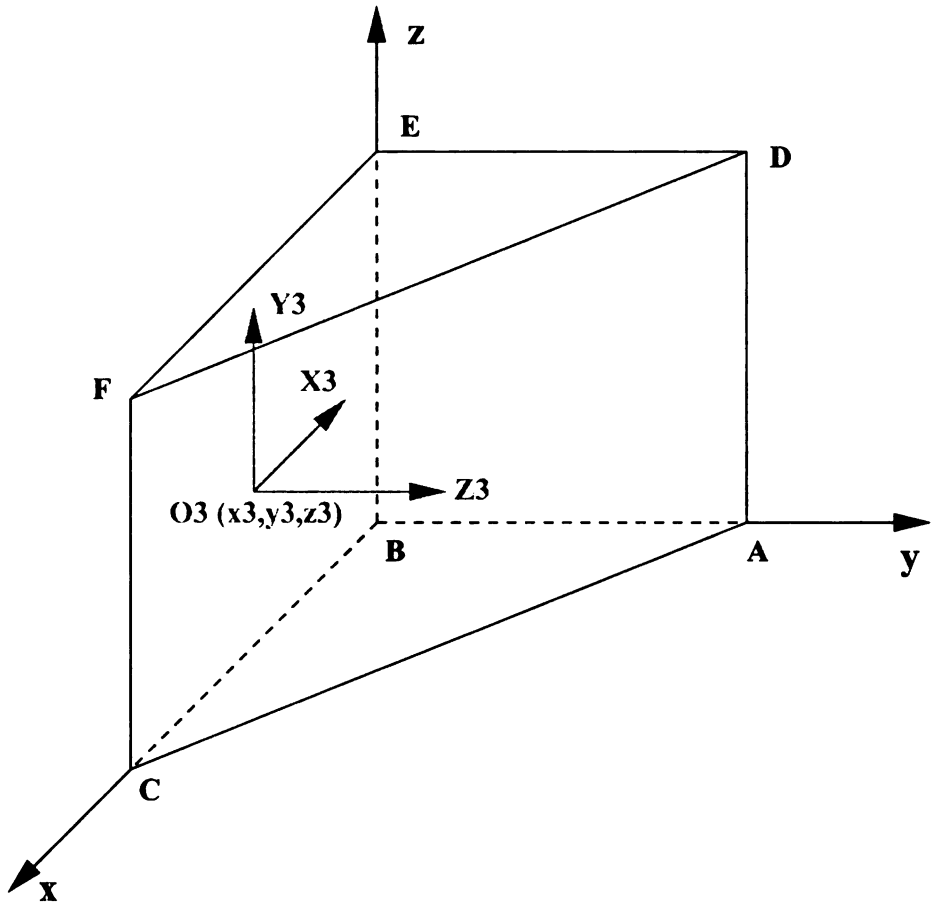

Figure 7.6. The local coordinate system for the plane $BEFC$.

7.1.8 Evaluating potential integrals generated by each subdomain

To calculate the potential integrals generated by the volume source shown in Figure 7.3, the volume is subdivided into five subdomains. The potential generated by the prism , denoted by Φ_a, is obtained by superposing the contributions generated by each subdomain according to

$$\Phi_a = \iiint_V f(x',y',z')\frac{e^{-jkR}}{4\pi R}dx'dy'dz' = \sum_{m=1}^{M}\frac{(A_m x + B_m y + C_m z + D_m)}{|A_m x + B_m y + C_m z + D_m|}\Phi_{am} \tag{7.35}$$

where $M = 5$ is the number of faces that the volume has, $A_m x + B_m y + C_m z + D_m = 0$ denotes the general form of the plane that passes through each face of the prism, and Φ_{am} is the potential on each subdomain. The expressions of Φ_{am} is

$$\Phi_{am} = \iiint_v f(X',Y',Z')\frac{e^{-jkR}}{4\pi R}dX'dY'dZ', \tag{7.36}$$

for each subvolume, where $f(X',Y',Z')$ is the apodization function in the local coordinate system, which can be obtained by substituting the expressions for the x', y', z' terms defined by Eqs. (7.30), (7.32), and (7.34).

7.1.9 Error calculations

For potential calculations, the numerical error $\eta(x,\ y,\ z;\ k)$ is defined as the normalized difference between the reference potential $\Phi_{ref}(x,y,z)$ and the computed potential $\Phi(x,y,z)$ according to

$$\eta(x,y,z;\ k) = \frac{|\Phi(x,y,z) - \Phi_{ref}(x,y,z)|}{max|\Phi_{ref}(x,y,z;\ k)|}, \tag{7.37}$$

The maximum error η_{max} is defined as

$$\eta_{max} = \max_{x,y,z}\eta(x,\ y,\ z), \tag{7.38}$$

and the number of significant digits n is given by

$$n = log10(\eta_{max}) \tag{7.39}$$

Table 7.2. Simulation parameters that achieve between 2 and 5 significant digits using the FNM and the singularity cancellation method to evaluate a potential integral with linear apodization evaluated on a 3D grid. Parameters listed include the number of significant digits achieved and the ratio of the computation time relative to the time required for the FNM. (a) Significant digits 2 and 3. (b) Significant digits 4 and 5.

(a)

Significant digits	2		3	
	FNM	Singularity cancellation	FNM	Singularity cancellation
Time (seconds)	0.095	0.83	0.11	1.70
Computaton time relative to FNM	1×	8.74×	1×	15.45×

(b)

Significant digits	4		5	
	FNM	Singularity cancellation	FNM	Singularity cancellation
Time (seconds)	0.16	4.96	0.25	8.69
Computation time relative to FNM	1×	31.00×	1×	34.76×

7.2 Results

The potential integral with linear apodization is evaluated on a 3D grid. The x and y directions extend from -0.5m to 1.5m with an interval of 0.02m, the z direction extends from 0 to 1.5m with an interval of 0.03m. The reference potential is computed using the singularity cancellation method evaluated with 1000 Gauss abscissas in each direction. Figure 7.7 contains a plot of the number of significant digits achieved with the FNM and the singularity cancellation method evaluated on a 3D grid as a function of computation times. Table 7.2 summarizes the ratio of the computation times obtained with the FNM and the singularity cancellation method when each achieves between 2 and 5 significant digits on a 3D computational grid. For this computational grid, the FNM is 8.74, 15.45, 31.00, 34.76 times faster than the singularity cancellation method when each achieves 2, 3, 4, and 5 significant digits, respectively.

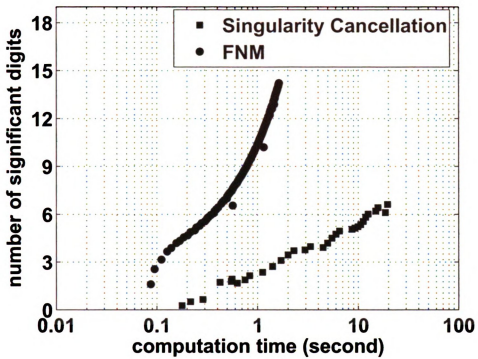

Figure 7.7. The number of significant digits achieved in calculations od the potential integrals linear apodization over the prism plotted as a function of computation time for evaluations on a 3D grid. The results show that the FNM achieves a larger number of significant digits than the singularity cancellation method for the same computation time.

7.3 Discussion

7.3.1 Other volume sources

The potential integral with linear apodization in Eq. (7.1) is a triple integral and the 1D FNM integral reduces this triple integral to the evaluation of a small number of single integrals. The 1D FNM integral converges much faster than the singularity cancellation method, and the 1D FNM integral needs much less computation time to achieve a given accuracy than the singularity cancellation method. The fast nearfield method calculations developed here are easily extended to any volume source with

polygonal faces. First, the volume source is subdivided into subdomains, and the number of subdomains is equal to the number of polygonal faces. Then, the potential generated in each subdomain is computed in the local coordinate system, where the Euler angle is first obtained for each of the base planes. The total potential generated by the volume source is obtained by superposing the potentials produced by each of the subdomains.

7.3.2 Higher order polynomials

The 1D FNM expressions for volume potentials with linear apodization are derived here. The FNM expressions of the volume potential integrals with higher order polynomial apodization can be derived using the same strategy. The Euler angle is first obtained for each of the base planes, and the apodization function in the global coordinate system is translated into the the function in the local coordinate system. Then, after obtaining the fast nearfield method for each apodization in the local coordinate system and superposing the contributions from each apodization function in local coorinate system yields the total potential.

7.4 Conclusion

1D FNM expressions for calculating volume potentials with linear apodization are derived and evaluated. The 1D FNM integral for a potential integral is first given, and FNM expressions for a planar source with linear apodization is then derived. The volume source is then subdivided into several subdomains including subpyramids and subtetrahedrons. The potential generated by each subdomain is computed in the local coordinate system and the total potential over the volume source is the superposition of the potential generated by each subdomain. After the 1D FNM expressions are obtained, the results obtained with the FNM are compared with the

singularity cancellation method on a large 3D observation grid. The results indicate that, for the 3D grid used here, the FNM reduces the computation time by a factor of 8.74 to 34.76 relative to the singularity cancellation method when each achieves between 2 and 5 significant digits on a 3D grid. Thus, the FNM is an ideal method for linear apodized potentials.

CHAPTER 8

Conclusion

This thesis derives and evaluates fast expressions for calculating pressures generated by planar pistons and potentials generated by volume sources. The 1D fast nearfield method (FNM) expressions are compared to several existing methods including the implulse response method, the Rayleigh-Sommerfield integral, the Field II program and the singularity cancellation method. Chapter 2 introduces 1D fast nearfield method expressions for the time-harmonic and transient pressures generated by triangular pistons. These fast nearfield method expressions remove singularities from a 1D integral and therefore converge very quickly. The transient calculations are further accelerated by time-space decomposition. The fast nearfield expressions for a triangular source are compared with the impulse response method, the Field II program, and the smoothed impulse response. The comparison results indicate that the fast nearfield method achieves smaller errors than the other three methods in less time.

Analytical 2D integral expressions for fast calculations of time-harmonic and transient nearfield pressures generated by apodized rectangular pistons are given in Chapter 3. A simplified time space decomposition method is also introduced to further reduce the computation time for transient pressure fields. The results are compared

with the Rayleigh-Sommerfeld integral and the Field II program to show that the 2D FNM integral converges much faster than the Rayleigh-Sommerfeld integral and the Field II program.

As a special case of Chapter 3, A fast nearfield method for calculating pressure generated by a polynomial apodized rectangular pistion is obtained based on the instantaneous impulse response in Chapter 4. Two kinds of apodization functions are considered in the derivation process. A trigonometric transform of the integrand is performed and the order of integration is exchanged to obtain the 1D fast nearfield method expressions. The results show that the 1D polynomial apodized FNM converge faster than the Rayleigh-Sommerfeld integral and the 2D apodized FNM.

Chaper 5 introduces a 1D fast nearfield method for the calculations of uniformly excited volume potential integrals. The results are compared with the singularity cancellation method at six different observation points and a volume grid, and the results show that the fast nearfield method needs less sample points than the singularity cancellation method to achieve a given number of significant digits. A 1D fast nearfield method to calculate potentals generated by surface integrals and volume integrals with polynomial apodization are introduced in Chapters 6 and 7. These expressions remove the singularities from the Rayleigh-Sommerfeld method integral. The results compared with the singularity cancellation method indicate that the 1D fast nearfield method achieves much faster convergence with much less computation time.

BIBLIOGRAPHY

[1] F. Oberhettinger, "On transient solutions of the 'baffled piston' problem," Journal of Research of the National Bureau of Standards-B. Mathematics and Mathematical Physics, 65B(1):1-6, 1961.

[2] P. R. Stepanishen, "Transient radiation from pistons in an infinite planar baffle," J. Acoust. Soc. Am., 49(5):1629-1638, 1971.

[3] J. C. Lockwood and J. G.Willette, "High-speed method for computing the exact solution for the pressure variations in the nearfield of a baffled piston," J. Acoust. Soc. Am., 53(3):735-741, 1973.

[4] J. A. Jensen, "Ultrasound fields from triangular apertures," J. Acoust. Soc. Am., 100(4), pp. 2049-2056, 1996.

[5] J. Zemanek, "Beam behavior within the nearfield of a vibrating piston," J. Acoust. Soc. Am., 49(1):181-191, 1971.

[6] K. B. Ocheltree and L. A. Frizzell, "Sound field calculation for rectangular sources," IEEE Trans. Ultrason. Ferroelect. Freq. Contr., 36(2):242-248, 1989.

[7] R. J. McGough, T. V. Samulski, and J. F. Kelly, "An efficient grid sectoring method for calculations of the nearfield pressure generated by a circular piston," J. Acoust. Soc. Am. Vol 115 (5), Pt. 1, May 2004, pp. 1942-1954.

[8] R. J. McGough, "Rapid calculations of time-harmonic nearfield pressures produced by rectangular pistons," J. Acoust. Soc. Am., 115(5), Pt. 1, 2004.

[9] J. A. Jensen, "A new calculation procedure for spatial impulse responses in ultrasound," J. Acoust. Soc. Am. 105(6), 3266-3274 (1999).

[10] J. A. Jensen, "Field: A program for simulating ultrasound systems, " Med. Biol. Eng. Comp., 10th Nordic-Baltic Conference on Biomedical Imaging, Vol. 4, Supplement 1, Part 1:351-353, 1996b.

[11] J. A. Jensen and N. B. Svendsen, "Calculation of pressure fields from arbitrarily shaped, apodized, and excited ultrasound transducers," IEEE Trans. Ultrason., Ferroelec., Freq. Contr., 39:262-267, 1992.

[12] D. Chen, J. F. Kelly, and R. J. McGough, "A fast nearfield method for calculations of time-harmonic and transient pressures produced by triangular pistons," J. Acoust. Soc. Am. 120 (5), 2450-2459 (2006).

[13] X. Zeng and R. J. McGough, "Evaluation of the angular spectrum approach for simulations of nearfield pressures," J. Acoust. Soc. Am. 123(1), 68-76 (2008).

[14] T. D. Mast, "Fresnel approximations for acoustic fields of rectangularly symmetric sources," J. Acoust. Soc. Am. 121 (6), 3311-3322 (2007).

[15] G. R. Harris, "Review of transient field theory for a baffled planar piston," J. Acoust. Soc. Am. 70(1), 10-20 (1981).

[16] M. Greenspan, "Piston radiator: Some extensions of the theory," J. Acoust. Soc. Am. 65(3), 608-621 (1979).

[17] C. Lafon, F. Prat, J. Y. Chapelon, F. Gorry, J. Margonari, Y. Theillere, and D. Cathignol, "Cylindrical thermal coagulation necrosis using an interstitial applicator with a plane ultrasonic transducer: *in vitro* and *in vivo* experiments versus computer simulations," Int. J. Hyperthermia 16, 508-522 (2000).

[18] D. R. Daum, and K. Hynynen, "A 256-element ultrasonic phased array system for the treatment of large volumes of deep seated tissues," IEEE Trans. Ultrason., Ferroelect. Freq. Contr. 46(5), 1254-1268 (1999).

[19] Y. Li and J. A. Zagzebski, "A frequency domain model for generating B-mode images with array transducers," IEEE Trans. Ultrason., Ferroelect. Freq. Contr., 46(3), 690-699 (1999).

[20] G. Cincotti, G. Cardone, P. Gori, and M. Pappalardo, "Efficient transmit beamforming in Pulse-Echo ultrasonic imaging," IEEE Trans. Ultrason., Ferroelect. Freq. Contr. 46(6), 1450-1458 (1999).

[21] Y. Lin, J. M. Dodson, J. D. Hamilton, J-U. A. Kluiwstra, C. Cain, and K. Grosh, "Theory and experiment for the design of piezoeletric element for phased arrays," Proceedings of Ultrasonics Symposium, 2, 1697-1700 (1997).

[22] J. L. Prego Borges, F. Montero de Espinosa, J. Salazar, J. Garcia-Alvarez, J. A. Chavez, A. Turo, and M. J. Garcia-Hernandez, "Diffraction aperture non-ideal behaviour of air coupled transducers array elements designed for NDT," Ultrasonics, 44, Supplement 1, e667-e672 (2006).

[23] B. M. Notaros and B. D. Popovic, "Optimized entire-domain momentmethod analysis of 3D dielectric scatterers," Int. J. Numer. Model., vol. 10, pp. 177–192, 1997.

[24] S. M. Rao, D. R. Wilton, and A. W. Glisson, "Electromagnetic scattering by surfaces of arbitrary shape," IEEE Trans. Antennas Propagat., vol. AP-30, pp. 409-418, May 1982.

[25] C. M. Butler, "Evaluation of potential integral at singularity of exact kernel in thin-wire calculations," IEEE Trans. Antennas Propag., vol. AP-23, pp. 293–295, Mar. 1975.

[26] D. H. Werner, J. A. Huffman, and P. L. Werner, "Techniques for evaluating the uniform current vector potential at the isolated singularity of the cylindrical wire kernel," IEEE Trans. Antennas Propag., vol. 42, pp. 1549–1553, Nov. 1994.

[27] L. Rossi and P. J. Cullen, "On the fully numerical evaluation of the linear-shape function times the 3-D Green's function on a plane triangle," IEEE Trans. Microwave Theory Tech., vol. 47, pp. 398–402, Apr. 1999.

[28] T. F. Eibert and V. Hansen, "On the calculation of potential integrals for linear source distributions on triangular domains," IEEE Trans. Antennas Propag., vol. 43, pp. 1499–1502, Dec. 1995.

[29] M. A. Khayat and D. R. Wilton, "Numerical Evaluation of singular and near-singular potential integrals", IEEE Trans. Antennas Propag., vol. 53, no. 10, 2005.

[30] M. G. Duffy, "Quadrature over a pyramid or cube of integrands with a singularity at a vertex," SIAM J. Numer. Anal., vol. 19, no. 6, pp. 1260–1262, 1982.

[31] M. A. Khayat and D. R. Wilton, "Numerical Evaluation of singular and near-singular potential integrals", *IEEE Transactions on antennas and propagations*, vol. 53, no. 10, 2005.

[32] A. H. Stroud, Approximate Calculation of Multiple Integrals. Englewood Cliffs, NJ: Prentice-Hall, 1971, pp. 31–32.

[33] R. D. Graglia, "Static and dynamic potential integrals for linearly varying source distributions in two- and three-dimensional problems," IEEE Trans. Antennas Propag., vol. AP-35, pp. 662–669, Jun. 1987.

[34] M. Frigo and S. G. Johnson, "FFTW: An adaptive software architecture for the FFT," Proceedings of the ICASSP, vol 3, no. 1, pp.1381-1384, 1998.

[35] J. D'hooge, J. Nuyts, B. Bijnens, B. De Man, P. Suetens, J. Thoen, M.-C. Herregods, and F. Van de Werf, "The calculation of the transient near and far field of a baffled piston using lwo sampling frequencies," J. Acoust. Soc. Am. 102(1), 78-86 (1997).

[36] J. F. Kelly and R. J. McGough, "A time-space decomposition method for calculating the near field pressure generated by a pulsed circular piston," IEEE Trans. Ultrason. Ferroelect. Freq. Contr., 53(6), pp. 1150-1159, 2006.

[37] J. F. Kelly and R. J. McGough, "An annular superposition integral for axisymmetric radiators," J. Acoust. Soc. Am. 121(2), 759-765 (2007).

[38] T. L. Szabo, "Generalized fourier transform diffraction theory for parabolically anisotropic media", *J. Acoust. Soc. Am.*, vol. 63(1), pp. 28-34, 1978.

[39] X. Zeng, Private communication, 2008.

[40] J. J. Wen and M. A. Breazeale, "A diffraction beam field expressed as the superposition of Gaussian beams," J. Acoust. Soc. Am. 83(5), 1752-1756 (1988).

[41] D. Ding, Y. Zhang, and J. Liu, "Some extensions of the Gauss beam expansion: Radiation fields of the rectangular and the elliptical transducer," J. Acoust. Soc. Am. 113(6), 3043-3048 (2003).

[42] B. D. Cook and W. J. Arnoult III, "Gaussian-Laguerre/Hermite formula for the nearfield of an ultrasonic transducer, " J. Acoust. Soc. Am. 59(1), 9-11 (1976).

[43] D. Chen and R. J. McGough, "A 2D fast nearfield method for calculating nearfield pressures generated by apodized rectangular pistons", accepted by J. Acoust. Soc. Am., 124(3), pp. 1526–1537,2008.

[44] G. Scarano, N. Denisenko, M. Matteucci, and M. Pappalardo, "A new approach to the derivation of the impulse response of a rectangular piston", J. Acoust. Soc. Am. 78 (3), 1985, pp. 1109-1113.

[45] Xiao-Chun Nie, Le-Wei Li, Ning Yuan, Tat Soon Yeo, and Yeow-Beng Gan, "Procorrected-FFT solution of the volume integral equation for 3-D inhomegeneous dielectric objects," IEEE Trans. Antennas Propagat., vol. 53, pp. 313-320, January 2005.

[46] D. Chen and R. J. McGough, "A Fast Nearfield Method for Calculating Pressures Generated by Rectangular Pistons with Polynomial Apodization", IEEE Ultrasonics Symposium, pp. 134-137, 2007.